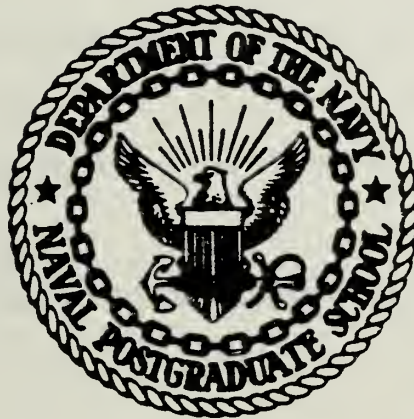


DUDLEY KNOX LIBRARY
NAVAL POST GRADUATE SCHOOL
MONTEREY, CALIF. 93940

NPG-162

NAVAL POSTGRADUATE SCHOOL

Monterey, California



THESIS

AN INVESTIGATION OF UNIPOLAR ARCING IN VARIOUS
CONDUCTORS AND METALLIC GLASSES

by

Todd Jeffrey Hoover

September 1981

Thesis Advisor:

F. Schwirzke

Approved for public release; distribution unlimited

T202293

UNCLASSIFIED

SECURITY CLASSIFICATION OF THIS PAGE (When Data Entered)

REPORT DOCUMENTATION PAGE		READ INSTRUCTIONS BEFORE COMPLETING FORM
1. REPORT NUMBER	2. GOVT ACCESSION NO.	3. RECIPIENT'S CATALOG NUMBER
4. TITLE (and Subtitle) An Investigation of Unipolar Arcing in Various Conductors and Metallic Glasses		5. TYPE OF REPORT & PERIOD COVERED Master's Thesis; September 1981
		6. PERFORMING ORG. REPORT NUMBER
7. AUTHOR(s) Todd Jeffrey Hoover		8. CONTRACT OR GRANT NUMBER(s)
9. PERFORMING ORGANIZATION NAME AND ADDRESS Naval Postgraduate School Monterey, California 93940		10. PROGRAM ELEMENT, PROJECT, TASK AREA & WORK UNIT NUMBERS
11. CONTROLLING OFFICE NAME AND ADDRESS Naval Postgraduate School Monterey, California 93940		12. REPORT DATE September 1981
		13. NUMBER OF PAGES 118
14. MONITORING AGENCY NAME & ADDRESS (if different from Controlling Office) Naval Postgraduate School Monterey, California 93940		15. SECURITY CLASS. (of this report) Unclassified
		15a. DECLASSIFICATION/DOWNGRADING SCHEDULE
16. DISTRIBUTION STATEMENT (of this Report) Approved for public release; distribution unlimited		
17. DISTRIBUTION STATEMENT (of the abstract entered in Block 20, if different from Report)		
18. SUPPLEMENTARY NOTES		
19. KEY WORDS (Continue on reverse side if necessary and identify by block number) Unipolar Arcing Metallic Glass		
20. ABSTRACT (Continue on reverse side if necessary and identify by block number) An investigation of unipolar arcing in various conductors and surface preparations was undertaken. A discussion on the production of "glassy" surfaces on various metals, and their susceptibility to unipolar arcing is also presented. All experiments were conducted using a neodymium glass laser in a Q-switched mode to generate a hot plasma. Results show that stainless steel and mild commercial steel arc very heavily, in agreement with past researchers, while titanium undergoes arcing at a lesser crater density but over a greater surface area,		

20. HY 130 undergoes arcing at a low crater density, and a commercially prepared metallic glass $\text{Fe}_{80}\text{B}_{20}$ and Poco graphite not at all.

Experiments were conducted in attempt to produce metallic glass coatings on stainless steel, HY 130, and a mild commercial steel (1030). Coatings produced were exposed to a laser produced plasma and arcing was found to be present in all cases but at a lower arc density. In conjunction with attempts to produce metallic glass surface coatings on metals, an experiment was done to determine the energy density required for the onset of plasma production in type 304 stainless steel.

Approved for public release; distribution unlimited

An Investigation of Unipolar Arcing in Various
Conductors and Metallic Glasses

by

Todd Jeffrey Hoover
Lieutenant, United States Navy
B.S., Ohio State University, 1974

Submitted in partial fulfillment of the
requirements for the degree of

MASTER OF SCIENCE IN PHYSICS

from the

NAVAL POSTGRADUATE SCHOOL
September 1981

ABSTRACT

An investigation of unipolar arcing in various conductors and surface preparations was undertaken. A discussion on the production of "glassy" surfaces on various metals, and their susceptibility to unipolar arcing is also presented.

All experiments were conducted using a neodymium glass laser in a Q-switched mode to generate a hot plasma. Results show that stainless steel and mild commercial steel arc very heavily, in agreement with past researchers, while titanium undergoes arcing at a lesser crater density but over a greater surface area, HY 130 undergoes arcing at a low crater density, and a commercially prepared metallic glass $\text{Fe}_{30}\text{B}_{20}$ and Poco graphite not at all.

Experiments were conducted in attempt to produce metallic glass coatings on stainless steel, HY 130, and mild commercial steel (1030). Coatings produced were exposed to a laser produced plasma and arcing was found to be present in all cases but at a lower arc density. In conjunction with attempts to produce metallic glass surface coatings on metals, an experiment was done to determine the energy density required for the onset of plasma production in type 304 stainless steel.

TABLE OF CONTENTS

I.	INTRODUCTION	16
II.	BACKGROUND	18
	A. UNIPOLAR ARC PROBLEM	18
	B. UNIPOLAR ARC MODEL	19
	C. METALLIC GLASSES	21
	D. LASER MATERIAL PROCESSING	23
	1. Laser-Target Interaction	23
	2. Laser Processing Results	26
III.	EXPERIMENTAL DESIGN	29
	A. EQUIPMENT	29
	1. Laser	29
	2. Target Test Chamber	31
	3. Optical Microscope	31
	4. Scanning Electron Microscope	31
	B. PROCEDURES	31
	1. Target Preparation	32
	2. Plasma-Surface Interaction	32
	3. Surface Damage Investigation	33
IV.	EXPERIMENTAL RESULTS	34
	A. CONDUCTORS	34
	1. Titanium	34
	2. Poco Graphite	36
	3. Type 304 Stainless Steel	49

4. HY 130	58
5. Copper (Sandblasted)	63
6. Type 316 Stainless Steel	66
7. 1030 Steel	70
B. METALLIC GLASSES	70
1. Metallic Glass $\text{Fe}_{30}\text{B}_{20}$	74
2. Type 304 Stainless Steel	78
3. Type 316 Stainless Steel	95
4. HY 130	96
5. 1030 Steel	99
V. CONCLUSIONS	107
VI. RECOMMENDATIONS	112
APPENDIX A: Composition of HY 130 cast steel	114
APPENDIX B: Laser shot sequences and locations	115
LIST OF REFERENCES	116
INITIAL DISTRIBUTION LIST	118

LIST OF FIGURES

1. Unipolar Arc Model	22
2. Laser and Test Chamber Arrangement	30
3. Titanium. Typical main laser impact crater and molten surface effects (100X optical)	35
4. Titanium. Concentric rings of molten material apparently produced by diffraction of laser pulse (200X optical)	35
5. Titanium. Unipolar arcing at the edge of the molten surface effects with 570 arcs/cm^2 (650X SEM)	37
6. Titanium. Unipolar arcs found at a distance of 3.5mm from the cessation of molten surface effects (500X optical).....	37
7. Titanium. Molten surface effects produced by irradiation at atmospheric pressure (240X SEM).....	38
8. Titanium. Area at the edge of molten surface effects (2400X SEM)	38
9. Poco graphite. Unpolished surface (280X SEM)	40
10. Poco graphite. Unpolished surface (1400X SEM)	40
11. Poco graphite. Surface produced by polishing with a 0.05μ slurry of Al_2O_3 (260X SEM)	41
12. Poco graphite. Polished surface (650X SEM)	41
13. Poco graphite. Main laser impact crater produced by successive pulses of energies of 14 and 15 Joules (50X SEM)	42
14. Poco graphite. View of main laser impact crater center (500X SEM)	42

15.	Poco graphite. View of the crack radiating from main laser impact crater (1000X SEM)	43
16.	Poco graphite. Polished surface after exposure to plasma. Main laser impact crater edge is visible in upper right hand corner (260X SEM)	43
17.	Poco graphite. Close up view of surface shown in previous figure (650X SEM)	44
18.	Poco graphite. Main laser impact crater and diffraction rings produced by 11.9 Joule pulse (32X optical)	44
19.	Poco graphite. Close up view of diffraction rings. Bright spots correspond to still polished areas (125X optical)	46
20.	Poco graphite. Unpolished surface after focused laser irradiation at 13.75 Joules (260X SEM)	46
21.	Poco graphite. Unpolished surface area abutting laser impact area (260X SEM)	47
22.	Poco graphite. Unpolished surface shown in previous figure at higher magnification (650X SEM)	47
23.	Poco graphite. Unpolished surface, as in previous figure, at higher magnification (2600X SEM)	48
24.	Poco graphite. Unpolished surface near main laser impact crater (1300X SEM)	48
25.	304 Stainless. Main laser impact craters (130X SEM)	50
26.	304 Stainless. Unipolar arcing at 2.7mm from main laser impact crater (2500X SEM)	50
27.	304 Stainless. Typical molten surface effects and diffraction pattern (130X SEM)	51

28.	Sandblasted 304. Typical surface structure produced by sand-blasting (220X SEM)	52
29.	Sandblasted 304. View (center) of molten surface effects after irradiation (110X SEM)	52
30.	Sandblasted 304. Close up view of molten surface effects (520X SEM)	54
31.	Sandblasted 304. Molten surface effects seen at 1.0mm from main crater center (1050X SEM)	54
32.	Sandblasted 304. Area of previous figure seen at higher magnification (2100X SEM)	55
33.	Sandblasted 304. Area seen near cessation of molten surface effects. Note unipolar arc in upper right hand corner (2200X SEM)	55
34.	Sandblasted 304. X-ray spectrum produced by area in previous figure. Lines (left to right) are: aluminum, silicon, manganese, chromium, iron, iron, and nickel	56
35.	Sandblasted 304. Surface seen at cessation of surface effects (2200X SEM)	57
36.	Sandblasted 304. Scintillations from x-rays from silicon. Each spot of light corresponds to x-ray radiation received from area in previous figure	57
37.	HY 130. Main laser impact crater resulting from a 12.14 Joule focused pulse (160X optical)	59
38.	HY 130. Unipolar arcing where left side of figure is 0.5mm from main laser impact crater (160X optical)	59

39.	HY 130. Top of figure is 0.75mm from main laser crater. Note extremely large arc craters (160X optical)	61
40.	HY 130. Largest unipolar arc (found at top) measures 0.140mm diameter with a cathode spot of 0.023mm (200X optical) ..	61
41.	HY 130. Polished surface showing porosity of the cast material (100X optical)	62
42.	Sandblasted copper. View of main laser impact crater (580X SEM)	64
43.	Sandblasted copper. Increased magnification view of main crater (1200X SEM)	64
44.	Sandblasted copper. Unipolar arc seen at right, found in main laser crater (2300X SEM)	65
45.	Sandblasted copper. View of area at cessation of molten surface effects (1200X SEM)	65
46.	Sandblasted copper. Surface view seen at 45 degrees from normal (1200X SEM)	67
47.	Copper. Scintillation pattern produced by x-rays from silica coating on copper surface seen in previous figure (1200X SEM)	67
48.	316 Stainless. Main laser impact crater (240X SEM)	68
49.	316 Stainless. Typical molten surface effects produced by laser irradiation (650X SEM)	68
50.	316 Stainless. Unipolar arcing found at 2.0mm from main laser impact crater (650X SEM)	69
51.	316 Stainless. Unipolar arcing found 2.7mm from main laser crater (620X SEM)	69

52.	1030 Steel. Main laser impact crater (125X SEM)	71
53.	1030 Steel. Unipolar arcs found at 2.0mm distance from main laser crater (1250X SEM)	71
54.	Metallic glass. Typical surface effects seen near laser "burn through" edge (520X SEM)	75
55.	Metallic glass. Area near the cessation of surface effects (0.35mm) (1000X SEM)	75
56.	Metallic glass. Close up of unipolar arc and molten surface effects near laser "burn through" edge (2100X SEM)	76
57.	Recrystallized MetGlas. Typical molten surface effects seen near laser "burn through" edge (520X SEM)	76
58.	Recrystallized MetGlas. View of hole, produced by beam irregularity, and the nearby surface effects (500X SEM)	77
59.	Recrystallized MetGlas. Areas of unipolar arcing found 1.2mm from laser burn through (500X SEM)	77
60.	304 Stainless. Plasma produced at 18 MW/cm^2 energy density	79
61.	304 Stainless. No plasma produced at 10 MW/cm^2 density	79
62.	304 Stainless. Typical burn pattern seen at low energy densities- 25 MWatt/cm^2 (2600X SEM)	80
63.	304 Stainless. Main laser crater produced by pulse number two (130X SEM)	80
64.	304 Stainless. Main crater two seen at a higher magnification (260X SEM)	82
65.	304 Stainless. Continuation of main crater number two sequence (650X SEM)	82

66.	304 Stainless. Unipolar arcing seen at the cessation of diffraction ring phenomenon (130X SEM)	84
67.	304 Stainless. Area shown in the previous figure at a higher magnification (260X SEM)	84
68.	304 Stainless. Area shown in previous figures at a higher magnification (650X SEM)	85
69.	304 Stainless. Acid etch of unipolar arcs and molten surface effects (650X SEM)	85
70.	304 Stainless. Acid etch of unipolar arcs showing different effects (650X SEM)	86
71.	304 Stainless. Main crater number two from the second three-shot sequence (260X SEM)	86
72.	304 Stainless. Unipolar arcing 2.5mm from the third laser pulse (260X SEM)	87
73.	304 Stainless. Surface produced by a seven pulse sequence (130X SEM)	87
74.	304 Stainless. Same surface area as previous figure but at higher magnification (260X SEM)	89
75.	304 Stainless. Surface produced by seven pulse sequence, 5mm from previous figure (260X SEM)	89
76.	304 Stainless. Same surface as previous figure but at higher magnification (650X SEM)	90
77.	304 Stainless. Another surface view from seven pulse sequence (650X SEM)	90
78.	304 Stainless. Close up of molten surface effects from seven pulse sequence, same area as in previous figures but at greater magnification (1300X SEM)	91

79.	304 Stainless. Unipolar arcing seen at cessation of molten surface effects for seven pulse sequence (260X SEM)	91
80.	304 Stainless. Etched cross section of seven pulse sequence. Note crystal structure crosses crack line (500X optical) ..	92
81.	304 Stainless. Etched cross section of seven pulse sequence. Note main laser crater rim in cross section (500X optical).	92
82.	304 Stainless. Etched cross section. Main laser crater shown in previous figure lies immediately to the left (500X optical)	93
83.	304 Stainless. Etched cross section. Crystalline microstructure can apparently be seen extending up to the surface (500X optical)	93
84.	304 Stainless. Etched cross section. Ridge-like structure corresponds to molten surface effects (500X optical)	94
85.	316 Stainless. View (center) of main laser impact crater resulting from pulse three (650X SEM)	97
86.	316 Stainless. View (center) of main laser impact crater resulting from pulse two and after exposure to plasma produced by pulse three (650X SEM)	97
87.	316 Stainless. Unipolar arcing seen at distance 2.5mm from main laser impact crater number three (650X SEM)	98
88.	316 Stainless. Molten surface effects resulting from pulse two, 2mm from main laser impact crater of pulse three, after exposure to plasma produced by pulse three (650X SEM)	98
89.	HY 130. Area between and around main impact craters from pulses one and two (160X optical)	100

90.	HY 130. Area near main laser impact crater number two (500X optical)	100
91.	1030 Steel. Main laser impact crater of pulse two after exposure to plasma produced by pulse three (125X SEM)	102
92.	1030 Steel. Close up of area in main crater two (600X SEM)	102
93.	1030 Steel. Close up of area in main crater two (600X SEM)	103
94.	1030 Steel. Unipolar arcing seen from distance of 2mm from main laser impact crater three (600X SEM)	103
95.	1030 Steel. Main laser impact crater produced by pulse two, after exposure to plasma produced by pulse three; in second three shot sequence (120X SEM)	104
96.	1030 Steel. Close up of area seen in upper left corner of main crater seen in previous figure (1100X SEM)	104
97.	1030 Steel. Unipolar arcing at distance of 2.4mm from main laser impact crater three (1100X SEM)	105

ACKNOWLEDGEMENTS

I am especially grateful to Mr. Robert Sanders and Mr. Tom Kellog for their help and support. Robert Sanders was particularly valuable for his support in the operation of the neodymium glass laser and target chamber vacuum system. While Tom Kellog's aid in target preparation, etching, and mounting, along with his training in the operation of the Scanning Electron and Zeiss Microscopes, and their associated photographic systems was greatly appreciated.

Most importantly, I would like to thank Professors Schwirzke and Challenger for their help and guidance, without which my research and thesis work would not have been possible.

Finally, I would like to thank my wife, Linda, for her support during my two years here at the Naval Postgraduate School, for her involvement in typing both the "rough" and the "final", and for correcting the sometimes atrocious spelling and sentence constructions of this thesis.

I. INTRODUCTION

The study of the interaction of a hot plasma with material surfaces is becoming increasingly important. If magnetically-confined fusion plasmas are ever to be used in the production of electrical power, plasma-surface interaction difficulties are going to have to be solved. Two major problems are apparent, first that the inner or first wall of the fusion reactor vessel can be damaged by the plasma and its reaction products, and second, the introduction by plasma-wall interactions of high Z particles into the plasma, which in turn will cool the plasma through Bremsstrahlung losses, to a point where fusion can no longer be sustained.

Three major damage mechanisms have been noted for a hot plasma in contact with a material surface. First, evaporation of the surface material, primarily due to the absorption of radiant heat from the plasma. This phenomenon can be accurately predicted knowing the wall composition, equilibrium vapor pressure for the material, and surface temperature. Second, sputtering by D, T, He ions or neutrals. When any of these strike an atom of the first wall, a collision cascade of lattice atoms is produced and sputtering results [Ref. 1]. Third, and most importantly, is the phenomenon of unipolar arcing, which can occur when a hot plasma and a conducting inner wall are in contact. An electrical arc is established between the wall and the plasma, with the plasma acting as both the anode and the cathode.

Unipolar arcing has been observed in DITE and Russian Tokamaks [Ref. 2], and recently in PLT, ISX, Macrotor, and Pulsator Tokamaks [Ref. 3], with erosion due to unipolar arcing at least two orders of magnitude greater than that caused by sputtering.

Also of note is the determination of the importance of plasma-surface interactions in targets of high energy laser weapons systems. As noted by Ryan and Shedd [Ref. 4], plasma-surface interactions could be more damaging to the target than direct laser surface interaction damage mechanisms, with unipolar arcing being the predominant mechanism of energy transfer from the plasma to the target surface. If this is the case, it becomes important to study the arcing mechanism, and discover materials and surface preparations that are resistant to unipolar arcing; thus minimizing the effect of an enemy's laser weapons.

Similar to Ryan and Shedd's study, the emphasis of the study reported by this thesis is the determination of the unipolar arcing susceptibility of various metals, metallic glasses and Poco graphite with a variety of surface preparations or surface hardening methods employed. The samples investigated were stainless steel type 304 with polished and sandblasted preparations, stainless steel type 316, a mild commercial steel type 1030, titanium, sandblasted copper, Poco graphite, HY 130 steel, and a metallic glass $\text{Fe}_{80}\text{B}_{20}$. "Laser glazed" surfaces were also prepared on both stainless steel types, on HY 130, and on the 1030 steel, and their susceptibility to arcing and their structure were investigated.

II. BACKGROUND

A. UNIPOLAR ARC PROBLEM

The problem of effects produced by plasma-surface interactions has been of interest since the beginning of controlled fusion programs. Interest in unipolar arcing has increased in the past few years, as a result of reports of unipolar arcing in the DITE Tokamak [Ref. 2], the PLT, ISX, Macrotor, and Pulsator Tokamaks [Ref. 3]. Unipolar arc damage has been found on test probes, limiters, and on the first wall in these fusion test machines, and has been shown to be the dominant damage mechanism.

While not of a structural concern, because of the small amount of surface material removed during the arcing process; unipolar arcs, due to their large numbers, are the primary source of high Z impurities in the fusion plasma. When the amount of these high Z impurities exceeds a certain level, energy losses due to radiation become so great that the plasma is cooled below fusion temperature. With this in mind, it is evident that control of the unipolar arc problem is vital to the ultimate fruition of controlled fusion programs. Current studies, like those here at the Naval Postgraduate School, are aimed at discovering structural materials and methods of surface preparation that inhibit unipolar arcing.

B. UNIPOLAR ARC MODEL

The model described in this thesis is the one proposed by F. Schwirzke and R. Taylor in 1978. A thorough treatment and discussion of all current unipolar arc models; and the initiation and cessation of unipolar arcing can be found in Ryan and Shedd's thesis, entitled A Study of the Unipolar Arcing Damage Mechanism on Selected Conductors and Semiconductors.

The condition of quasi-neutrality in a plasma leads to the formation of a sheath potential whenever a plasma comes into contact with a wall. The width of the sheath is approximately that of a Debye length (λ_D) and is given by:

$$\lambda_D = (kT_e / 4\pi n_e e^2)^{\frac{1}{2}}$$

while the plasma assumes a sheath potential with respect to the wall of [Ref. 5]:

$$V_f = (kT_e / 2e) \ln (M_i / 2\pi M_e)$$

where:

- k = Boltzmann Constant
- T_e = Electron Temperature
- n_e = Electron density
- M_i = Ion Mass
- M_e = Electron Mass
- e = Electron Charge

and the electrical field in the sheath is the order of [Ref. 5]:

$$E_s \approx V_f / \lambda_D = \ln (M_i / 2\pi M_e) (\pi n_e k T_e)^{\frac{1}{2}}$$

Unipolar arcing occurs, with the plasma acting as both cathode and anode, if the electric field strength in the potential becomes high enough to ignite and sustain an arc. Electrons are then emitted from a cathode surface spot on the wall into the plasma. This serves to reduce the nearby plasma potential and less energetic electrons in the plasma can now reach the wall, thus closing the current loop. For this model, a requirement for arcing is an ion density increase over the cathode spot. The ion density can increase due to ionization of neutral atoms released from a hot cathode spot [Ref. 5].

A number of mechanisms exist that can lead to production of a hot spot, including surface protrusions and inclusions in the wall which produce localized electrical field enhancement. This enhancement will lead to increases in the ion flux rate from the plasma to the cathode spots which produce localized heating due to ion bombardment and recombination, and evaporation of a wall metal as well as desorption of gases and vaporization of oil films which enter the plasma. A fraction of these neutrals will be ionized, then accelerated by the sheath potential and fall back onto the cathode spot. This serves to increase the ion bombardment rate, acting as a feedback mechanism to further spot heating and evaporation and to increase the electron emission from the hot cathode spot. Sheath width is subsequently reduced while the electric field increases due to increases in local plasmas density and pressure [Ref. 5].

The locally increased plasma pressure above the cathode spot serves to produce a radial electric field (E_r) tangential to the surface where E_r is given by [Ref. 5]:

$$E_r = -(kT_e/e)(1/n)(dn/dr)$$

This field acts to reduce the potential in a ringlike area about the cathode spot. The lowered sheath potential allows more electrons to reach the surface, thus closing the unipolar arc current loop. A diagram of this model is seen in figure 1.

C. METALLIC GLASSES

All metals found in everyday use exist in the crystalline state, rather than an amorphous one, because the crystalline structure always has a larger binding energy. For a metal to form an amorphous state, it must be cooled to a temperature threshold called the glass temperature. Unfortunately, the glass temperature is always well below the freezing point of the metal where crystallization begins. Thus, when the liquid is cooled, it crystallizes long before the glass has a chance to form [Ref.6].

Amorphous metallic structures can be created by cooling a liquid metal rapidly through the liquidus temperature to below the glass temperature. If the cooling rate is rapid enough, no time will be available for the formation and growth of nucleation centers. Quenching rates required for production of metallic glasses are on the order of 10^6 °C/sec for most alloys.

The primary method used to obtain these quench rates is the one employed in the production of the first metallic glass, and is called melt spinning. Molten metal is sprayed onto a rapidly rotating metal disc which is held at room temperature. The liquid is thereby drawn into a thin ribbon about three to five microns in thickness.

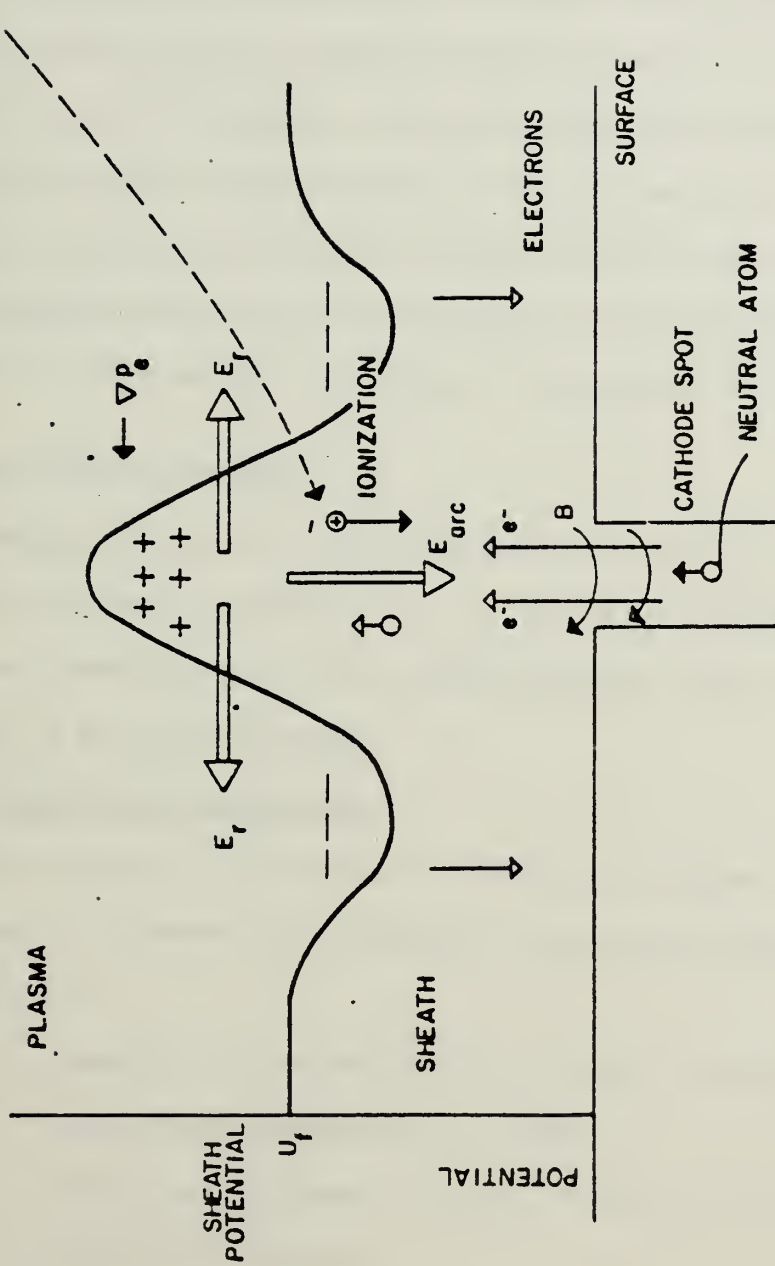


Figure 1. Unipolar arc model

The thin metal ribbon, being in contact with a relatively massive heat sink, solidifies at an extremely rapid rate with quenching rates exceeding 10^6 °C/sec.

Metallic glasses have similar properties to that of the crystalline alloy. Two properties are different and may play a role in the resistivity towards unipolar arcing displayed by metallic glasses. One, there are no grain boundaries in the amorphous alloy, and it is this property that makes metallic glasses corrosion resistant. Two, the electrical resistivity in metallic glasses, while low, usually is an order of magnitude above the resistivity of the crystalline alloy; though it is about one half the value of the liquid [Ref. 7].

D. LASER MATERIAL PROCESSING

The physics of laser-surface interactions is quite complex and shall be discussed only generally. The results of laser-surface interactions are sometimes quite novel and interesting, and a number of these results shall be discussed.

1. Laser-Target Interaction

The process of laser-target interaction, whether the interaction takes place in a vacuum or at atmospheric pressure, follows these steps [Ref. 8]:

- a. Absorption of electromagnetic radiation within a skin depth
- b. Heating and vaporization of surface
- c. Electrical breakdown in vapor, plasma production
- d. Expansion of plasma
- e. Generation of plasma shock waves
- f. Momentum transfer to target from moving plasma

- g. Generation of shock wave (stress-wave) in target
- h. Late burn off of material by the hot plasma
- i. Dissipation

The initial radiation falls on the target surface and interacts with the conduction band electrons in the skin depth. These electrons respond collectively to the field and the energy absorbed through free-free transitions or electron collisions with imperfections. The skin depth is a function of the wavelength of the incident radiation (wavelength λ), the plasma frequency for the conduction band electrons (ω_p), refractive index (k), and electron collision time (τ). The skin depth, δ , is given by:

$$\delta = \frac{\lambda}{4\pi k(\omega, \omega_p, \tau)} \approx \sqrt{\frac{\rho}{\pi \mu \nu}}$$

where:

ρ = density

μ = permeability of the material

ν = radiation frequency

For 304 stainless, the skin depth of 1.06 μ m radiation is approximately 260 angstroms.

As the radiation is absorbed and surface temperatures in the focal spot start to rise, a decrease in the reflectivity occurs, enabling further radiation to be absorbed till melting and then vaporization of the surface is achieved, with an evaporation rate given by:

$$R_e \approx \exp(-w/kT)$$

where:

w = Binding energy

k = Boltzmann constant

T = Temperature

Ionization of the vaporized material is approximately one percent (1%) according to the SAHA equation [Ref. 8]:

$$\alpha = \sqrt{2P_i P_n} \cdot \left((kT)^{3/4} / \sqrt{n} \right) \cdot (2\pi m_e / h)^{3/4} \exp (-eV_i / kT)$$

P_i and P_n are partition functions for the ions and neutrals.

Absorption of the laser radiation in this gas proceeds via inverse Bremsstrahlung. As evaporation proceeds and gas breakdown occurs, a well developed plasma profile develops, and laser radiation may be entirely cut off from the surface. The plasma plume expansion rate is about 10^5 m/sec and the target material now starts to ablate due to plasma-surface interactions.

The radiation pressure of the incident laser pulse and the pressure and shock caused by recoiling material can be tremendous over very short time scales. A simple calculation of the surface pressure involved would show a plasma exerted pressure on the order of 1.58×10^5 atmospheres, with $n_e = 10^{21}/\text{cm}^3$, and $kT = 100\text{eV}$ using the formula [Ref. 9]:

$$P = n_e kT$$

where:

n_e = Plasma density

k = Boltzmann constant

T = Plasma temperature

A more in depth analysis of the physics involved provides an expression for the surface pressure during laser-target interaction to be [Ref. 8]:

$$P = (F_0 \sqrt{kT_v/m}) / (L_v + CT_v)$$

where:

F_0 = Absorbed power density

k = Boltzmann constant

T_v = Vaporization temperature

m = Mass of target material

L_v = Latent heat of vaporization

C = Specific heat of solid

Actual physical measurement of the surface pressures involved during laser-target interaction has been done by a number of researchers. Ready [Ref. 10] found that, for a laser energy density of 2.3×10^8 W/cm², a peak surface pressure of approximately 100 atmospheres was obtained using a 303 stainless steel target. Krehl et.al. [Ref. 11] found that, for a laser energy density of about 2×10^9 W/cm², a peak surface pressure of approximately 780 atmospheres was obtained using an aluminum target, while Schriempf [Ref. 12] writes that a 100 Megawatt peak power pulse, absorbed in an area of 10^{-4} cm², exerts a pressure of approximately 300 atmospheres.

With energy densities on the order of 10^{10} W/cm² for these experiments, it is felt that surface pressures on the order of 15,000 psi were obtained. Though the 15,000 psi pressure is below the fracture strength of the various steels used for this thesis, it is certainly in the elastic deformation regime.

2. Laser Processing Results

The techniques used in laser processing of materials include transformation hardening, deep-penetration welding, drilling, laser

glazing and shock hardening. Of particular interest and relevance to this thesis, are the surfaces produced by laser glazing and shock hardening.

The technique used for laser glazing involves rapidly traversing the surface of a material with a laser beam focused so that a power density of 10^4 to 10^7 W/cm² is obtained at the material's surface. Laser shock hardening attempts to work-harden materials with the blast wave that accompanies rapid surface vaporization induced by pulsed lasers at very high power densities, over 10^9 W/cm². Though laser glazing was not strictly done in this thesis's experiments because of the use of a pulsed laser, quenching rates were of the same order, while power levels were on the order of 10^{10} W/cm².

The procedure used in laser glazing results in a thin melt layer with the substrate remaining cold. With the steep temperature gradients involved, rapid solidification of the thin melt layer takes place, with quench rates in excess of 10^8 °C/sec for melt layers of one to ten (1 - 10) microns thickness. Obviously, with quench rates that rapid, production of amorphous films are easily obtainable in certain alloys.

Using the laser glazing process on M2 tool steel, with a quench rate of approximately 5×10^5 °C/sec, a glazed surface layer displayed an extremely refined and homogeneous microstructure. The layer consisted of a two-phase matrix of δ ferrite and austenite (γ) with a low concentration of fine carbide particles [Ref. 13]. Laser glazing

M50 alloy steel, but at a faster quenching rate, produced similar results with only very fine carbide particles being resolved in the melt layer at high magnifications, and a hardness increase of 200 DPH (diamond pyramid hardness) over the substrate [Ref. 14].

Shock hardening techniques produce similar and sometimes greater increases in hardness than the laser glazing technique. It has been noted that martensite can be induced to form in the austenitic stainless steel type 304 but not type 316 [Ref. 15] by cold working; and, it seems plausible that surface layers of martensite can be formed by laser shock hardening 304 stainless and possibly other steels as well. It is expected, though not in the case of 304 stainless, that the hardened regions will be more corrosion resistant than the base metal due to the homogeneity of the hardened surface layer [Ref. 14].

III. EXPERIMENTAL DESIGN

A. EQUIPMENT

The equipment used for experimentation included a medium power neodymium glass laser and an evacuated target test chamber, a scanning electron microscope, and two optical microscopes; the latter being used to study surface damage on test samples. Figure 2 is a schematic of the laser and test chamber.

The optical microscopes were used to study the surface preparation of all test samples. The neodymium glass laser was used to irradiate sample targets in the test chamber, thus generating a hot plasma. After exposure to the laser-produced plasma, each target was studied using both the optical and scanning electron microscopes to determine the degree of plasma-surface interaction.

1. Laser

A KORAD K-1500 Q-switched neodymium doped glass laser, with a wavelength of $1.06\mu\text{m}$, was the source of energy for producing a hot dense plasma over the target surfaces. A detailed description is given by Davis [Ref. 16]. Figure 2 is a block diagram of the basic system. The output energy of the laser was variable in the range of 0.2 - 15 Joules with a nominal 25 nanosecond pulse width. For these experiments the laser was operated at an output of approximately 8 - 15 Joules on target with focal spot sites varying from 0.5×10^{-2} to 0.2cm^2 . For metallic glass experiments, filters of varying transmittance were inserted. Laser total output energy was measured using a laser precision RK - 3200 Series Pyroelectric meter.

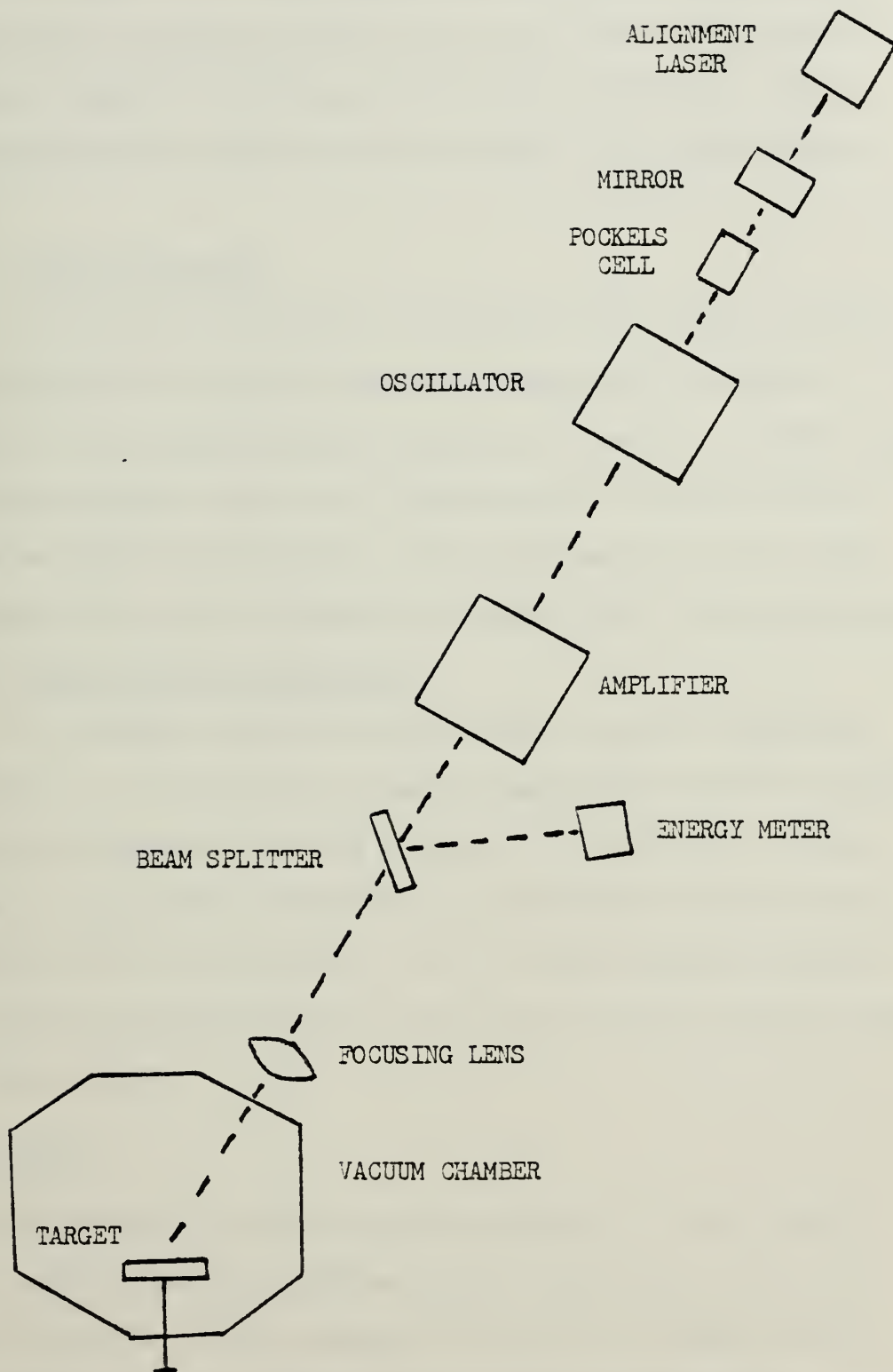


Figure 2. Laser and test chamber arrangement

2. Target Test Chamber

The target test chamber used was a six-inch cube of unbaked aluminum with an internal volume of 12.9 ± 0.3 liters. The vacuum system was capable of providing pressure down to 10^{-7} Torr. Laser beam alignment was 30 degrees from the normal of the target surface face.

3. Optical Microscope

A Bausch and Lomb Balplan stereoscopic light microscope and a Zeiss microscope were used to observe and photograph the target surfaces. Optical magnification available was from 100 to 1000X, with most work being done in the 100 - 200X range due to depth of field problems at higher magnifications. These microscopes were also used to determine the depth of unipolar arc craters after laser irradiation.

4. Scanning Electron Microscope

The scanning electron microscope (SEM) used was a Cambridge Stereoscan S4 - 10, which has a range of magnification of 20 to 100,000X with most observations conducted in the 200 - 1300X range. The SEM provides a large depth of field, that is much better than the optical microscopes, and is an invaluable tool for surface damage evaluation. Also used with the SEM system was a Princeton Gamma Tech energy dispersive x-ray analyzer.

B. PROCEDURES

The experimental procedures can be separated into three distinct steps: target preparation, plasma-surface interaction, and surface damage evaluation. Target preparation consisted of target machining (if necessary), target polishing using standard metallographic

procedures, and target examination under the optical microscope after polishing. The second step of plasma-surface interaction was then accomplished in the plasma laboratory of the Naval Postgraduate School using the neodymium glass laser and target test chamber with varying pressure conditions. Surface damage evaluation was accomplished by examination of each sample under both the SEM and the optical microscopes.

1. Target Preparation

The targets consisted of 1030 mild commercial steel, type 304 and type 316 stainless steels, titanium, copper, carbon graphite, HY 130, and $\text{Fe}_{80}\text{B}_{20}$ metallic glass ribbon. The 1030, 304, 316, Poco, HY 130, and titanium targets were polished using standard metallurgical techniques with a final polishing slurry of $0.05\mu\text{ Al}_2\text{O}_3$. The carbon graphite targets were shot unpolished and polished. The copper and some stainless steel (304) targets were sandblasted using 300 grit 84% silica at an operating pressure of 85 psi. All commercial metallic glass targets were shot as received, with no surface preparation other than acetone cleaning. All targets were examined optically prior to irradiation at magnifications to 400X for comparison with target surfaces after plasma exposure.

2. Plasma-Surface Interaction

Each target was cleaned with ethyl alcohol and then acetone prior to being mounted in the test chamber. The target chamber was then evacuated to a pressure of 10^{-6} Torr and the laser fired at energy levels varying from 8 to 15 Joules with a nominal pulse width in the Q-switched mode of 25 nanoseconds. Breakdown of target surface material

was achieved, producing a hot ($kT_e \approx 100\text{eV}$), dense ($n_e \approx 10^{21}/\text{cm}^3$), and approximately hemispherically shaped plasma which established the sheath potential, relative to the target surface, necessary for unipolar arcing. No external voltage was applied.

3. Surface Damage Investigation

Specimens were examined and photographed using the optical and scanning electron microscopes. Unipolar arc damage, if any, was evaluated, crater density determined, and arc crater depth at various radii from crater center measured. The depth of molten surface effects was measured using an etched target cross section.

IV. EXPERIMENTAL RESULTS

Plasma-metallic surface interactions were evaluated using targets of types 304 and 316 stainless steel, 1030 mild (Rockwell B of 42) commercial steel, titanium, Poco graphite, sandblasted copper, HY 130, $\text{Fe}_{80}\text{B}_{20}$ (a commercial metallic glass), laser produced surface metallic glasses on types 304 and 316 stainless, 1030, and HY 130 steels, and $\text{Fe}_{80}\text{B}_{20}$ metallic glass that had been annealed for two hours at 380°C to allow crystallization of the glass to begin.

A. CONDUCTORS

1. Titanium

99.9% pure titanium targets were shot both at 10^{-6} Torr and at atmospheric pressures. Laser energy on target varied from 11 to 14 Joules with a focal spot diameter range of 0.4 to 0.6mm. The main laser crater size averaged 0.7mm in diameter with subsequent molten zone extending an average distance of 0.35mm from the main crater. Diffraction of the laser light by the plasma created a series of molten concentric rings about the main crater out to an average radius of 1.0mm from the laser crater rim. Total area of the plasma-surface interaction region averaged 45mm^2 , 20mm^2 more than the stainless steels affected region, even though titanium has a slightly higher melting point (1675°C vs. 1595°C). Figure 3 is a photograph of a main laser impact crater showing the outward flow of once molten material, while figure 4 shows an example of the diffraction produced concentric rings.



Figure 3. Titanium. Typical main laser impact crater and molten surface effects (100X optical)

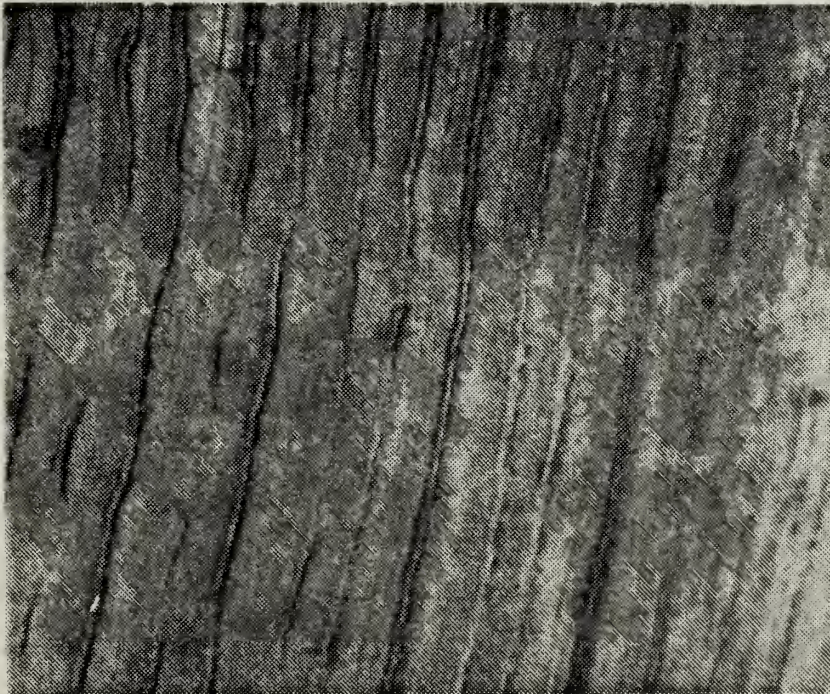


Figure 4. Titanium. Concentric rings of molten material apparently produced by diffraction of laser pulse (200X optical)

Figure 5 shows an area immediately outside the diffraction rings, and the unipolar arcs produced by the plasma surface interaction. This figure shows an area of moderate unipolar arc density with about 570 arcs/cm^2 , with the appearance of the arcs being smoothed over due to the flow of molten metal at the surface layer. Apparently, arcing in this region occurred during the solidification process. It is interesting to note, however, that only in the titanium was arcing found to be taking place over the entire 1.25 cm^2 target surface, albeit at a low arc density. Figure 6 shows unipolar arcs found 3.5mm from the main laser crater rim. It is apparent that the plasma density and temperature required to initiate unipolar arcing in titanium is less than stainless steel, but the amount of crater material removed (damage) and arc density per unit area is less than that of stainless steel. Unipolar arc craters observed at a radius of 2mm or greater from the main laser crater (see figure 6) measured 2.0 to 14.0 μm in diameter, with a depth of 1.0 to 5.0 μm . Irradiation of titanium targets in the atmosphere produced similar effects, but the diffraction ring pattern size was reduced to a diameter of 0.85mm. Unipolar arc densities were approximately the same at the cessation of molten surface effects. Figures 7 and 8 show typical results for laser irradiation of titanium at atmospheric pressure.

2. Poco Graphite

Carbon graphite composites have been suggested for use as limiters in fusion reactors. Poco graphite target material was supplied commercially, and was irradiated both polished and as supplied. Laser pulse energy on target varied from 11 to 15 Joules/pulse. Figures 9

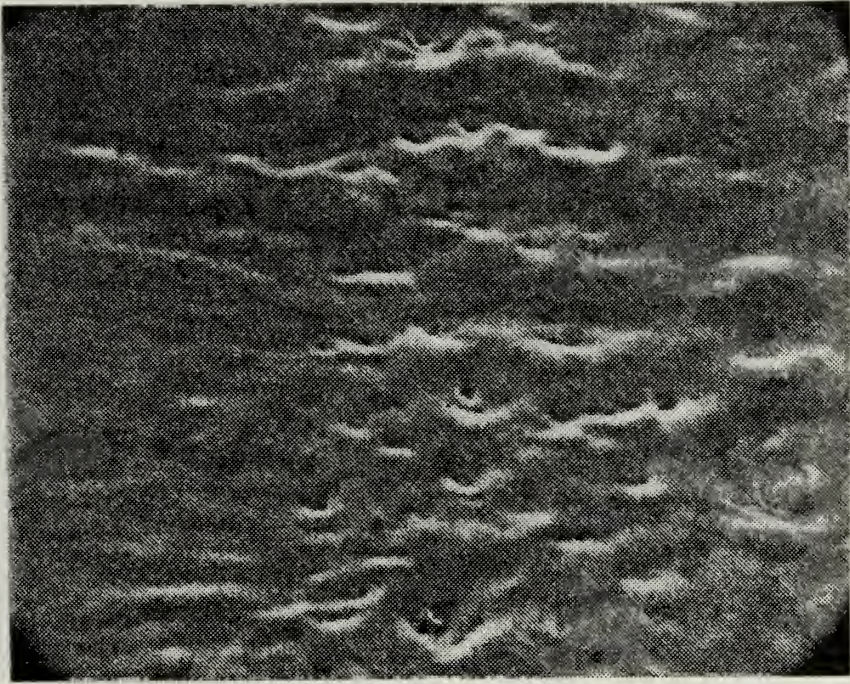


Figure 5. Titanium. Unipolar arcing at the edge of the molten surface effects with 570 arcs/cm^2 (650X SEM)

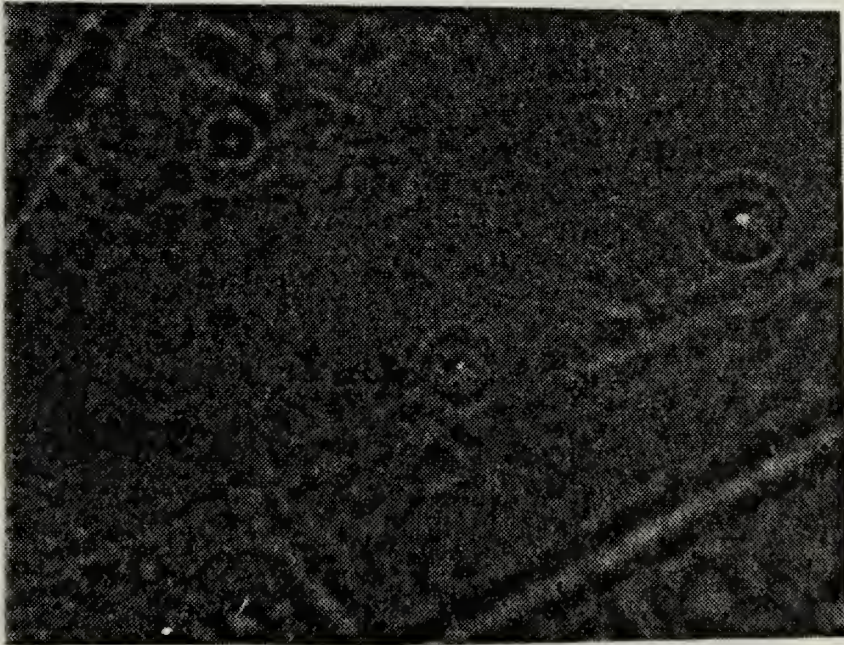


Figure 6. Titanium. Unipolar arcs found at a distance of 3.5mm from the cessation of molten surface effects (500X optical)

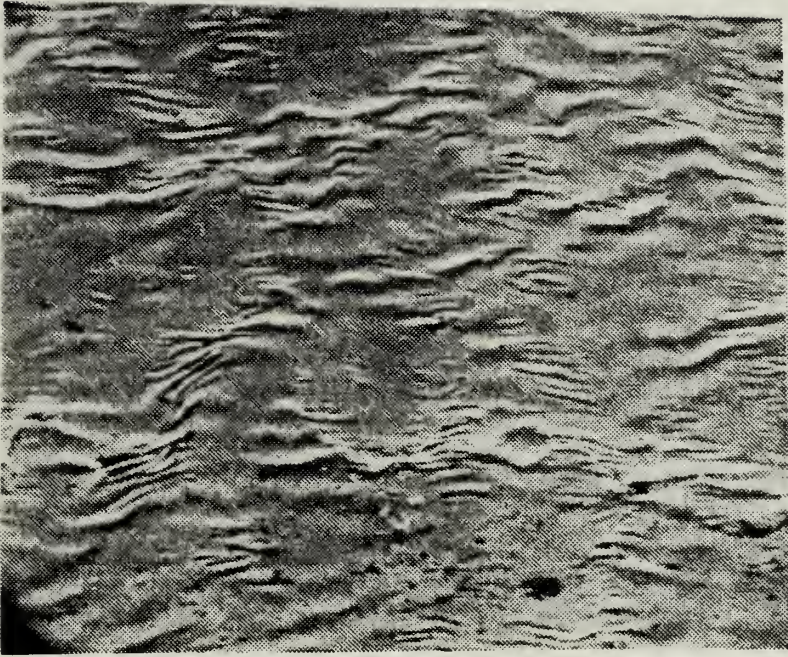


Figure 7. Titanium. Molten surface effects produced by irradiation at atmospheric pressure (240X SEM)

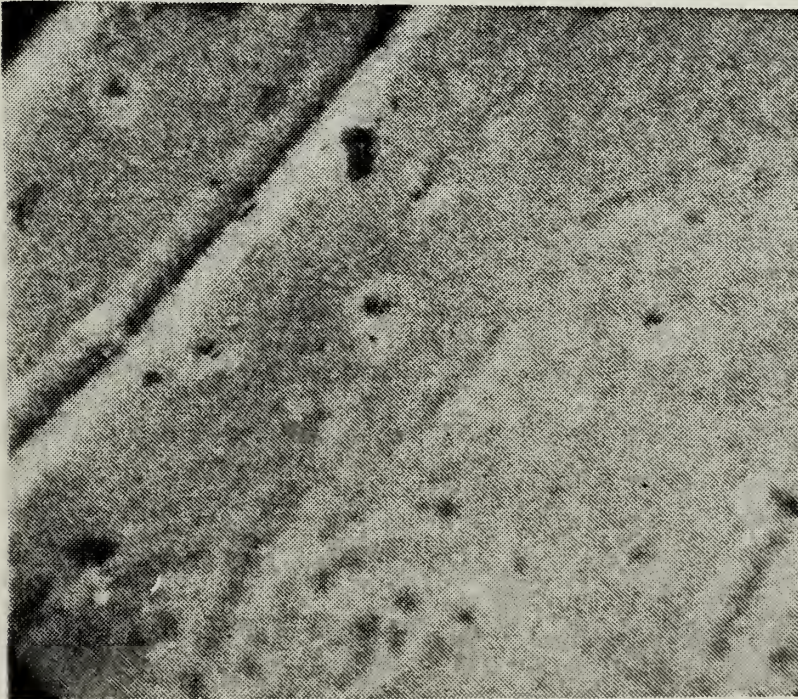


Figure 8. Titanium. Area at the edge of molten surface effects (2400X SEM)

and 10 are SEM photographs at 280 and 1400X magnification respectively, of the target material with no surface preparation, while figures 11 and 12, at 260 and 650X magnifications, show the target surface after polishing with a 0.05 micron slurry of Al_2O_3 . As can be seen, the surface of the material is extremely porous making unipolar arc detection difficult. Figure 13 shows the main laser crater produced by two successive laser pulses of 14 and 15 Joules on target (crater depth measures approximately 0.35mm) while figure 14 shows a view of the crater center at 500X. Figure 15 is a view of the large crack, at 1000X, radiating from the crater center, produced by laser shock effects, a graphic illustration of the brittleness of the material. No areas of unipolar arcing can be seen in these photos, at least no cathode spots could be distinguished amidst the porous surface; however, the surface appears to have undergone erosion or ablation by the plasma, apparently revealing the microstructure of the material. The erosive effect of the plasma can be more clearly seen in figures 16 and 17, which are views, near the main crater's edge, of a polished carbon target that had been irradiated at 11.9 Joules. The edge of the main laser crater can be seen in the upper right hand corner of figure 16, while the erosive effect of the plasma on the carbon surface can clearly be seen in figure 17 when it is compared with the view of a polished unshot surface in figure 12. For the two shot sequence, surface ablation was seen over an approximately elliptical area with a major axis of 8.13mm and a minor axis of 7.08mm. Ablation depth varied radially with a cessation of plasma surface effects at a 4.07mm radius from crater center along the major axis, to a 5 to 7 micron erosion depth of the original surface

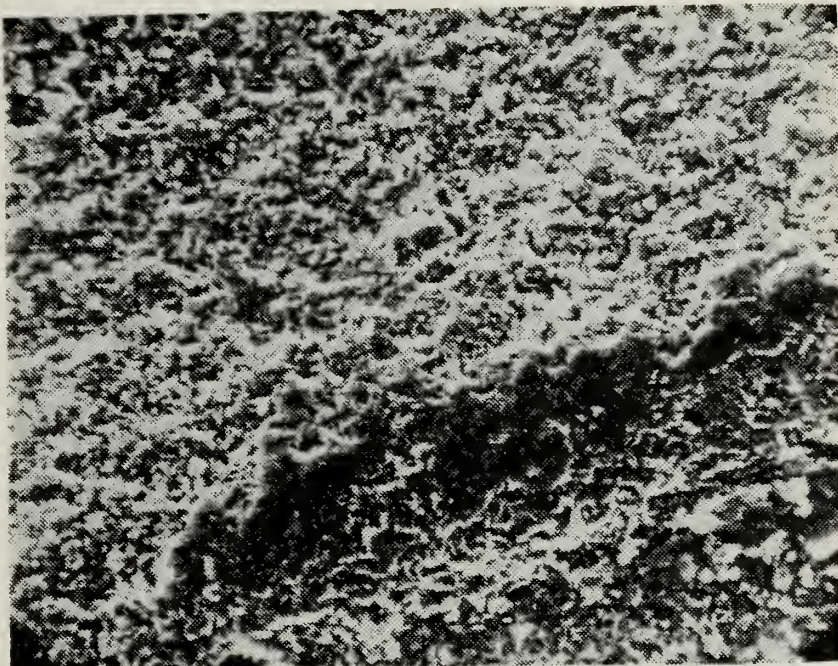


Figure 9. Poco graphite. Unpolished surface
(280X SEM)



Figure 10. Poco graphite. Unpolished surface
(1400X SEM)

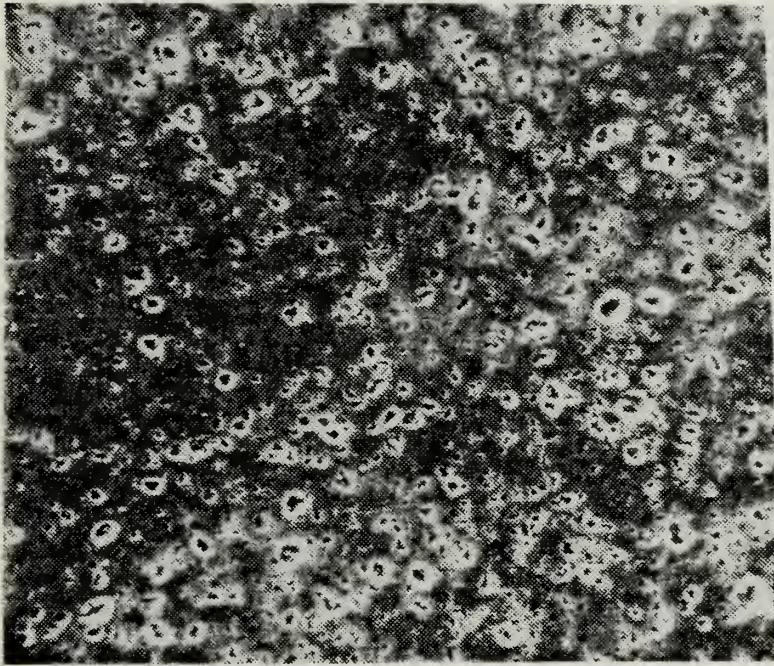


Figure 11. Poco graphite. Surface produced by polishing with a 0.05 μ slurry of Al_2O_3 (260X SEM)

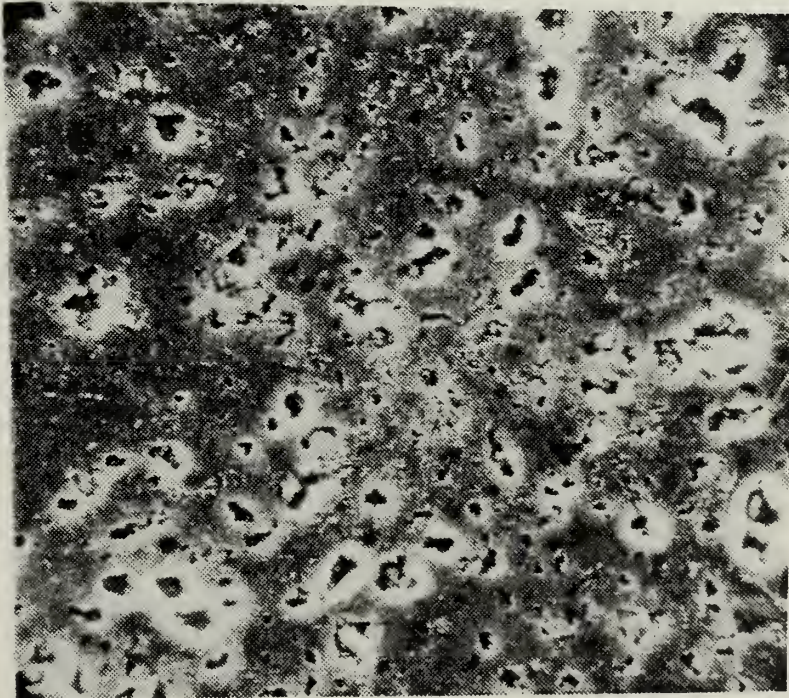


Figure 12. Poco graphite. Polished surface (650X SEM)

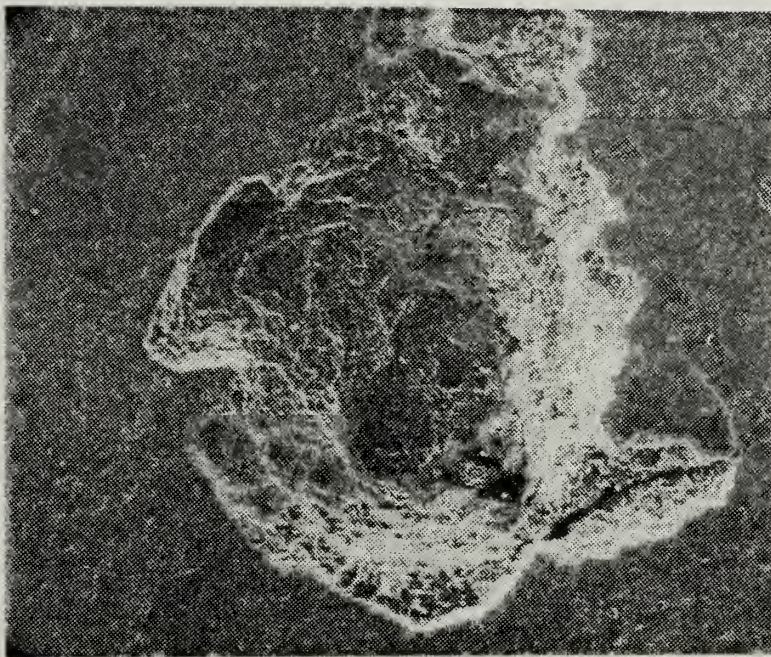


Figure 13. Poco graphite. Main laser impact crater produced by successive pulses of energies of 14 and 15 Joules (50X SEM)

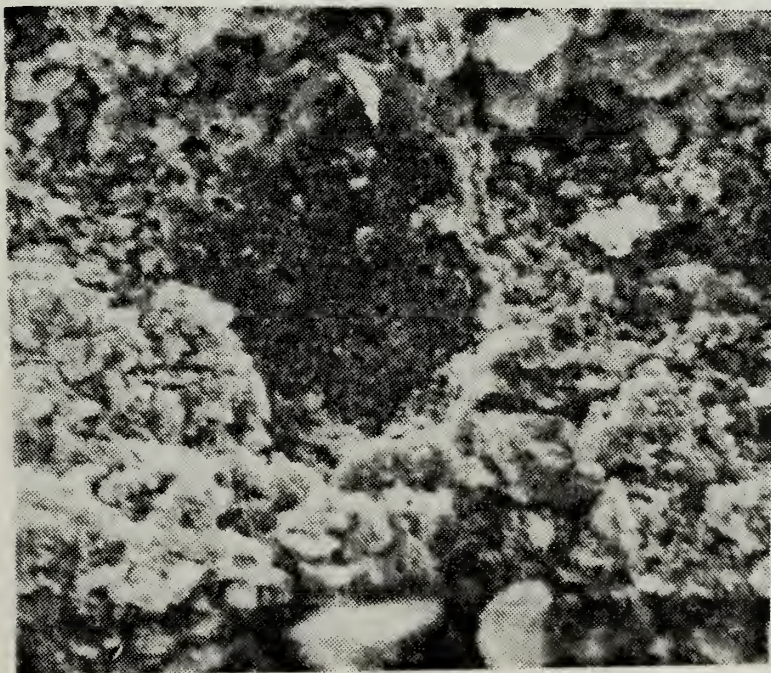


Figure 14. Poco graphite. View of main laser impact crater center (500X SEM)

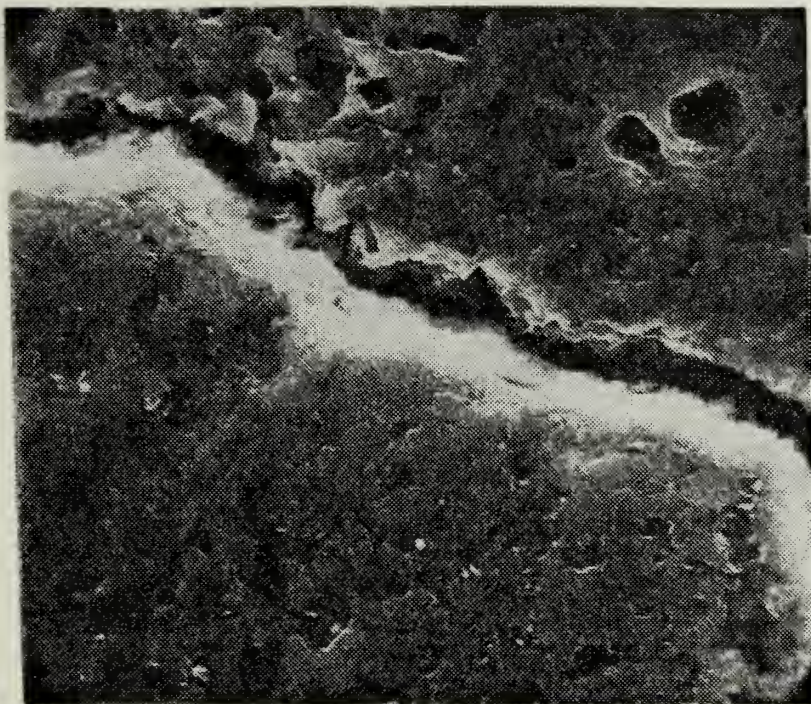


Figure 15. Poco graphite. View of the crack radiating from main laser impact crater (1000X SEM)

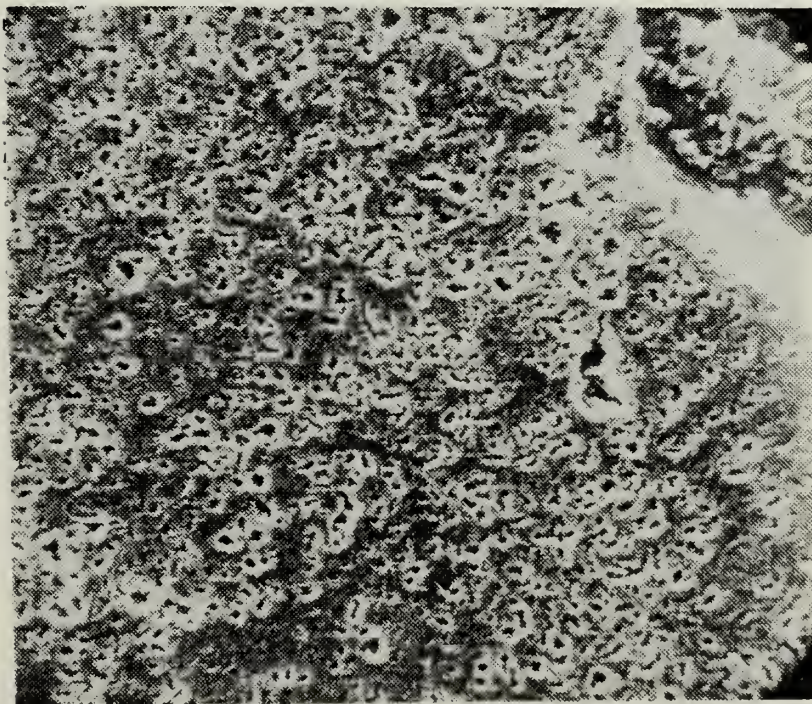


Figure 16. Poco graphite. Polished surface after exposure to plasma. Main laser impact crater edge is visible in upper right hand corner (260X SEM)

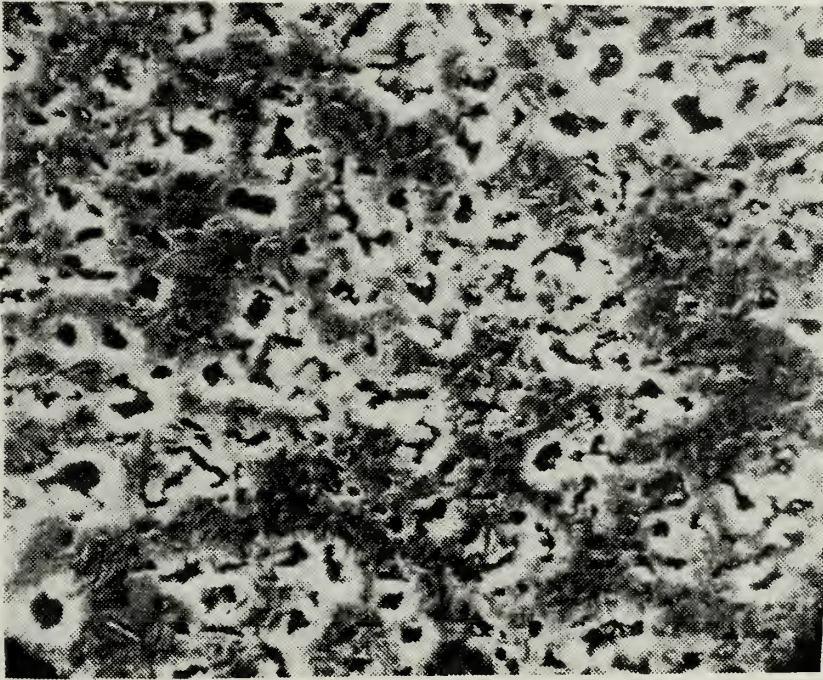


Figure 17. Poco graphite. Close up view of surface shown in previous figure (650X SEM)

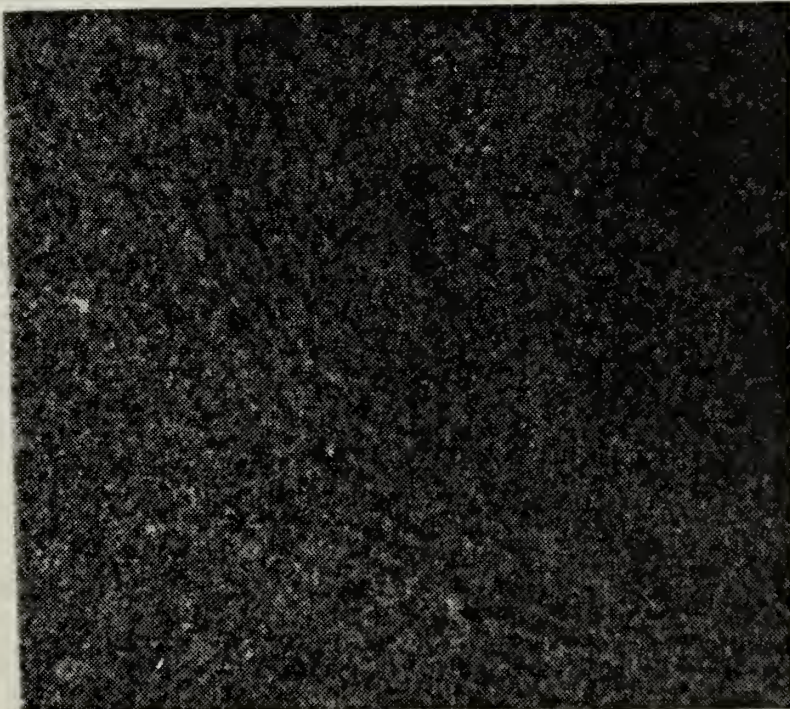


Figure 18. Poco graphite. Main laser impact crater and diffraction rings produced by 11.9 Joule pulse (32X optical)

at the edge of the laser crater. A polished target irradiated at 11.9 Joules, with a focal spot of 0.4mm diameter, had a main crater of 1.5mm diameter and a depth of 0.25mm. The plasma-surface interaction area for this pulse was nearly circular in shape, with surface effects noted at a radius of 3.5mm from crater center. Surface erosion, for this shot, at the edge of the laser crater again was about 5 microns with a series of concentric rings of ablation seen at the edge of the plasma effects.

It was found that the diffraction effect, seen as concentric rings of molten metal or unipolar arcs on the metallic targets, was apparent on carbon targets as a series of concentric rings of ablated material. This tends to confirm that the rings seen on the metals are not solidified surface waves on the once molten material. Figure 18 shows the results of an 11.9 Joule forward shot on a polished target. The concentric rings produced by the diffraction effect can be clearly seen on the left side of figure 18, while figure 19 shows a close up of the rings. The shiny areas in figure 19 correspond to an untouched or still polished surface while the dark areas correspond to the ablated surface. The depth of ablation varied along the rings, but stayed close to an average "peak to trough" depth of 5 microns.

One target, with no surface preparation, was irradiated at an energy of 10.78 Joules and a focal spot diameter of 1mm. The main crater, as seen in figure 20, in this case was not as well defined as the focused shot craters were; however, the area of surface plasma effects was approximately 30mm^2 , which is the same order as the 38mm^2 plasma-surface interaction area for an 11.9 Joule, 0.4mm diameter focal spot, shot. Figures 21, 22, and 23 show an area abutting the edge of the

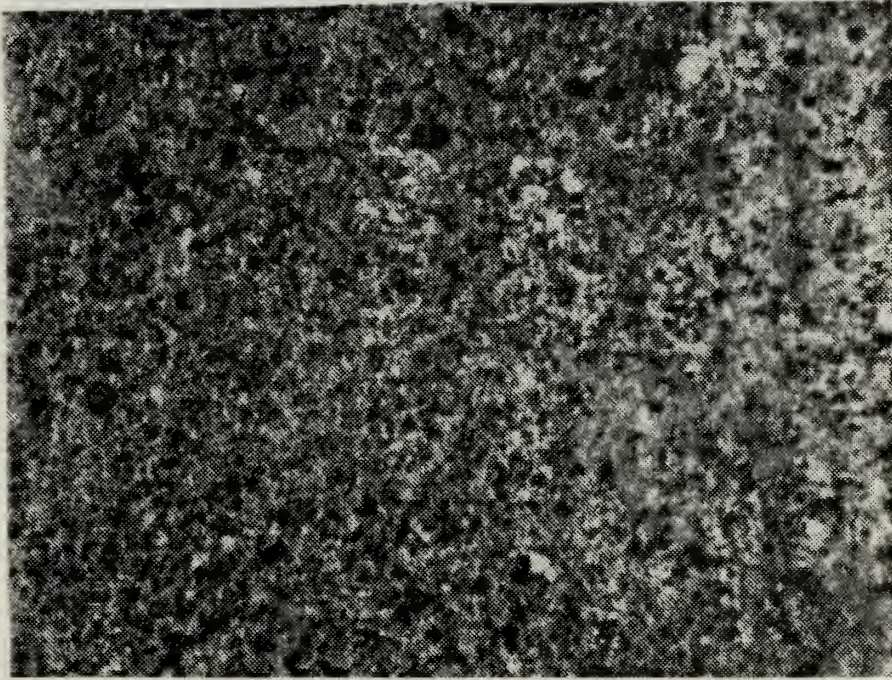


Figure 19. Poco graphite. Close up view of diffracted rings. Bright spots correspond to still polished areas (125X optical)

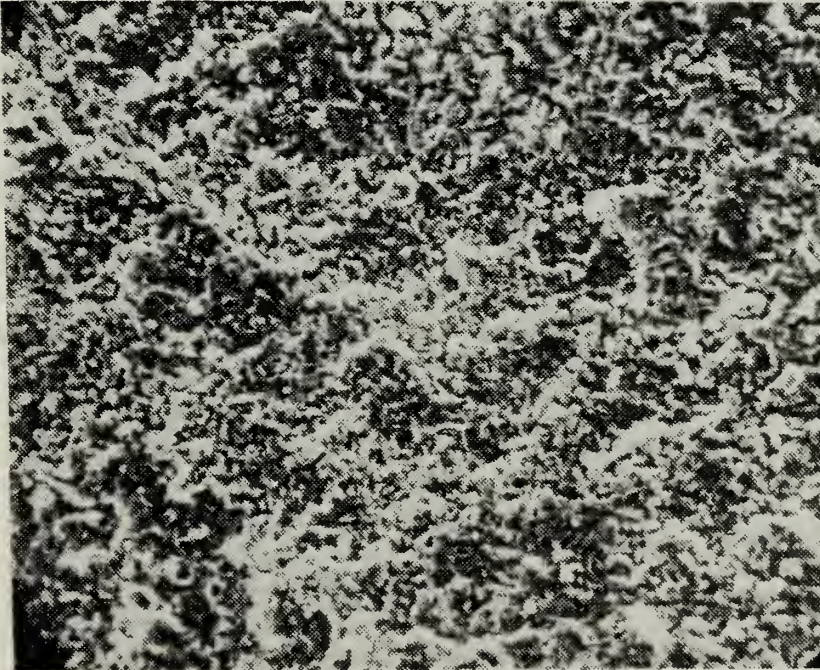


Figure 20. Poco graphite. Unpolished surface after focused laser irradiation at 13.75 Joules (260X SEM)

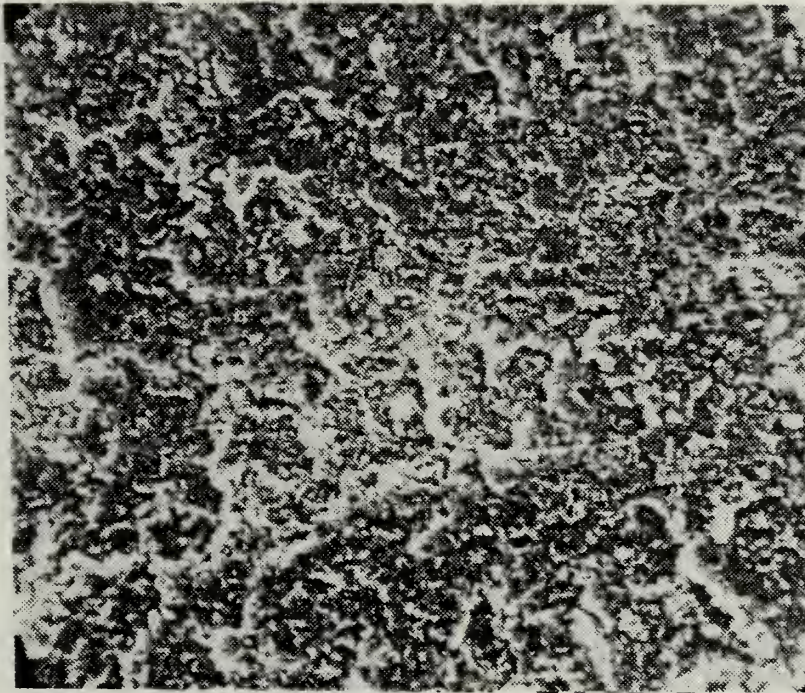


Figure 21. Poco graphite. Unpolished surface area abutting laser impact area (260X SEM)

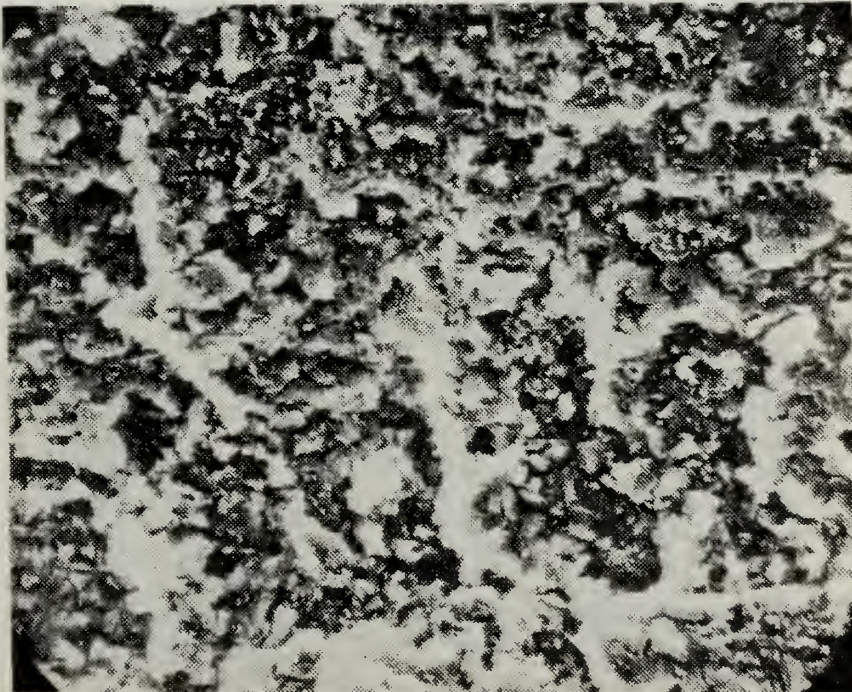


Figure 22. Poco graphite. Unpolished surface shown in previous figure at higher magnification (650X SEM)

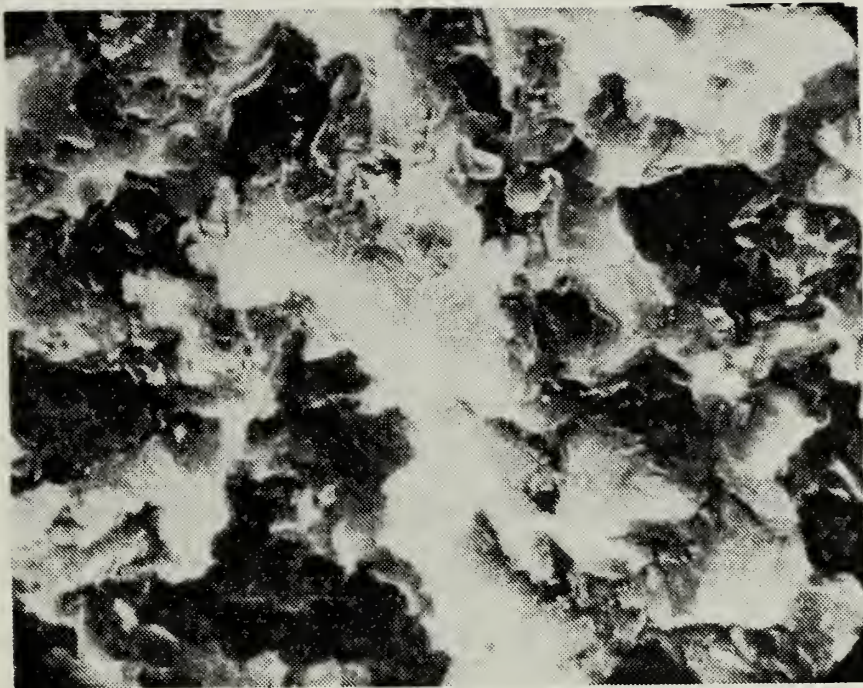


Figure 23. Poco graphite. Unpolished surface, as in previous figure, at higher magnification (2600X SEM)

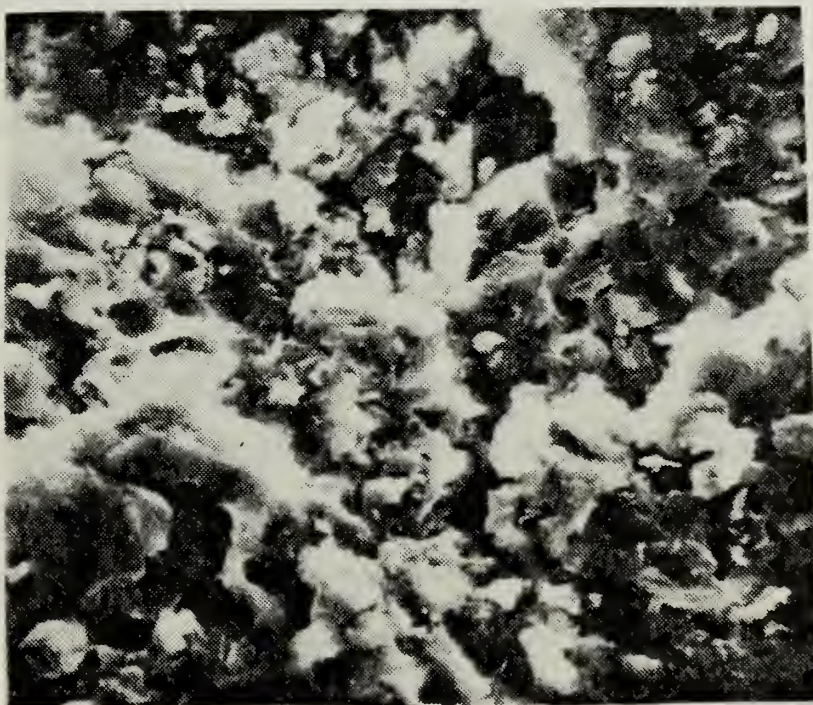


Figure 24. Poco graphite. Unpolished surface area near main laser impact crater (1300X SEM)

main laser crater, at successively higher magnifications, while figure 24 shows an area at 1300X, 1mm away from the laser crater. As in the polished sample shots, some etching of the surface is noticeable at the highest magnifications, revealing the microstructure of the material; and, as with the polished samples, no unipolar arcing effects could be discerned amidst the porous and irregular surface, only erosion effects were noticeable.

3. Type 304 Stainless Steel

Polished 304 targets were irradiated with on target energies varying from 9 to 15 Joules. Average focal spot size was 0.4mm in diameter producing a main laser crater of 0.4 to 0.9mm in diameter (see figure 25) and an average depth of 30 μ m. The plasma damaged surface area averaged in size 20 to 28mm², with an area of molten surface effects of approximately 15mm². Figure 26 shows the periphery, 2.7mm from the main laser crater, of plasma interaction with a unipolar arc crater density of 300/cm². Craters at a distance of 2.5mm from main crater rim measured from 3 to 10 μ m rim to rim diameter, and had a depth of 1 to 6 μ m. Crater densities close in to the main crater appear to exceed 100,000/cm² as previous researchers have noted [Ref. 4]. Figure 27 shows the result of laser pulse diffraction by the plasma, producing concentric rings of molten material about the main crater.

A number of type 304 stainless steel targets were sandblasted with a 300 grit of 84% silica content, at 85 psi, to determine the susceptibility of sandblasted steel to unipolar arcing. Figure 28 shows a typical surface produced by sandblasting stainless steel type 304. After sandblasting, a target was irradiated with two laser pulses of

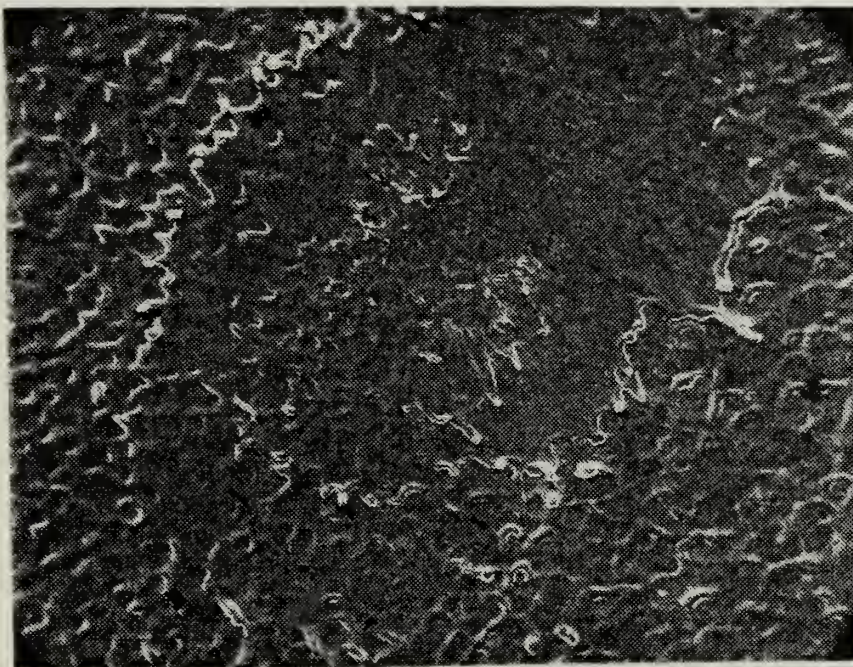


Figure 25. 304 Stainless. Main impact crater (130X SEM)

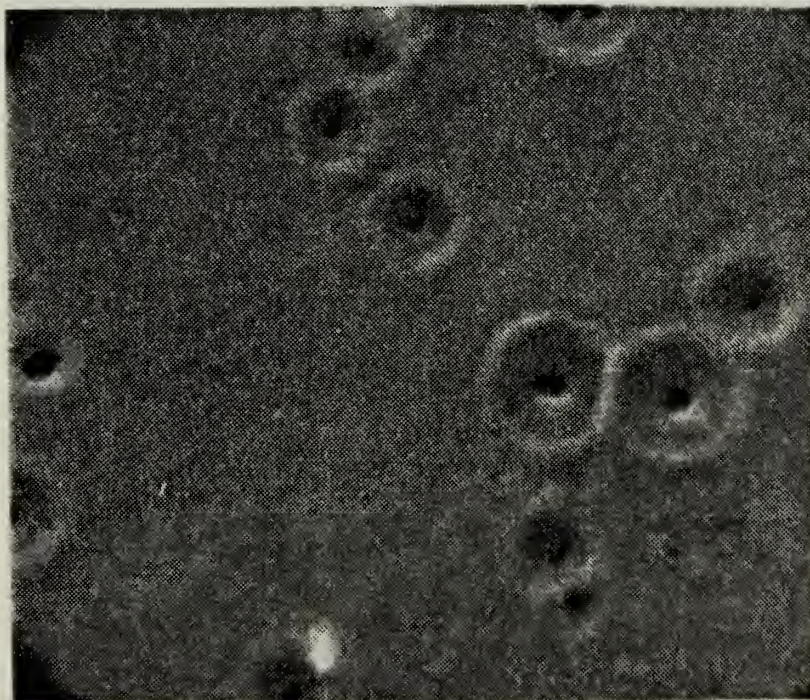


Figure 26. 304 Stainless. Unipolar arcing at 2.7mm from main laser impact crater (2500X SEM)

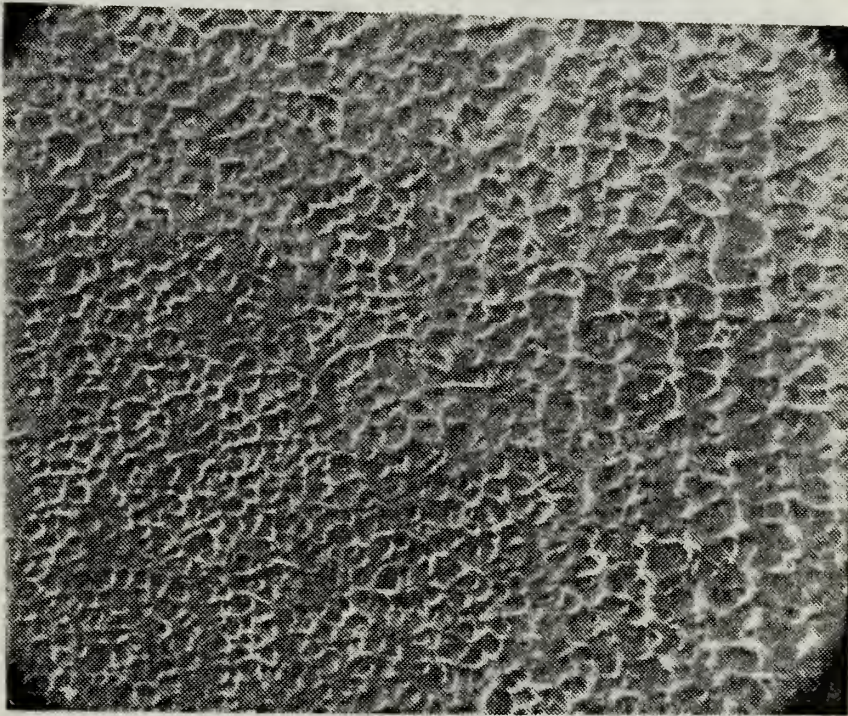


Figure 27. 304 Stainless. Typical molten surface effects and diffraction pattern (130X SEM)

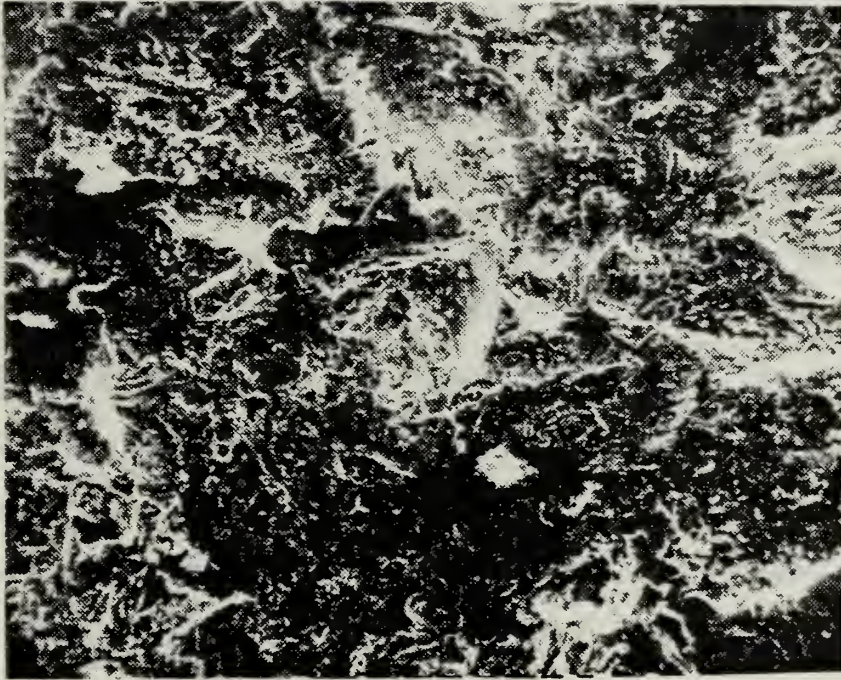


Figure 28. Sandblasted 304. Typical surface structure produced by sandblasting (220X SEM)

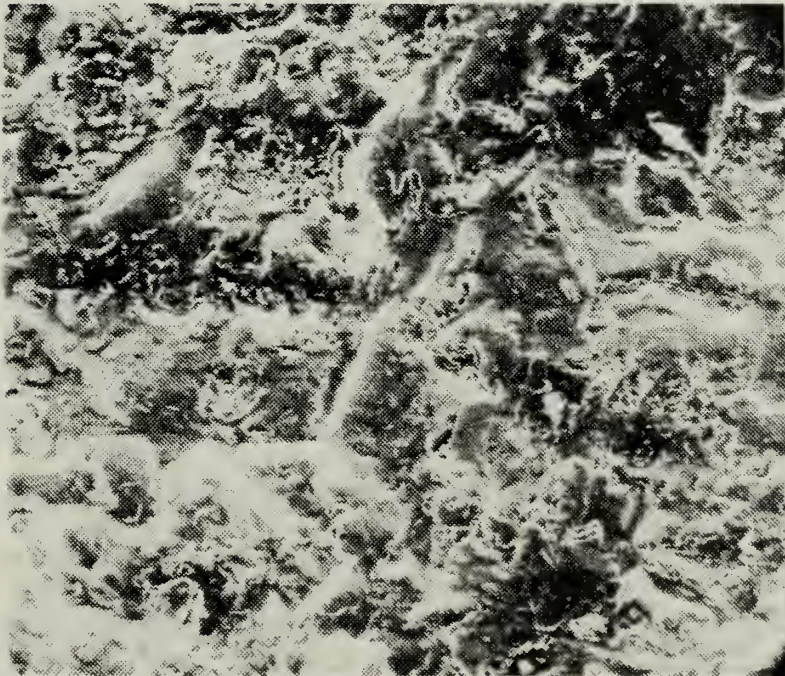


Figure 29. Sandblasted 304. View (center) of molten surface effects after irradiation (110X SEM)

energies 9.38 and 10.68 Joules at the same focal spot. This two shot sequence was done to facilitate finding the main laser crater amid the extremely rough surface. Figures 29 and 30 show the central area of the main crater, while figures 31 and 32 show typical molten surface effects approximately 1.0mm from the main crater center. As can be seen, it is extremely difficult to find evidence of unipolar arcing amid the rough surface and clutter. It is apparent that the unipolar arc density is lower in the sandblasted target however. Unipolar arcing was noticed at a density of approximately 500 arcs/cm^2 at a distance of approximately 1.5mm from crater center; however, beyond this distance almost no unipolar arcs could be found. It is felt that the arcs seen were formed predominately on the second shot after the sandblasted surface had undergone melting. It is thought that the sandblasting leaves a few atoms thick coating, along with a large number of embedded grains, of SiO_2 on the steel surface which, in turn, acts as inhibitor to arc initiation, even though there are a large number of jagged surfaces produced by the sandblasting that act as electric field enhancers. Figure 33 shows an area (45° from normal) at the edge of plasma-surface interaction effects, while figure 34 shows a corresponding x-ray spectral analysis of the area. A silicon line is shown, though this cannot be attributed to SiO_2 since 304 stainless has a maximum Si content of 1% by weight. Figure 35 shows an area (45° from normal) immediately beyond the plasma interaction area. Corresponding to figure 35 is figure 36 which shows scintillations produced by x-rays from silicon in that target area.

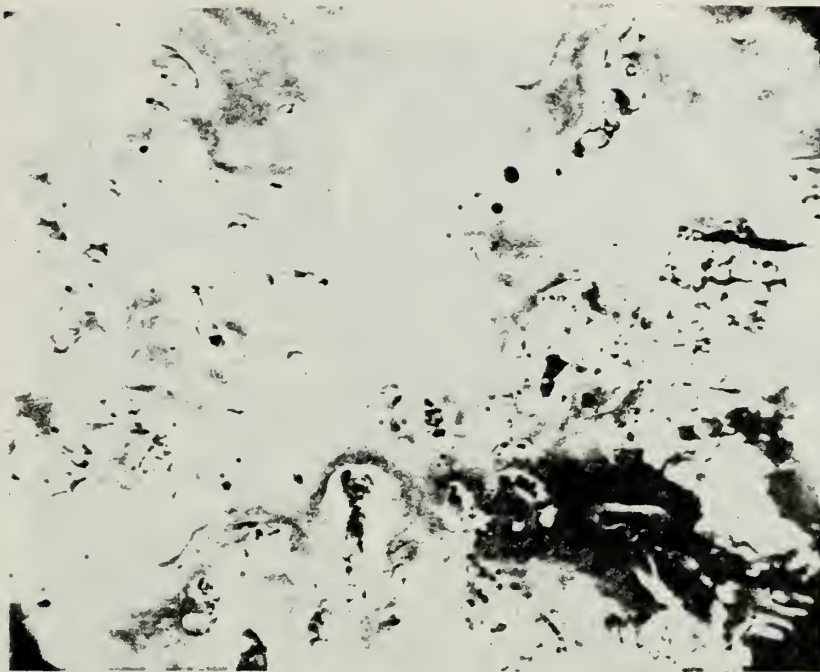


Figure 30. Sandblasted 304. Close up view of molten surface effects (520X SEM)

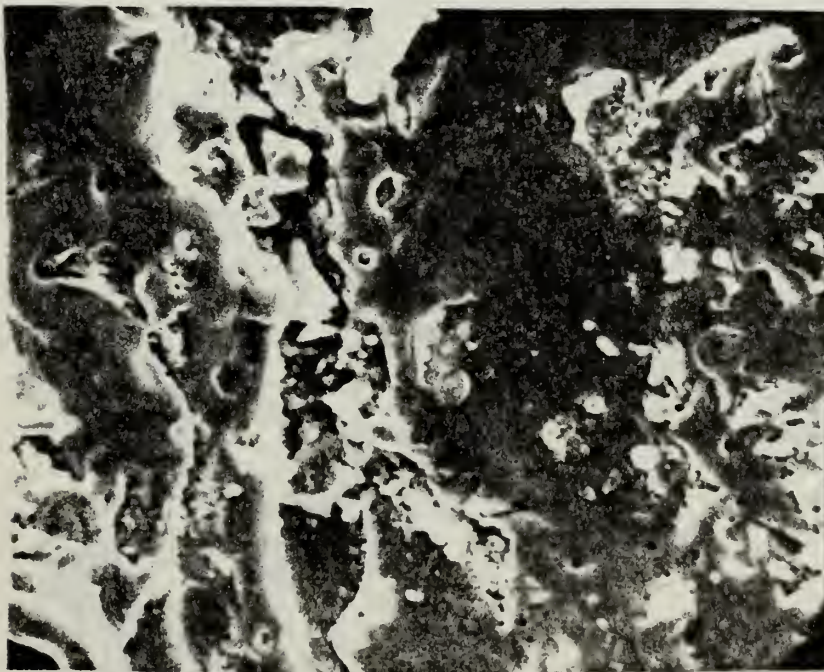


Figure 31. Sandblasted 304. Molten surface effects seen at 1.0mm from main crater center (1050X SEM)

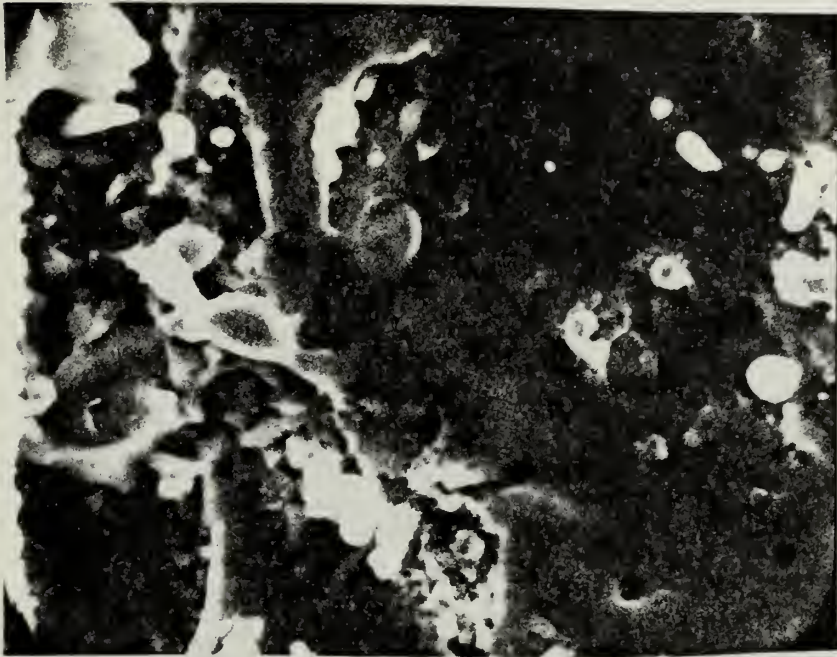


Figure 32. Sandblasted 304. Area of previous figure seen at higher magnification (2100X SEM)

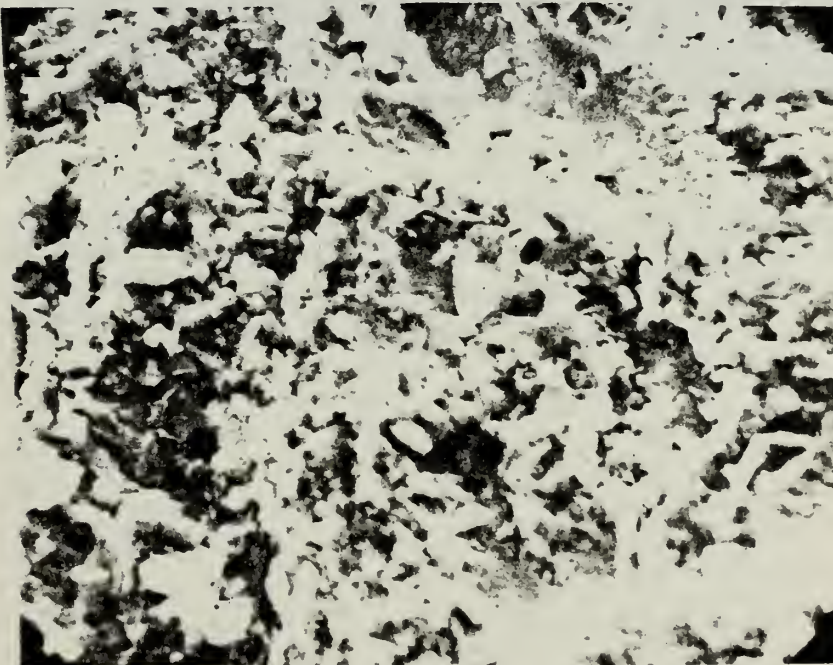


Figure 33. Sandblasted 304. Area seen near cessation of molten surface effects. Note unipolar arc in upper right hand corner (2200X SEM)

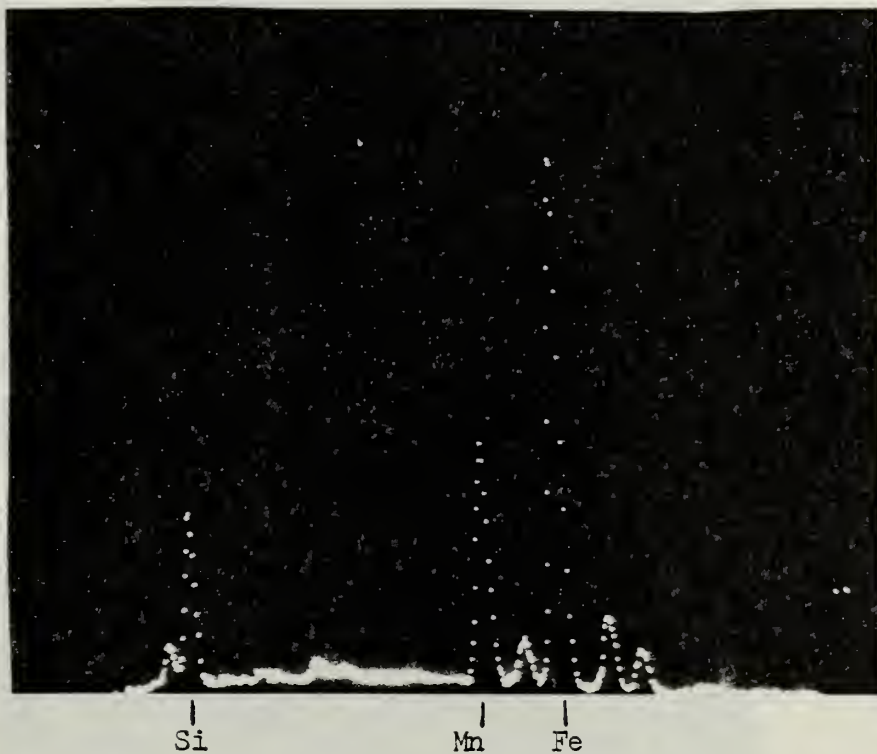


Figure 34. Sandblasted 304. X-ray spectrum produced by area in previous figure. Lines (left to right) are: aluminum, silicon, manganese, chromium, iron, iron, and nickel.

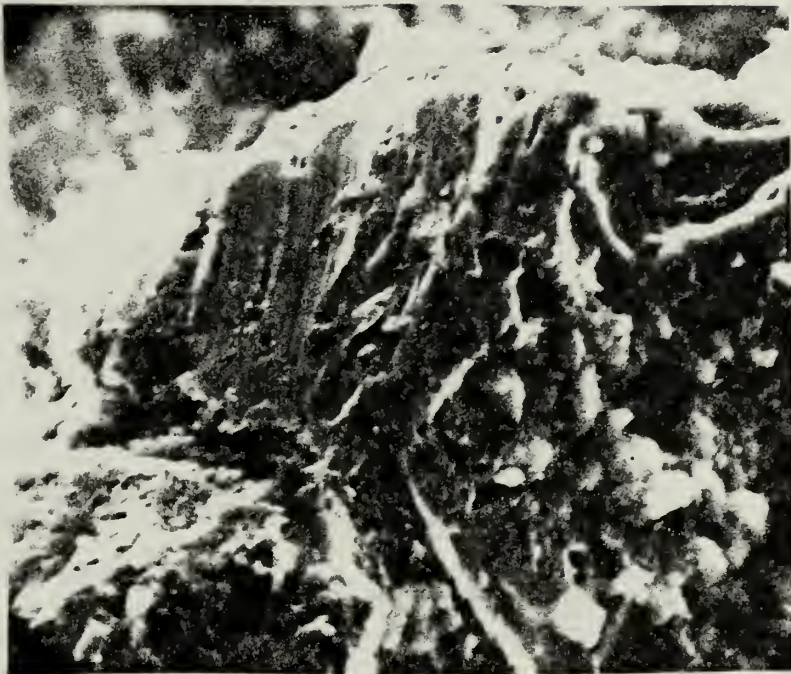


Figure 35. Sandblasted 304. Surface seen at cessation of surface effects (2200X SEM)

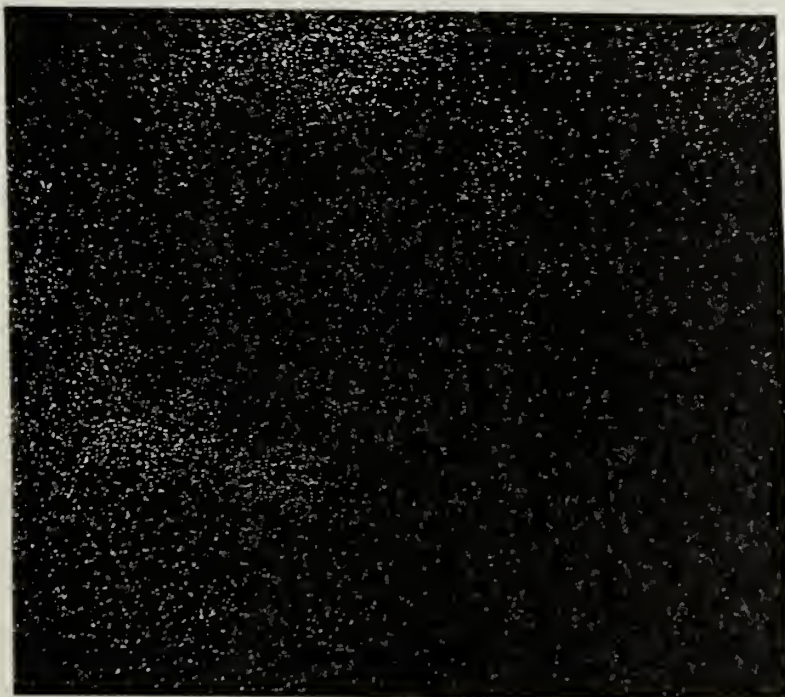


Figure 36. Sandblasted 304. Scintillations from x-rays from silicon. Each spot of light corresponds to x-ray radiation received from area in previous figure

4. HY 130

HY 130 is a 5 Ni-Cr-Mo-V steel containing less than 0.12 percent carbon and has a minimum yield strength of 130,000 psi, and a high degree of toughness. The microstructure is predominately tempered martensite, with the steel being developed for use in the United States Navy submarine hull construction. Target material was obtained from a thesis student of Professor Challenger and was cut from a cast block with a hardness of Rockwell C 32, and a composition as listed in Appendix A. To the knowledge of the author, this is the first time that a tough, high strength, martensitic steel has been tested for susceptibility to unipolar arcing.

One polished target was irradiated in the target chamber at a pressure of 10^{-6} Torr, a focal spot diameter of 0.35mm, and a laser pulse energy of 12.14 Joules. The main laser crater shown in figure 37 measured 0.56mm in diameter and had a depth of 15 microns. Three unipolar arcs can be seen immediately outside the crater amidst a surface where sputtering had apparently revealed the martensitic microstructure. The two larger unipolar arc craters shown in figure 37 measure 0.095mm in diameter and 12 microns in depth. Plasma surface effects were noted over an area of approximately 5mm^2 , only one quarter that of stainless steel at the same pulse energy and focal spot size. Figure 38 shows an area where the left side of the figure is 0.5mm from the edge of the main crater rim. The area shown covers 0.64cm^2 and shows 27 arcs upon careful search, which corresponds to an arc density of 42 unipolar arcs/ cm^2 . The largest arc craters shown in this figure have a diameter of 0.067mm and a cathode spot of 0.010mm diameter. Figure 39 shows an area

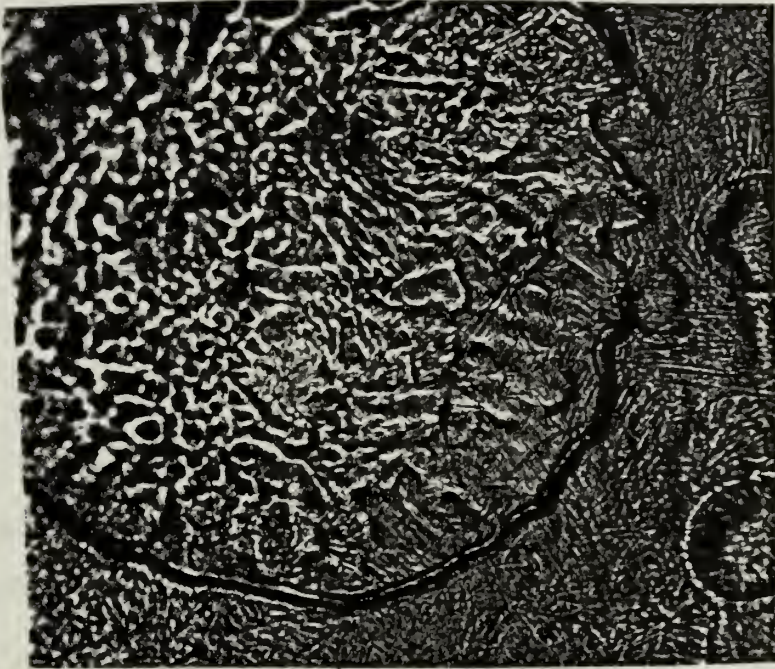


Figure 37. HY 130. Main laser impact crater resulting from a 12.14 Joule focused pulse (160X optical)

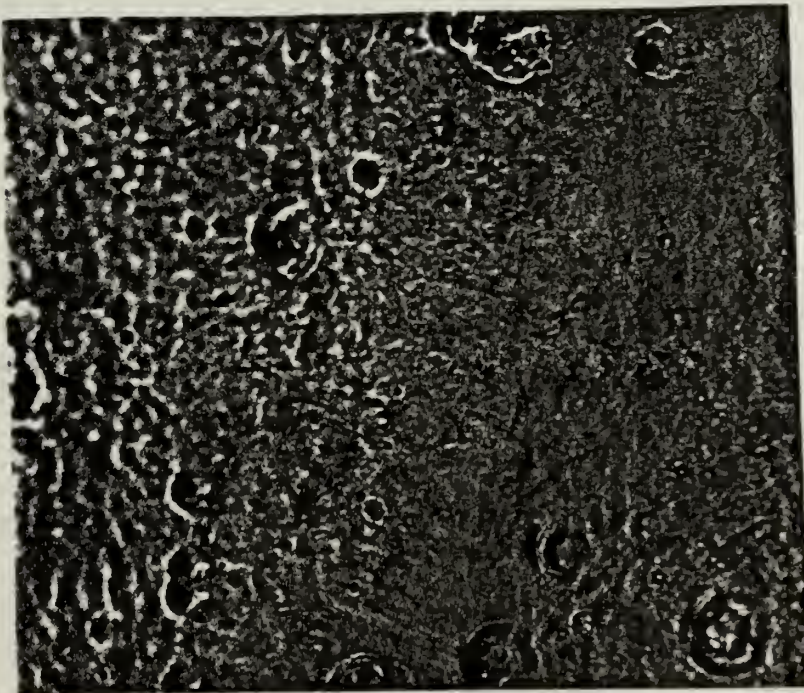


Figure 38. HY 130. Unipolar arcing where left side of figure is 0.5mm from main laser impact crater (160X optical)

at the opposite side of the main laser crater from figure 38, where the top edge of the figure lies 0.75mm from the main laser crater rim. The area shown covers 0.51cm^2 and has 20 unipolar arcs or 39 arcs/cm^2 . Some plasma erosion of the surface is apparent showing the microstructure of the steel, though the erosion is not as severe as that near the main laser crater. The largest unipolar arcs in this figure measure 0.076mm in diameter and have a cathode spot size of 0.013mm diameter.

Figure 41 is a photograph of the polished surface of cast HY 130 showing a porous surface typical of cast steels. It is felt that the large cathode spots seen were initially pores in the surface that served as initiators to unipolar arcing and that the large diameter of the spots was at least partly attributable to the pore size. It appears that the number and distribution of the large arcs corresponds to the number and distribution of the surface pores.

The material removed from these super sized arcs may be as much as 100 times the amount removed in a typical stainless steel unipolar arc. It is important to note, however, that stainless steel arc densities can easily approach or exceed $100,000\text{ arcs/cm}^2$ at a distance of 0.75mm from the main laser crater with 12 Joules on target, as compared with the observed $39\text{ unipolar arcs/cm}^2$ at 0.75mm in HY 130, with six of these being "super" arcs. Figure 40 shows the largest unipolar arc found on the HY 130 target, an arc which measures 0.140mm rim to rim, has a cathode spot of 0.023mm diameter, and was found at a distance of 0.30mm from the main laser crater outer rim. Even taking these "super" arcs into account, assuming they contribute approximately 100 times the material to the plasma than an average stainless steel

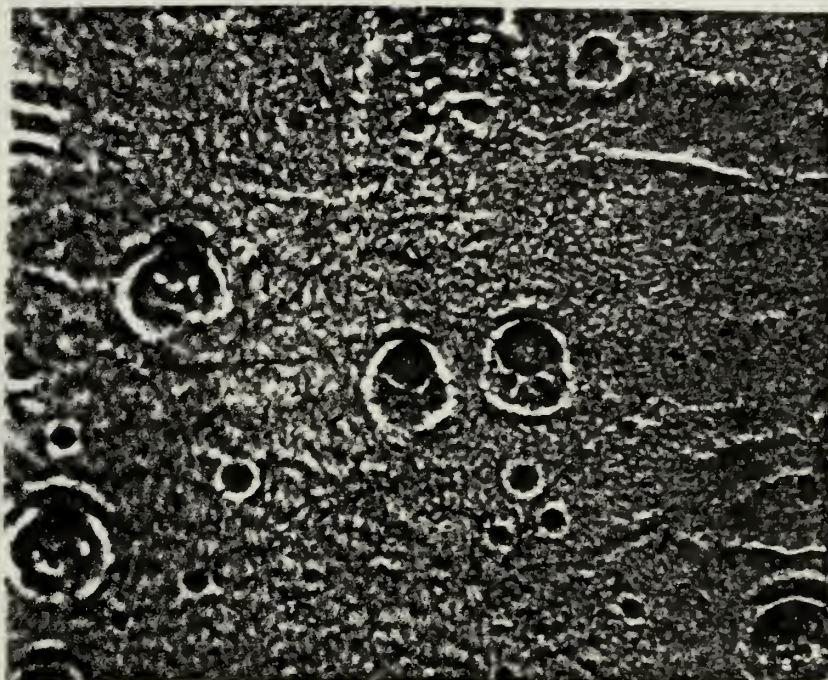


Figure 39. HY 130. Top of figure is 0.75mm from main laser crater. Note extremely large arc craters (160X optical)

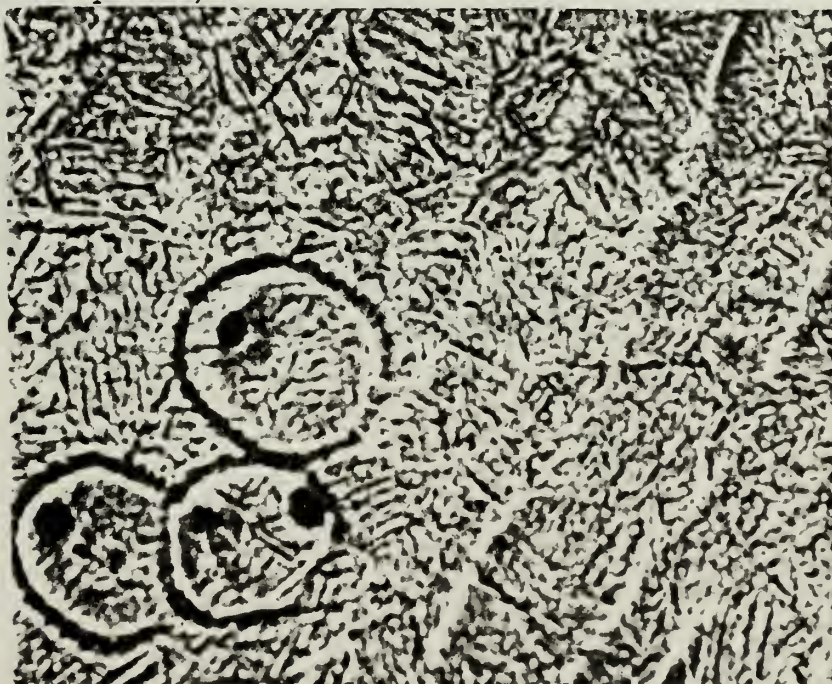


Figure 40. HY 130. Largest unipolar arc (found at top) measures 0.140mm diameter with a cathode spot of 0.023mm (200X optical)

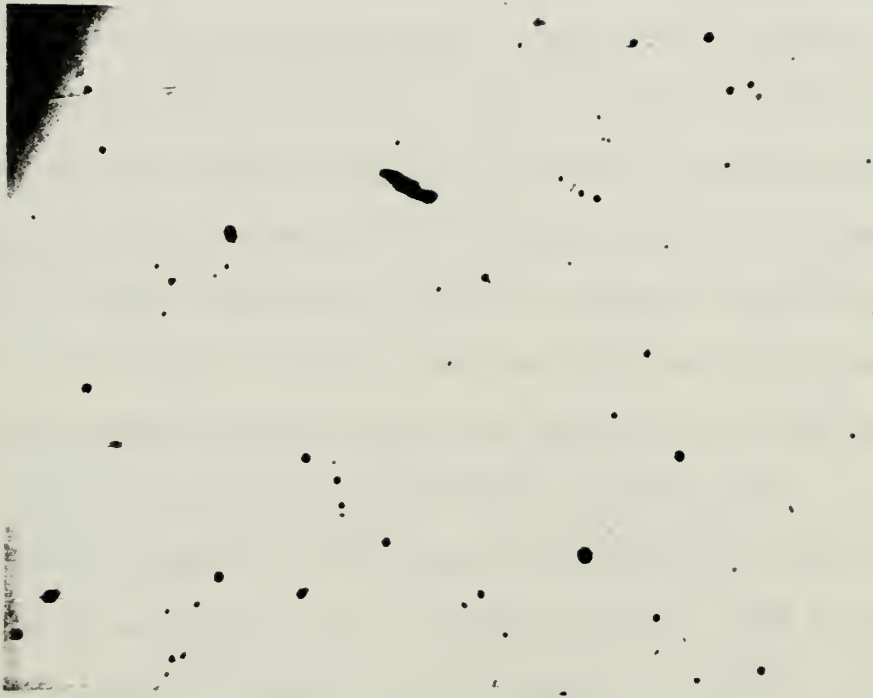


Figure 41. HY 130. Polished surface showing porosity
of the cast material (100X optical)

unipolar arc, the material contributed to the plasma via unipolar arcing from HY 130 was at least three orders of magnitude less than that of type 304 stainless, a substantial decrease and one deserving a more thorough investigation.

5. Copper (Sandblasted)

One copper target was sandblasted using the same procedure as that that was used with the 304 stainless. Again, grit size used was 300, with operating pressure of 85 psi. After sandblasting, the target was irradiated with two laser pulses of 9.53 and 10.55 Joules in the same focal area on target. Again, this was done to aid in locating, with the SEM, the laser damaged area amid the extremely rough surface. Figure 42 is a photograph of an area near the main laser crater center. The total area of molten surface effects was approximately 12mm^2 but no measurements of crater depth and diameter were possible due to the roughened surface. Figures 43 and 44 show, at successively higher magnifications, an area near the center of laser effects. These figures show extensive melting of the surface and a number of unipolar arcs; however, even at the center of the plasma effects, there were areas that showed no interaction effects. Figure 45 shows an area approximately 1mm from the center of plasma effects. Again, extensive melting of the surface could be seen, however, no unipolar arcs could be seen.

The effects noted above were in keeping with the theory that an SiO_2 coating on a conductor will inhibit unipolar arcing. Comparing these results with those of Barker and Rush's [Ref. 17], who irradiated polished copper, the amount of plasma surface interaction was much less on the sandblasted surface. Barker and Rush found that, for a 3 Joule

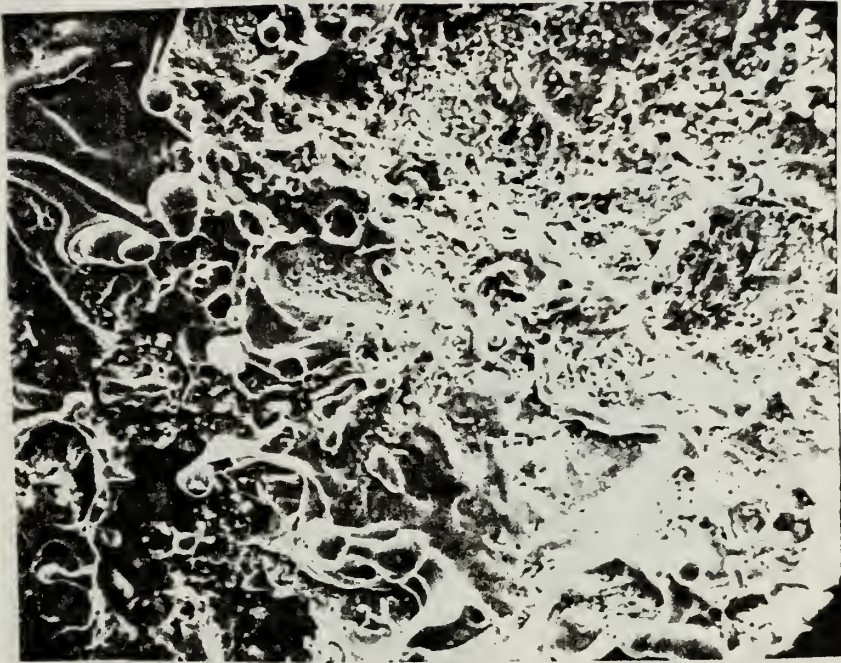


Figure 42. Sandblasted copper. View of main laser impact crater (580X SEM)

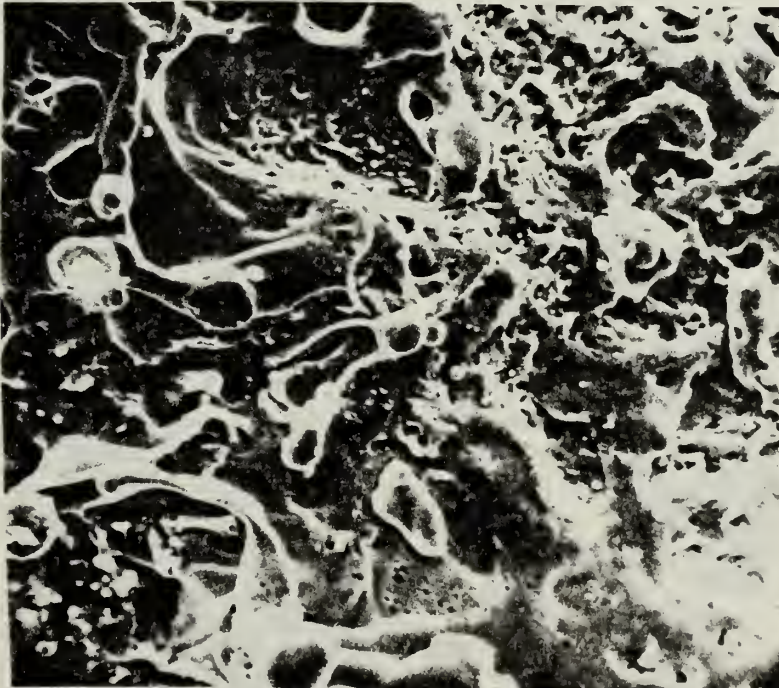


Figure 43. Sandblasted copper. Increased magnification view of main crater (1200X SEM)

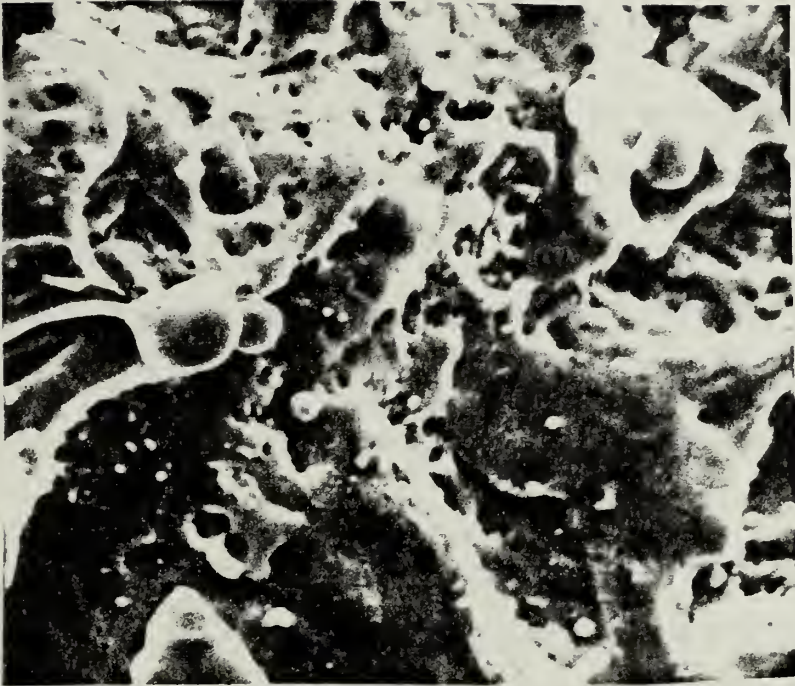


Figure 44. Sandblasted copper. Unipolar arc seen at right, found in main laser crater (2300X SEM)

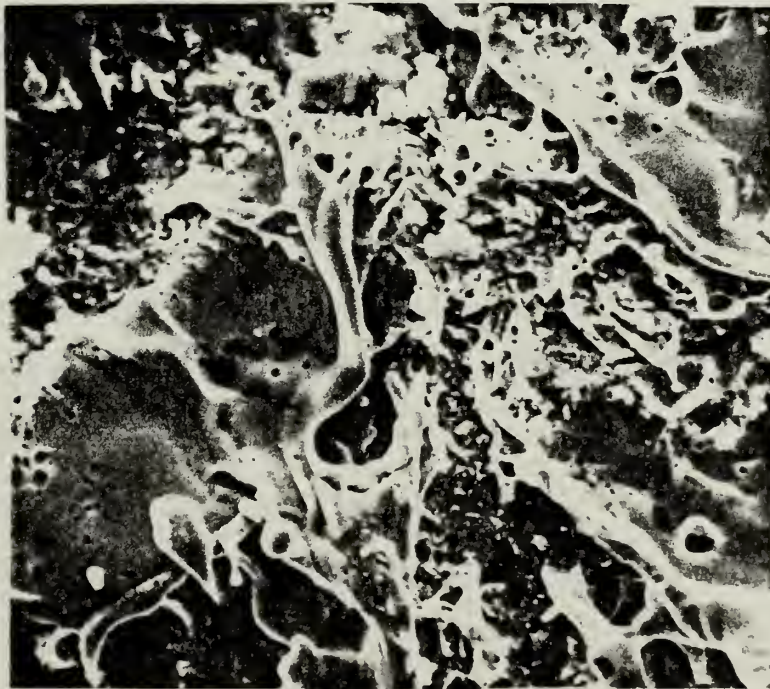


Figure 45. Sandblasted copper. View of area at cessation of molten surface effects (1200X SEM)

focused pulse, the total damaged area was 3.14mm^2 , while 20 Joules on a sandblasted surface damaged 12mm^2 and produced few unipolar arcs. Figure 46 shows the irregular surface produced by sandblasting, while figure 47 shows the silica concentration at the surface seen in figure 45.

6. Type 316 Stainless Steel

A single polished target of 316 stainless steel was irradiated with a pulse energy of 12 Joules and a focal spot diameter of 0.3mm. The elliptically shaped laser crater produced by this pulse is shown in figure 48. The dimensions of the main crater were 0.4mm minor axis, and 0.7mm major axis. Depth of the crater varied but averaged about 20 μm . The total area of molten surface effects was approximately 12mm^2 , about 3mm^2 less than the average 304 stainless molten area.

Figure 49 shows an area, located near the main laser crater rim, and is a typical example of the plasma produced molten surface effects. Some unipolar arcs that were formed very early after plasma production and then "washed out" by ensuing molten surface effects can be seen. Figures 50 and 51 show the arc densities obtained at radii of 2 and 2.7 mm respectively from the main laser crater center, with a unipolar arc density of $600/\text{cm}^2$ for figure 50 and $350/\text{cm}^2$ for figure 51. Of note are the numerous craters, varying in diameter from 2 to 4 microns that appear to have formed very early after plasma initiation and had their crater and cathode spot eroded over by latter plasma effects, suggesting that arc initiation was easy for some reason, but that arc cessation was rapidly obtained.

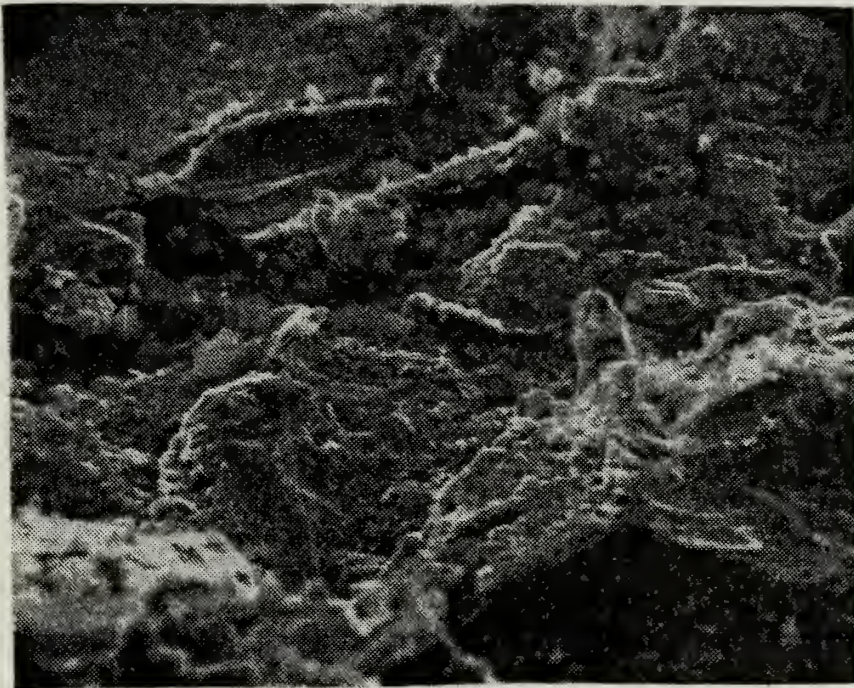


Figure 46. Sandblasted copper. Surface view seen at 45 degrees from normal (1200X SEM)

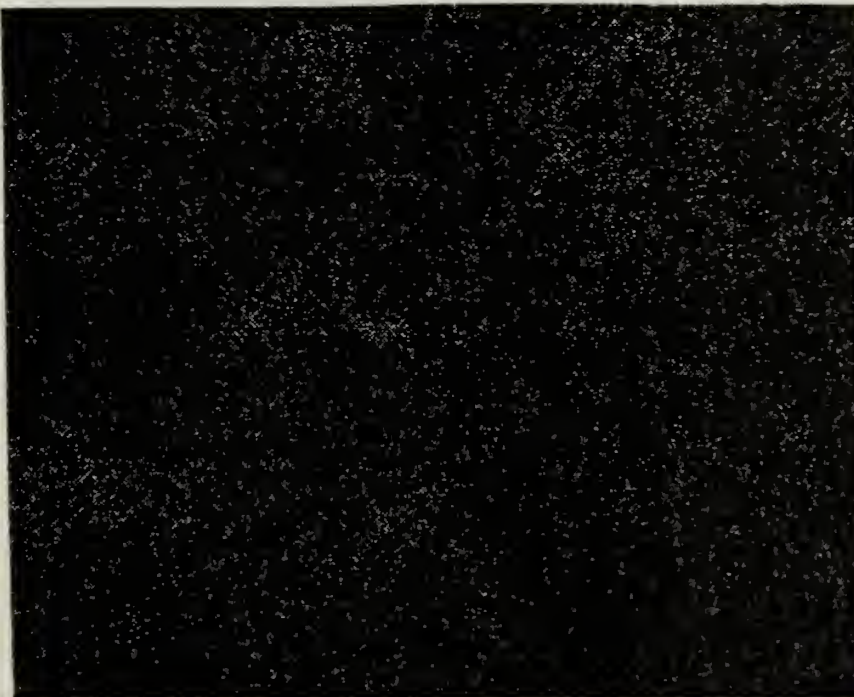


Figure 47. Copper. Scintillation pattern produced by x-rays from silica coating on copper surface seen in previous figure (1200X SEM)

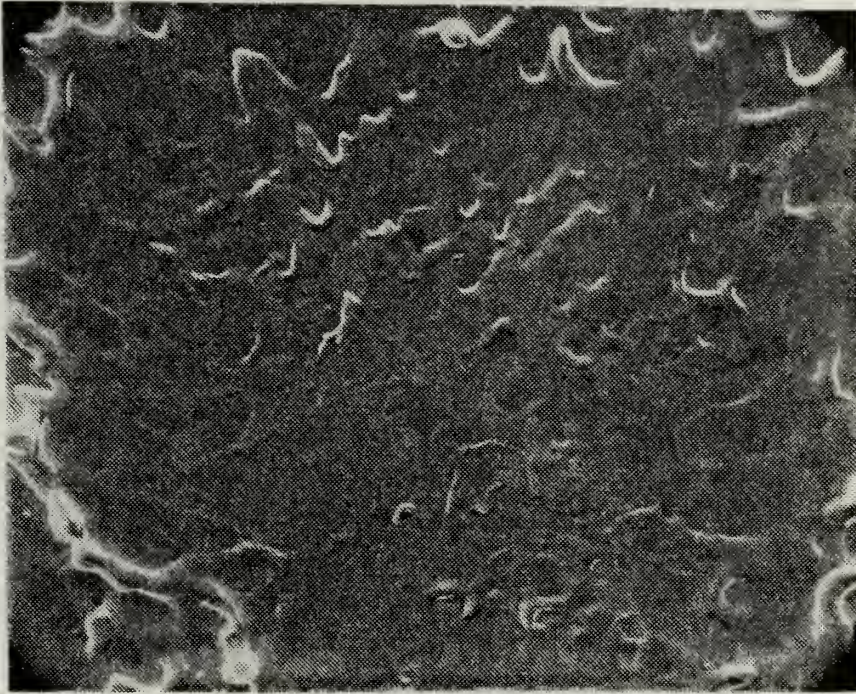


Figure 48. 316 Stainless. Main laser impact crater (240X SEM)

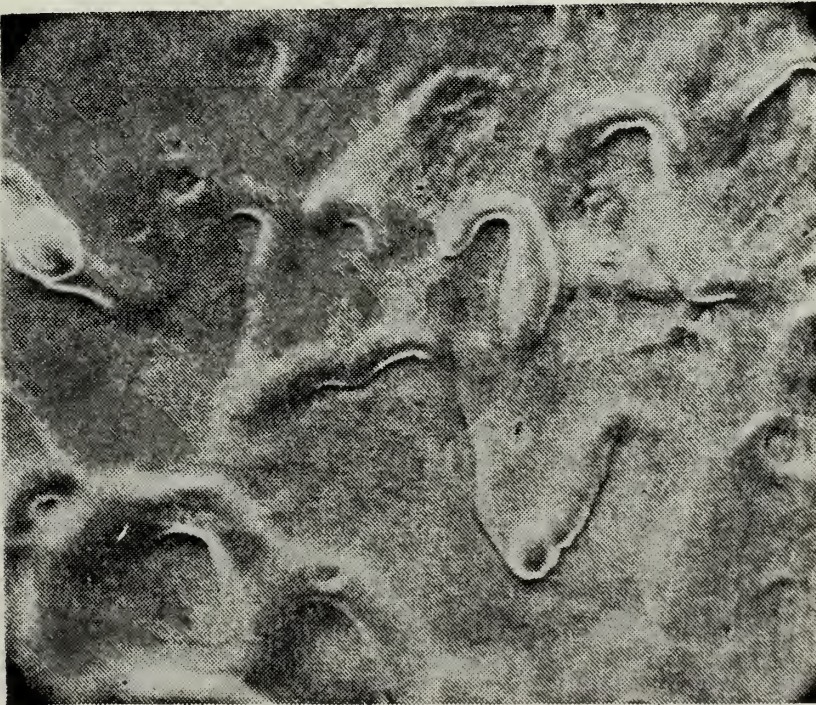


Figure 49. 316 Stainless. Typical molten surface effects produced by laser irradiation (650X SEM)



Figure 50. 316 Stainless. Unipolar arcing found at 2.0mm from main laser impact crater (650X SEM)

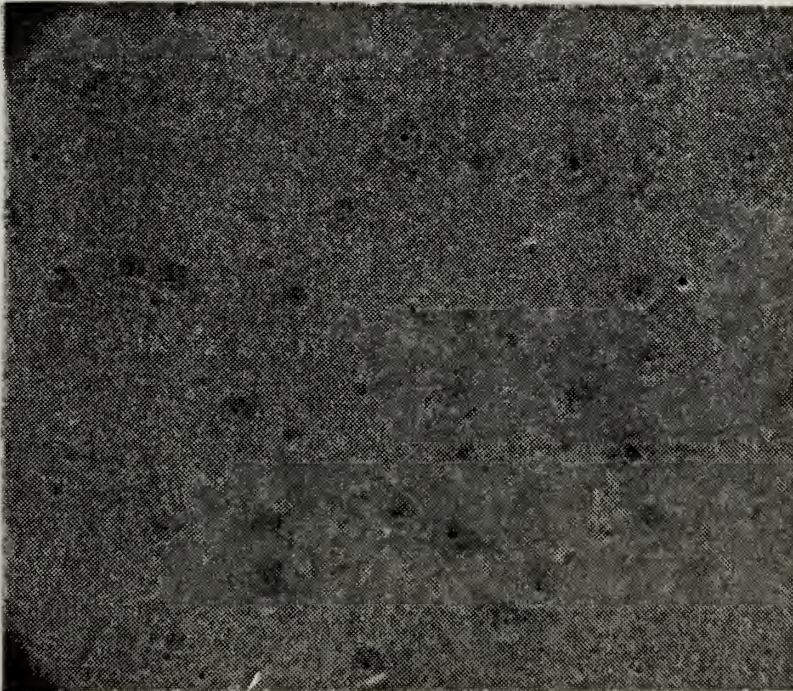


Figure 51. 316 Stainless. Unipolar arcing found 2.7mm from main laser crater (620X SEM)

7. 1030 Steel

One polished target of 1030 steel, with a hardness of 42 on the Rockwell B scale, was irradiated by a laser pulse with an energy of 11.6 Joules and a focal spot diameter of 0.3mm. A main laser crater, seen in figure 52, with diameter of 1.2mm and a depth of 25 microns, was produced which covered a considerably larger area than the stainless or HY 130 crater areas. Molten surface effects were seen over an area of approximately 15mm^2 ; however, with a cessation of unipolar arcing about 3mm from main laser crater center. Those numbers correspond almost exactly to those of 304 stainless. Figure 53 shows an area that was approximately 2mm distant from the main laser crater with 48 unipolar arcs appearing in the 7.8mm^2 area; which corresponds to an arc density of $615/\text{cm}^2$, a density closely paralleling that of the stainless steel targets at the same radial distance.

B. METALLIC GLASSES

For this part of the experiment a commercially prepared metallic glass alloy $\text{Fe}_{80}\text{B}_{20}$ was irradiated at energies ranging from 1.2 to 15 Joules, with focal spot diameters varying from 0.4 to 5mm. Also, attempts were made to produce metallic glass-like surfaces on HY 130 steel, 1030 mild commercial steel, and on type 304 and type 316 stainless steel, and then irradiate these glass surfaces to determine their susceptibility to unipolar arcing.

Two different approaches were taken in an attempt to produce metallic glass surfaces on 304 stainless, 316 stainless, 1030, and HY 130 steels. The first approach was to discover the energy density required for onset of plasma production in the metal, and then irradiate the surface

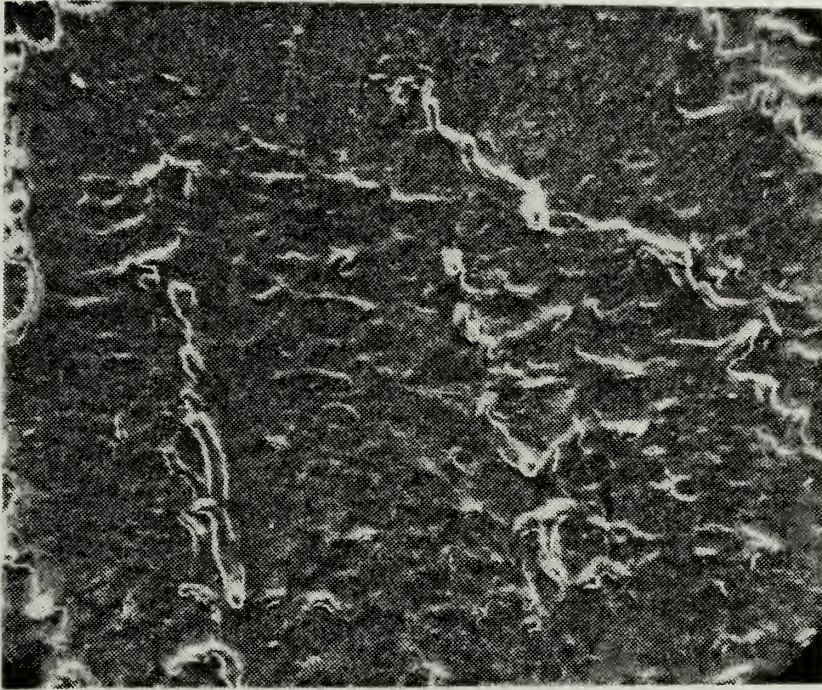


Figure 52. 1030 Steel. Main laser impact crater (125X SEM)

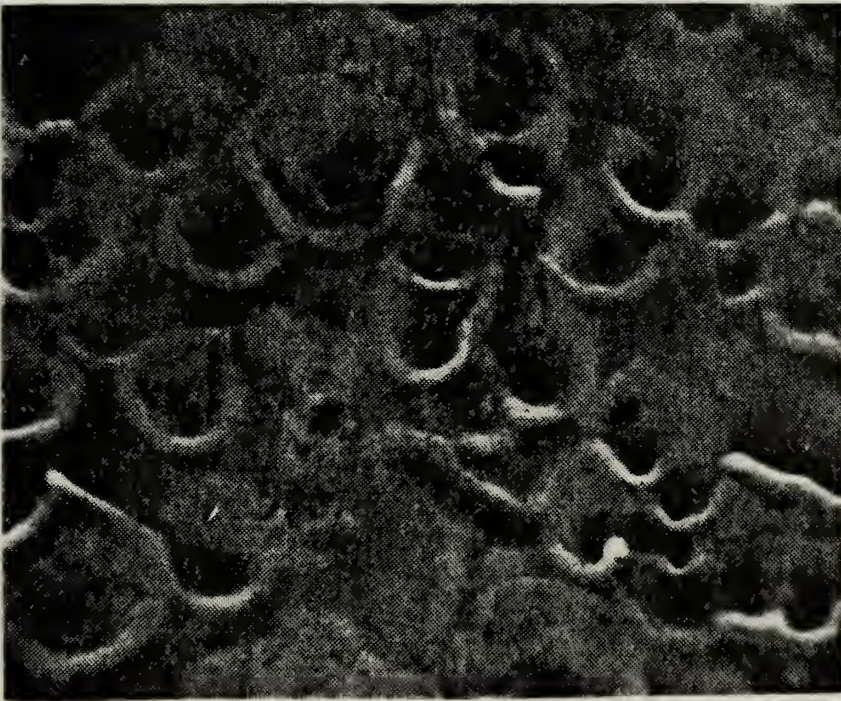


Figure 53. 1030 Steel. Unipolar arcs found at 2.0mm distance from main laser crater (1250X SEM)

at energy densities just below this value. Ryan and Shedd [Ref. 4] reported that in type 304 stainless steel they were able to produce areas of surface melting without plasma production, and that these surfaces resembled a metallic glass in that they were more resistant to etching than the surrounding metal surface. This approach was taken only with type 304 stainless as it was deemed ineffective for production of areas larger than 0.03mm^2 .

The second approach was one of brute force but one which is believed to be basically sound. Each target was irradiated at energies varying from 8 to 15 Joules with focal spots of approximately 0.5mm diameter, with 3 to 7 shots in close proximity; thus producing large areas of molten surface effects. It was thought that these areas should be similar in structure to metallic glass, or, if not, should be of very fine microstructure and free of any surface contaminants that aid in unipolar arc initiation. In fact, using a theoretical model as was done by Krehl, Schwirzke, and Cooper [Ref. 11], it was found that for stainless steel, the time between surface melting and resolidification and return to room temperature starting at the arrival of the incident pulse was approximately 1 millisecond, which, with a melting temperature of 1595°C , gives a cooling rate well in excess of $1,000,000^{\circ}\text{C}/\text{second}$. The 1 millisecond value should be regarded as an order of magnitude one since assumptions made for the model assume incident uniform radiation, a one dimensional heat flow, all incident energy absorbed and no shielding by a plasma layer at critical density, and that the thermal properties of the steel do not change with temperature, nor that it undergoes a phase change and that the laser pulse is Gaussian.

The equation for the change in temperature is given by:

$$\Delta T(z, t) = \frac{4P_0}{K} \left(\frac{\ln 2}{\pi} \right)^{\frac{1}{2}} \left[\sum_{q=1}^q \exp - \left(\frac{(q\tau - d)^2}{2} \right) \right]$$

$$\{ k[t - (q - 1)\tau] \}^{\frac{1}{2}} \times \sum_{n=0}^{\infty} \left(\text{ierfc} \frac{(2n + 1) d - z}{2[kt - (q - 1)\tau]^{\frac{1}{2}}} \right) +$$

$$\text{ierfc} \frac{(2n + 1) d + z}{2k[t - (q - 1)\tau]^{\frac{1}{2}}} \Big) - [k(t - q\tau)]^{\frac{1}{2}} \times \sum_{n=0}^{\infty}$$

$$\left(\text{ierfc} \frac{(2n + 1) d - z}{2[k(t - q\tau)]^{\frac{1}{2}}} + \text{ierfc} \frac{(2n + 1) d + z}{2[k(t - q\tau)]^{\frac{1}{2}}} \right)]$$

where 2δ and P_0 define a pulse width and amplitude for a rectangular pulse having the same energy as the Gaussian laser pulse, and the Gaussian pulse as a sum of q columns of equal width τ . K is the thermal conductivity, k is the thermal diffusivity, $q = 2\delta/\tau$ is the number of columns, τ (sec), z is the depth (cm) from the far side of the target of thickness d (cm). Values used for 304 stainless were $\tau = 5\text{nsec}$, $q = 5$, $K = 0.5 \text{ w/cm}^{\circ}\text{k}$, $k = 0.1\text{cm}^2/\text{sec}$, and $P_0 = 10^{10} \text{ w/cm}^2$. For a thorough treatment using an aluminum target see Krehl, Schwirzke, and Cooper [Ref. 16]. Also, as was discussed earlier in Chapter II of this thesis, transient surface pressures were about 10^4 psi at the focal spot due to radiation pressure and recoil of vaporized material. These radical temperature and pressure changes, it was felt, should produce a metallic glass surface layer or, at the very least, a hard surface layer with an extremely fine microstructure.

1. Metallic Glass Fe₈₀B₂₀

Four shots were made with a 5mm diameter focal spot and energies on target of 8.1, 8.6, 9.3 and 10.6 Joules. At these energy densities, there were no discernable plasma effects noticed on these samples when compared with an unirradiated sample of the metallic glass alloy. A shot was then made with a focal spot size of 0.4mm and an energy of 11.25 Joules. The laser shot burned through the ribbon, creating a hole of 1.0mm diameter, and a small amount of splattering confined to within a 0.35mm radius of the edge of the hole. There is a significant amount of surface melting within the 0.35mm radius, and a small number of what appeared to be unipolar arc craters formed when the alloy was still molten; however, outside this zone, no evidence of unipolar arcing was found with the surface being examined at magnifications up to 2100X. Figures 54, 55, and 56 show areas, at successively higher magnification, immediately outside the main laser crater. The arc craters in these photographs measure from 6 to 20µm in diameter and are comparatively widely separated.

A sample of the Fe₈₀B₂₀ metallic glass was taken and annealed at 380°C for two hours, as per Walter, et.al., [Ref. 18] to initiate crystallization of the metallic glass. This sample was then irradiated at an energy of 11.75 Joules and a spot size of 0.4mm. The hole created by the laser pulse was again 1.0mm in diameter with splattering out to a radius of 0.5mm from the edge of the crater. Figures 57, 58, and 59 show areas, as before, at successively higher magnification, 0.3 to 1.0mm outside the hole burned through the ribbon. As can be seen, arcing has occurred and at a greater density than the unannealed Fe₈₀B₂₀.

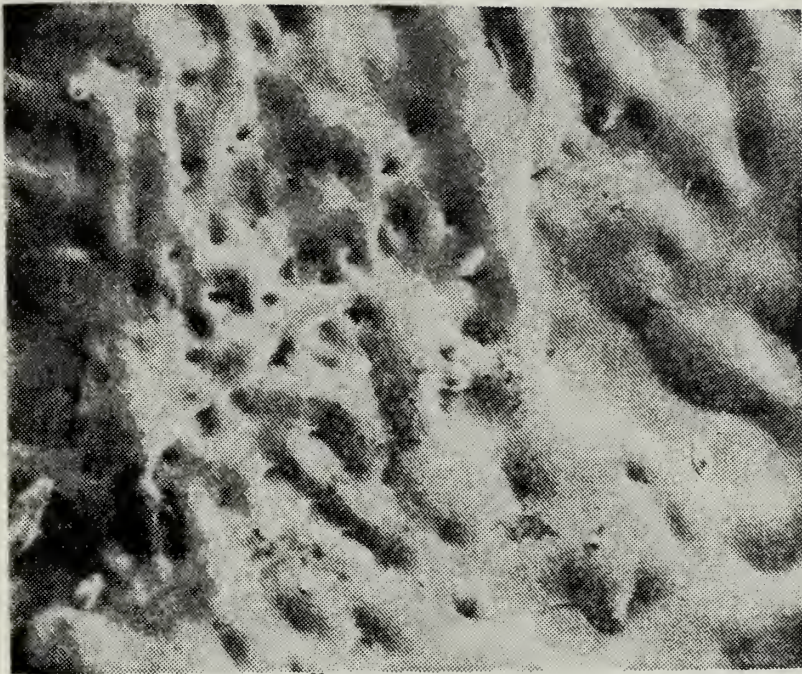


Figure 54. Metallic glass. Typical surface effects seen near laser "burn through" edge (520X SEM)



Figure 55. Metallic glass. Area near the cessation of surface effects (0.35mm) (1000X SEM)

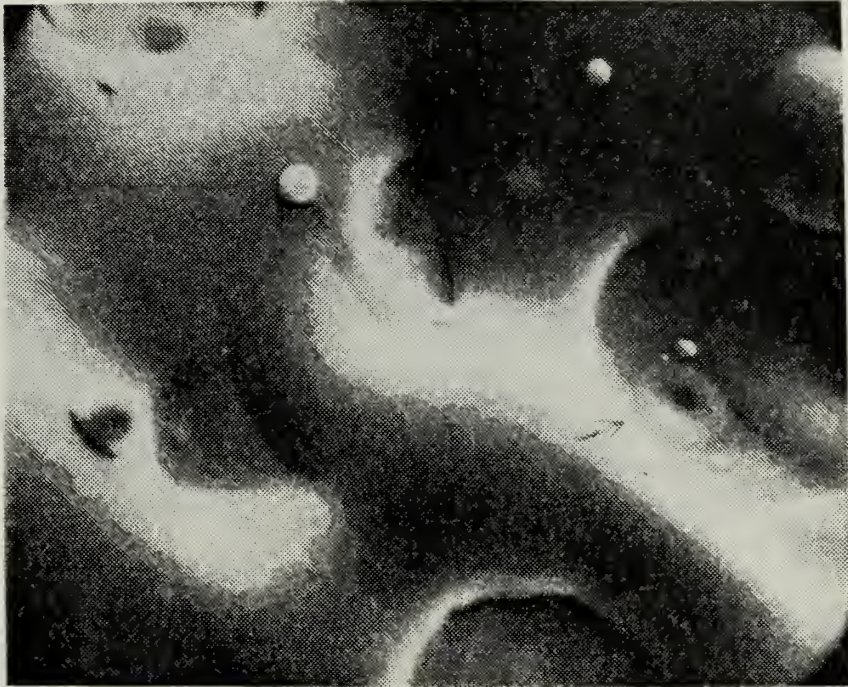


Figure 56. Metallic glass. Close up of unipolar arc and molten surface effects near laser "burn through" edge (2100X SEM)

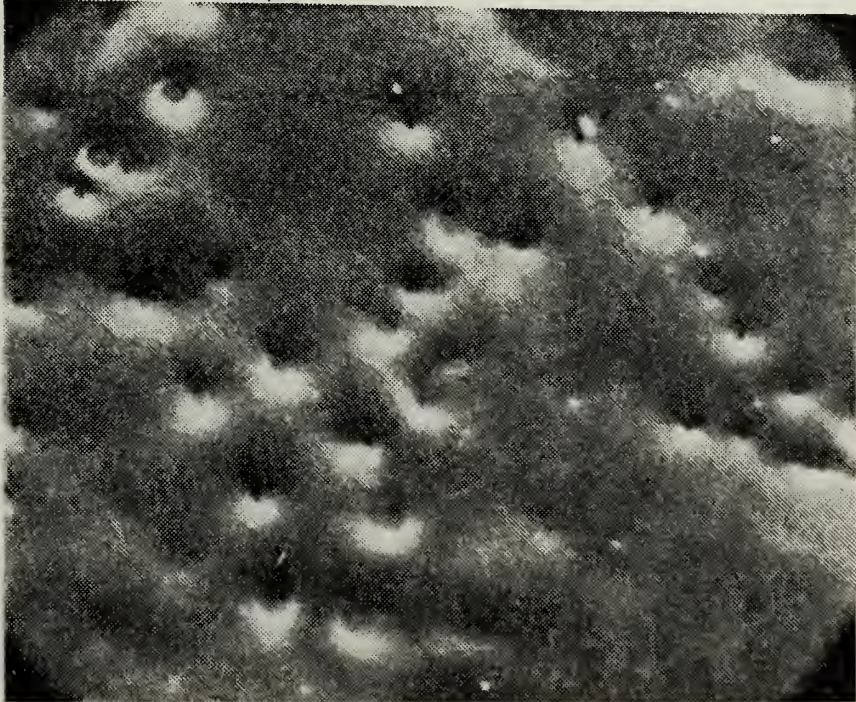


Figure 57. Recrystallized MetGlas. Typical molten surface effects seen near laser "burn through" edge (520X SEM)



Figure 58. Recrystallized MetGlas. View of hole, produced by beam irregularity, and the nearby surface effects (500X SEM)

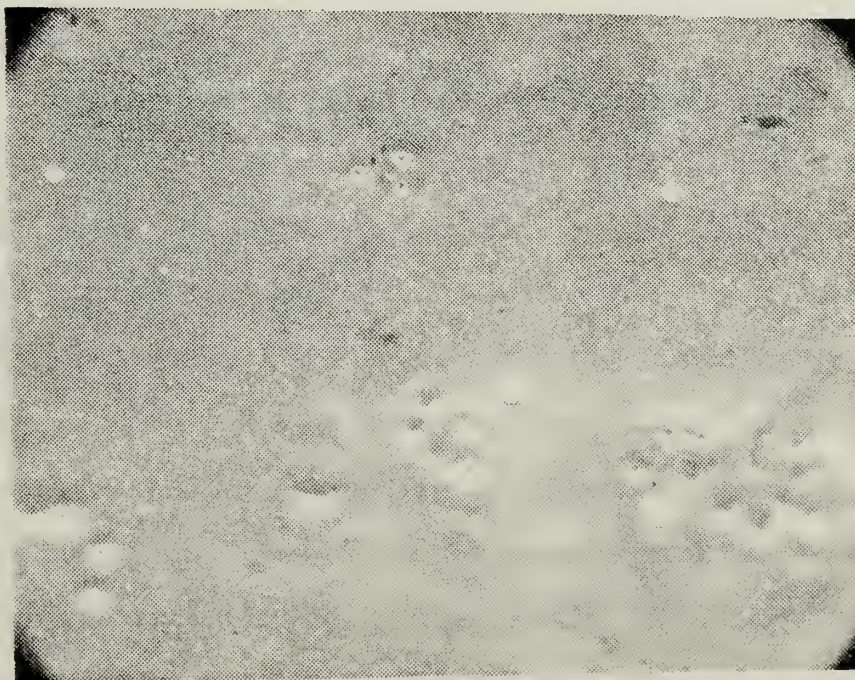


Figure 59. Recrystallized MetGlas. Areas of unipolar arcing found 1.2mm from laser burn through (500X SEM)

According to Walter, et.al., [Ref. 18], the annealing process initiates recrystallization with elliptically shaped crystals of approximately 1 micron in diameter being produced. It is felt that these recrystallized sites provided areas for which unipolar arc initiation is easier than the amorphous areas. Thus, arc densities were higher in the annealed sample than in the unannealed $\text{Fe}_{80}\text{B}_{20}$ metallic glass. Of note is the fact that unipolar arcing appeared in the annealed sample at 1.0mm radius from the main crater, while in the unannealed samples no arcing effects were noted beyond the immediate edge of the main laser crater.

2. Type 304 Stainless Steel

The first attempts to produce metallic glass surface on 304 stainless involved determining the energy density required for the onset of plasma production which initiates unipolar arcing, and then irradiating a target at an energy density sufficient to produce surface melting but without a plasma. To accomplish this, the laser was focused to a 0.5mm diameter spot size and was then fired at targets with the laser pulse filtered for each shot, at successively lower levels of pulse transmittance and, therefore, successively lower energy levels. A photograph was taken of each laser pulse-target interaction continuing at the successively lower energy densities until a plasma could not be seen in the photograph. The camera for photographing the laser-target interactions was a Polaroid CR-9, using an ASA 3200 Polaroid film, with an f-stop setting of 8. Figures 60 and 61 show the cutoff obtained, while figure 62 shows a typical spot shape and burn pattern obtained at these low energy densities. It was found that the energy

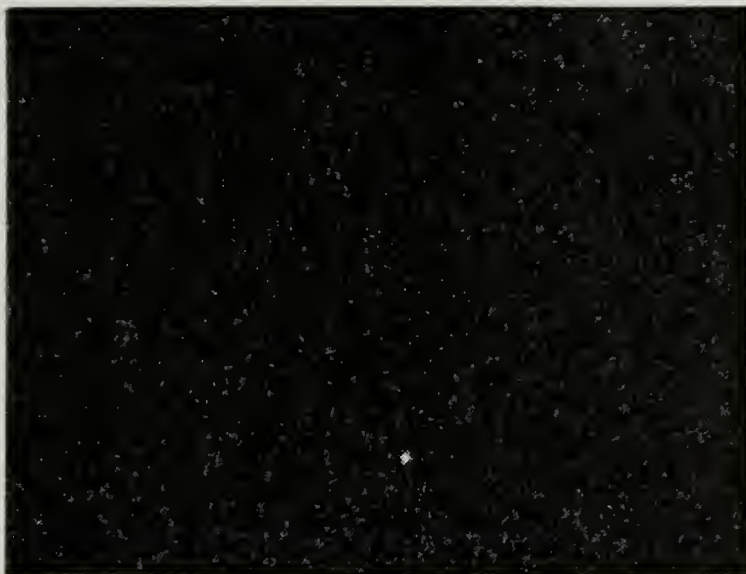


Figure 60. 304 Stainless. Plasma produced at
18 MW/cm² energy density

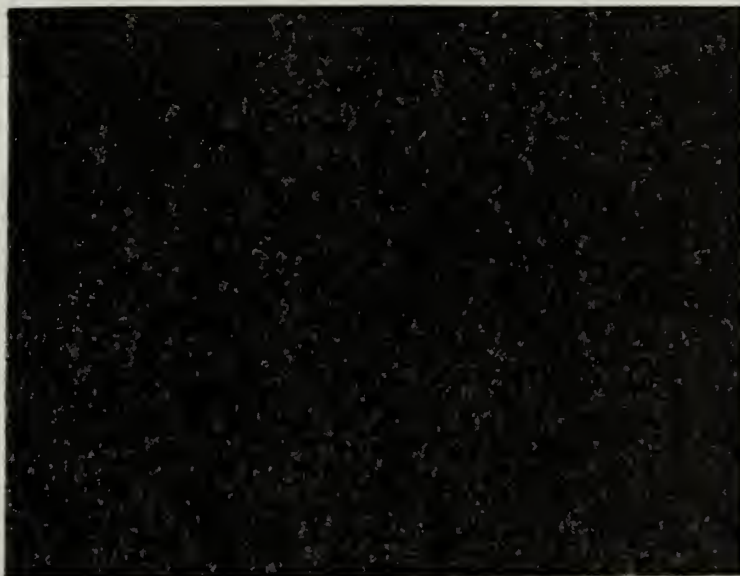


Figure 61. 304 Stainless. No plasma produced at
10 MW/cm² density

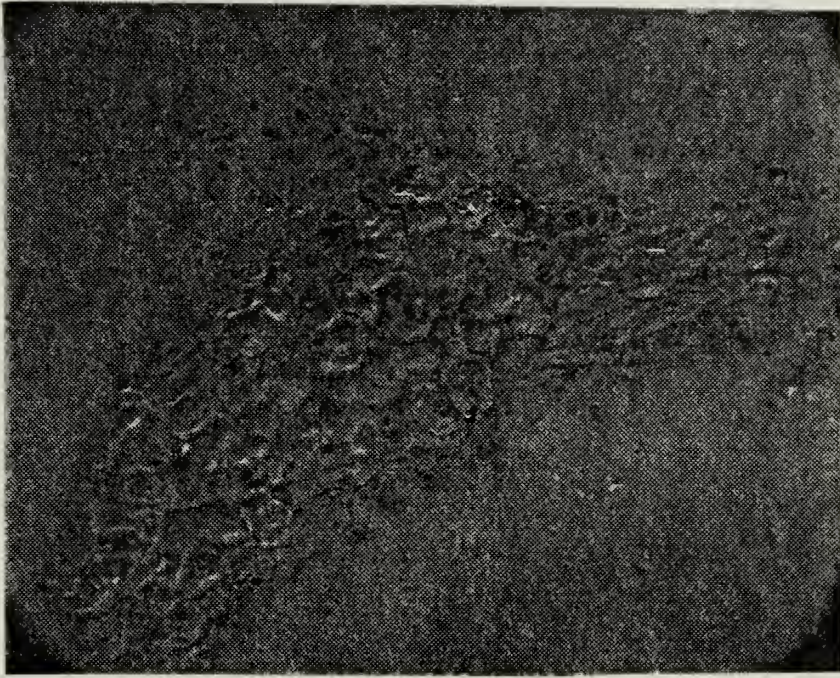


Figure 62. 304 Stainless. Typical burn pattern seen at low energy densities-25 MWatt/cm² (260X SEM)

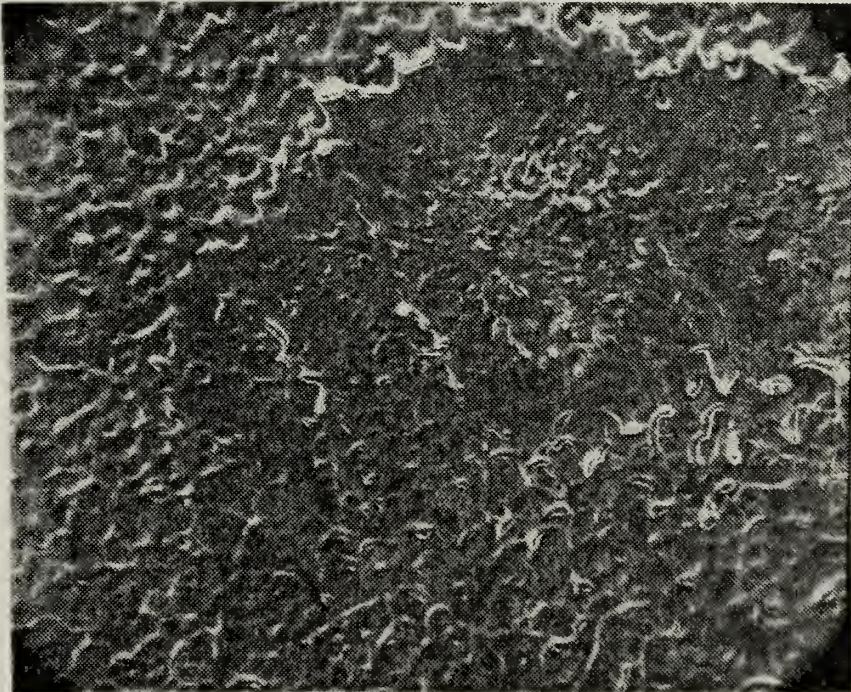


Figure 63. 304 Stainless. Main laser crater produced by pulse number two (130X SEM)

density required for the onset of plasma production lies around 11 Megawatts/cm²; however, the figure obtained is only an approximate one, since the incident radiation was assumed distributed uniformly and hot spots and beam irregularities could not be taken into account.

A 304 stainless target was then irradiated at an energy density of approximately 7 Megawatts/cm², then etched electrolytically and examined. Areas of possible metallic glass production were observed; however, the largest area obtained measured less than 0.1mm in diameter and was deemed to be unusable in any attempts to determine the susceptibility to unipolar arcing of stainless steel metglas. The results from those first attempts brought about the brute force attempt, with the thought that the areas around the main laser crater and also around unipolar arcs, due to their short time in molten state, themselves should be of a metallic glass form. Initially, a three laser shot sequence was done on a polished 304 stainless target. Two shots, of 9 and 10 Joules energy and focal spot diameters of 0.5mm, were made with the rims of the two resulting main laser craters lying within 1.0mm of each other. A third shot, with an energy of 10 Joules and 0.5mm diameter focal spot, was then made with the result that the farthest edge of the previously mentioned rings produced by diffraction of the third laser pulse abutted the main crater rim from the second shot (see appendix B for shot sequence diagrams). Figures 63, 64, and 65 show the main laser crater area of shot number two, after all three shots, at successively higher magnifications. The diffraction rings produced by the third shot would lie immediately outside and to the right in figure 63. The previous three figures should be compared with figures

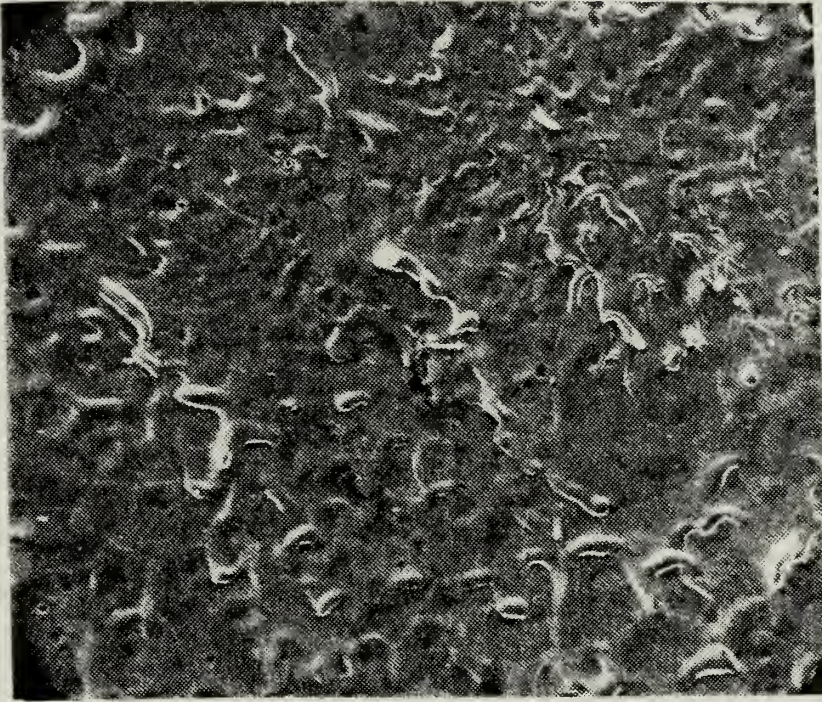


Figure 64. 304 Stainless. Main crater two seen at a higher magnification (260X SEM)



Figure 65. 304 Stainless. Continuation of main crater number two sequence (650X SEM)

66, 67, and 68 which show unipolar arc densities produced by shot number three directly opposite of main laser crater two and at a distance where plasma surface effects should be the same, again at successively higher magnifications. It is obvious that the density of unipolar arcs is much less in the area that had been subjected to rapid surface melting and resolidification and it is interesting to note that, seen at the highest magnifications, it appears that the plasma has had an etching effect on the steel. Figures 69 and 70 show the results of oxalic acid etching the surface produced by laser glazing. The author was unable to interpret these etching results.

A repeat of the linear three shot sequence with a distance of 2.5mm between successive crater centers produced similar results, though unipolar arcing was much more apparent this time in crater number two. Figure 71 shows an area of molten effects produced by shot number two, with the left edge of the figure lying 2.5mm from the center of main laser crater number three. Figure 72 shows an area lying directly opposite crater two, with the midpoint of the figure being 2.5mm from shot number three. Again, though some new unipolar arcs are noticeable in figure 71, their density is much less than that seen in figure 72.

Because of those results, an experiment was undertaken with a polished 304 stainless target being irradiated by a linear seven shot sequence (see Appendix B for shot sequence and positions), with the idea that the sequence would produce an extremely large area of molten surface effects. It was felt that the first five shots should provide a continuous line of molten surface effects and that the last two shots

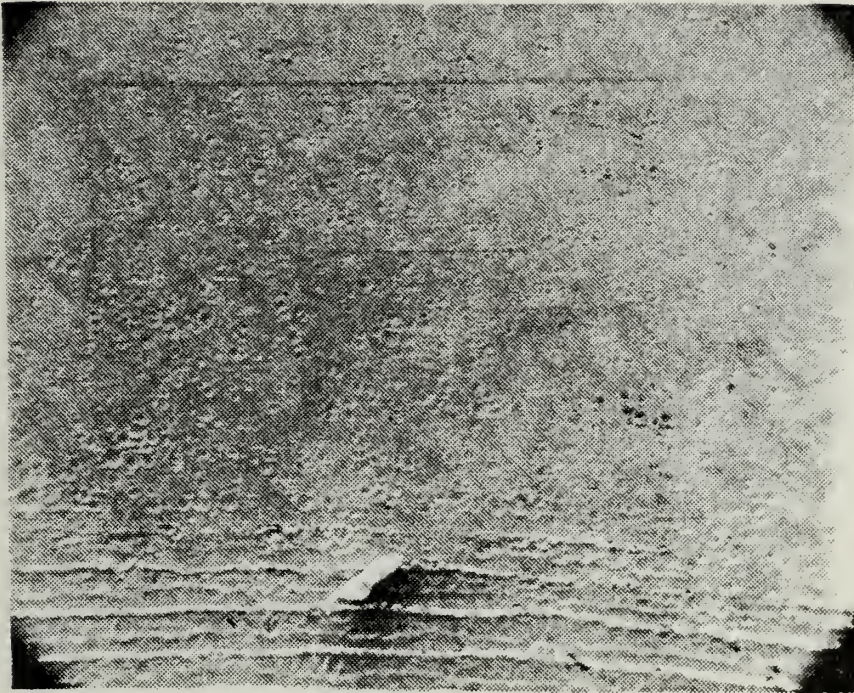


Figure 66. 304 Stainless. Unipolar arcing seen at the cessation of diffraction ring phenomenon (130X SEM)

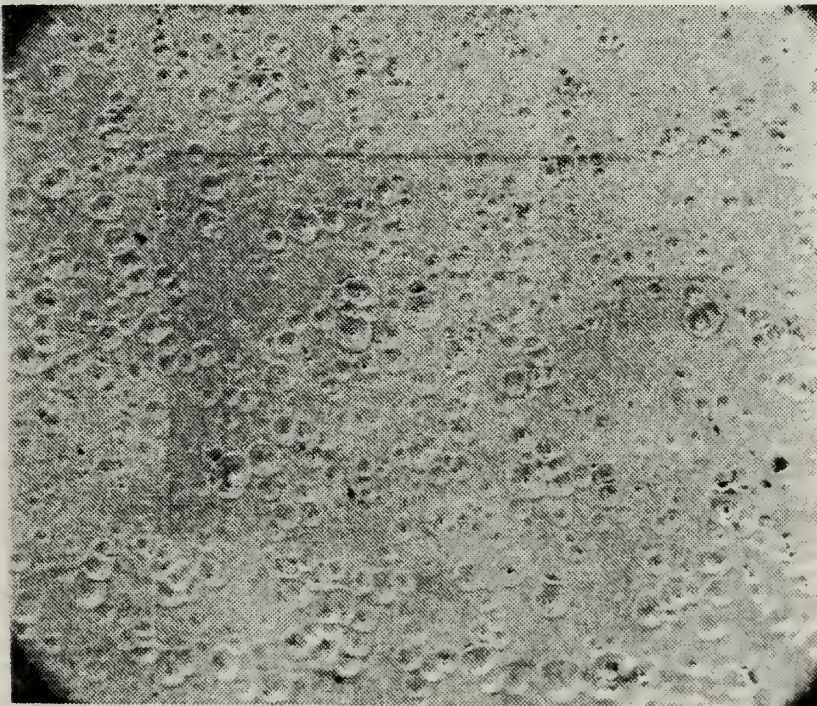


Figure 67. 304 Stainless. Area shown in the previous figure at a higher magnification (260X SEM)

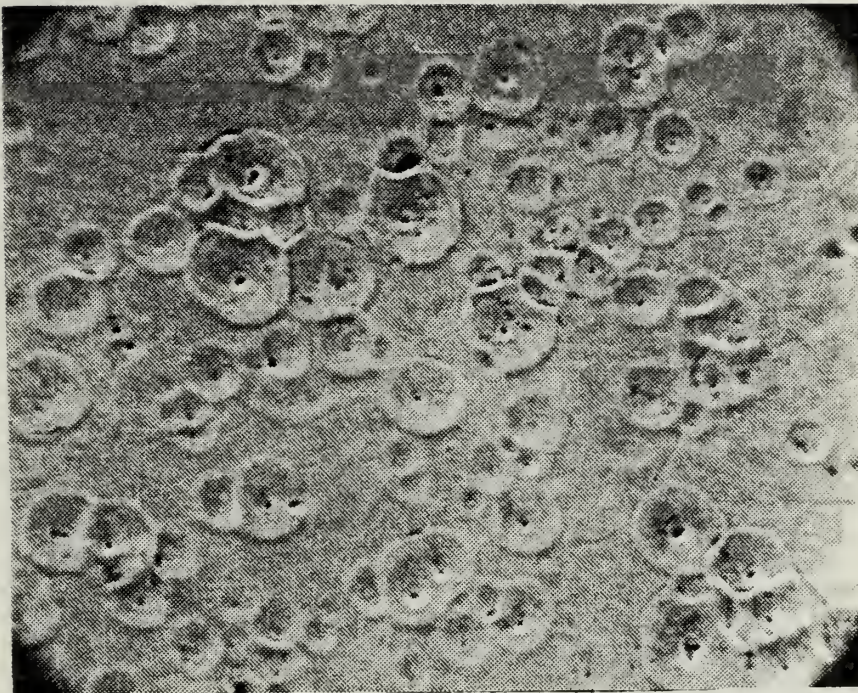


Figure 68. 304 Stainless. Area shown in previous figures at a higher magnification (650X SEM)

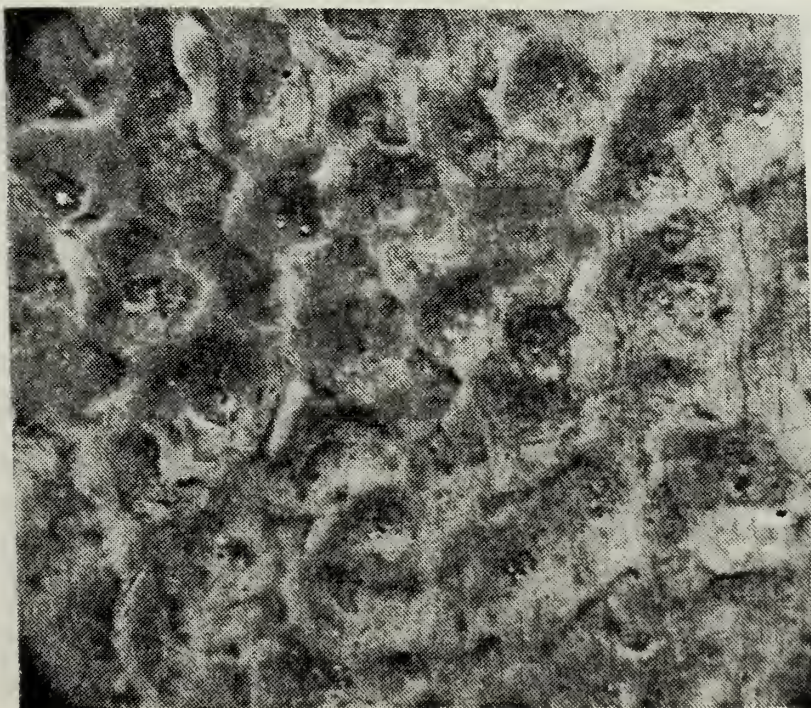


Figure 69. 304 Stainless. Acid etch of unipolar arcs and molten surface effects (650X SEM)

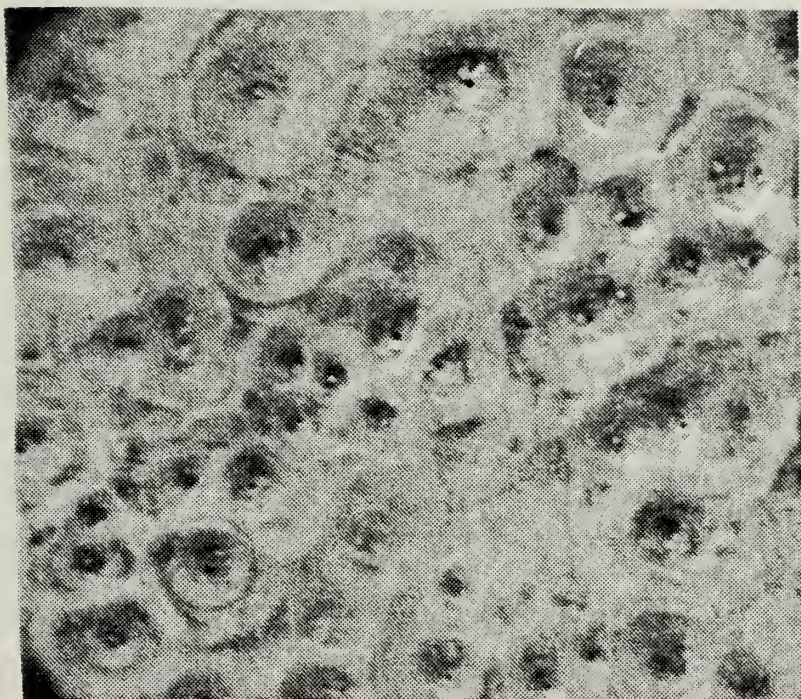


Figure 70. 304 Stainless. Acid etch of unipolar arcs showing different effects (650X SEM)

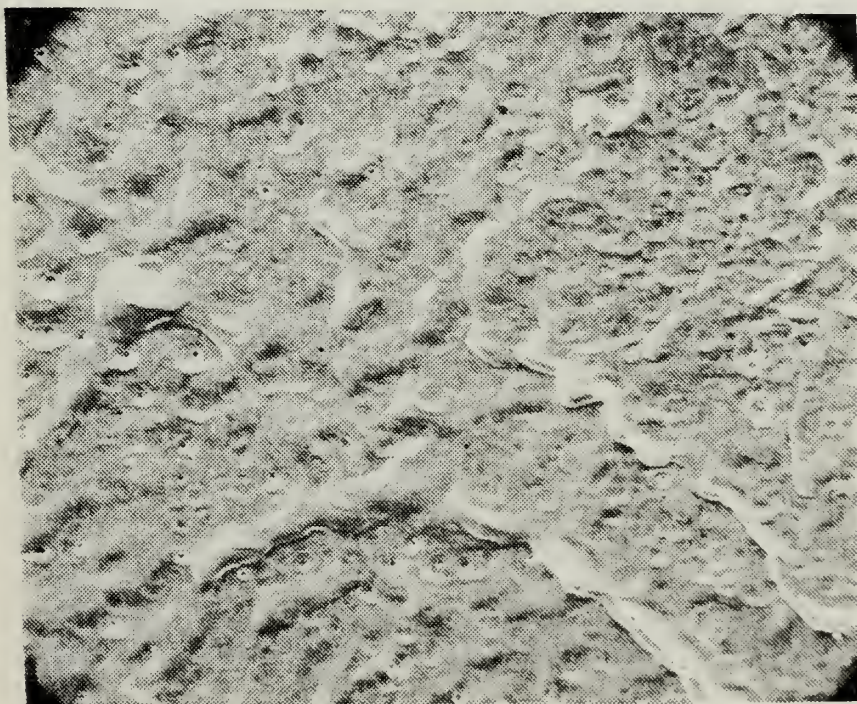


Figure 71. 304 Stainless. Main crater number two from the second three-shot sequence (260X SEM)

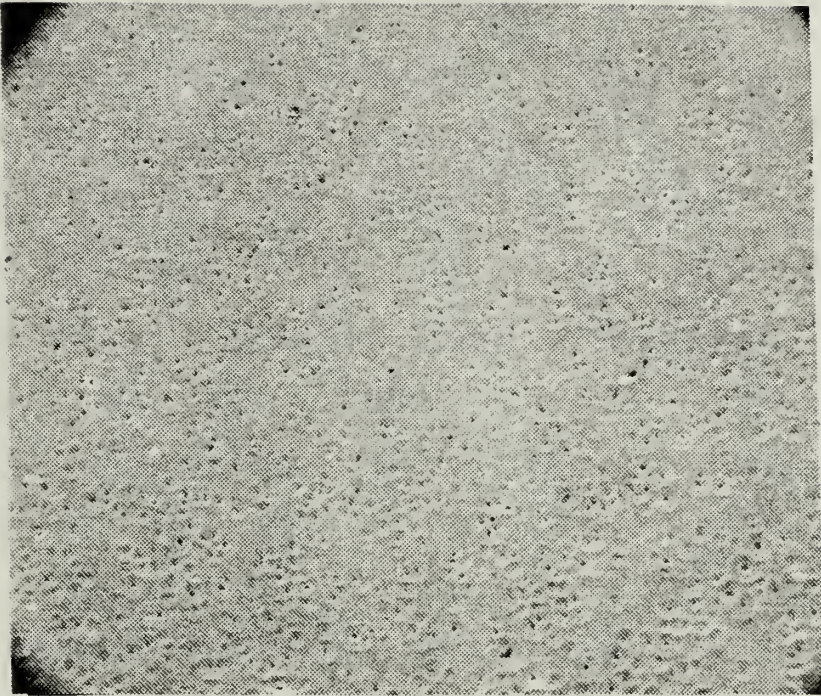


Figure 72. 304 Stainless. Unipolar arcing 2.5mm from the third laser pulse (260X SEM)

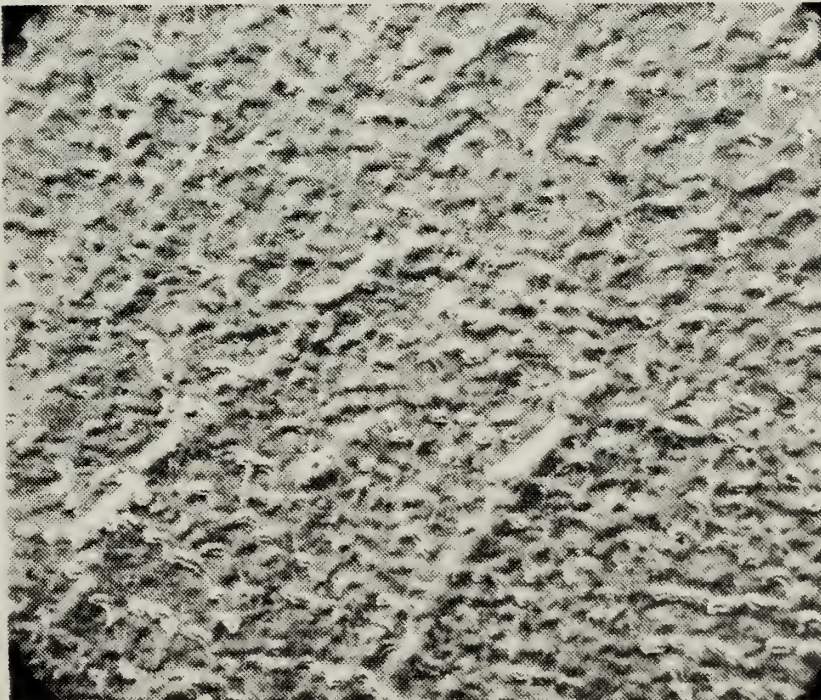


Figure 73. 304 Stainless. Surface produced by a seven pulse sequence (130X SEM)

would provide the test plasmas for determination of unipolar arc susceptibility of the laser glazed surface. After shots 6 and 7, the sample was examined under the SEM at magnifications up to 2100X. Unipolar arcs could be found only at distances greater than 3mm from the center-line of the molten surface effects, with the glazed surface visually similar to that of the commercial metallic glass $\text{Fe}_{30}\text{B}_{20}$. Figures 73, 74, 75, 76, 77, and 78 show the resulting surface structure, produced by the seven shot sequence, at various areas and at successively higher magnifications. Cathode spots from unipolar arcs that have been "glazed over" are visible; however, no new unipolar arcs were found on this surface. Figure 79 shows the typical arc densities found outside the glazed area with the bottom of the figure being at an approximate distance of 3mm from the center of the "glazed" surface.

After examinations of the surface were completed and photographs taken, the target sample was cut with a low speed diamond saw so that a cross section of the glazed area was obtained. After polishing with a 0.05 micron slurry of Al_2O_3 , the sample was etched electrolytically using 10 grams of oxalic acid in 100 ml of water, and then examined optically to determine the extent of laser effects (if any), from the seven shot sequence, into the stainless. Figures 80, 81, 82, 83, and 84 show, at 500X, the etched cross section at various points along the laser-target interaction area, with the black areas at the top being the bakelite mounting material, and the laser glazed surface abutting the bakelite. Immediately noticed, was the horizontal line running almost the entire length of the cross section approximately 5 microns below the laser-target surface interaction area. It is thought that this

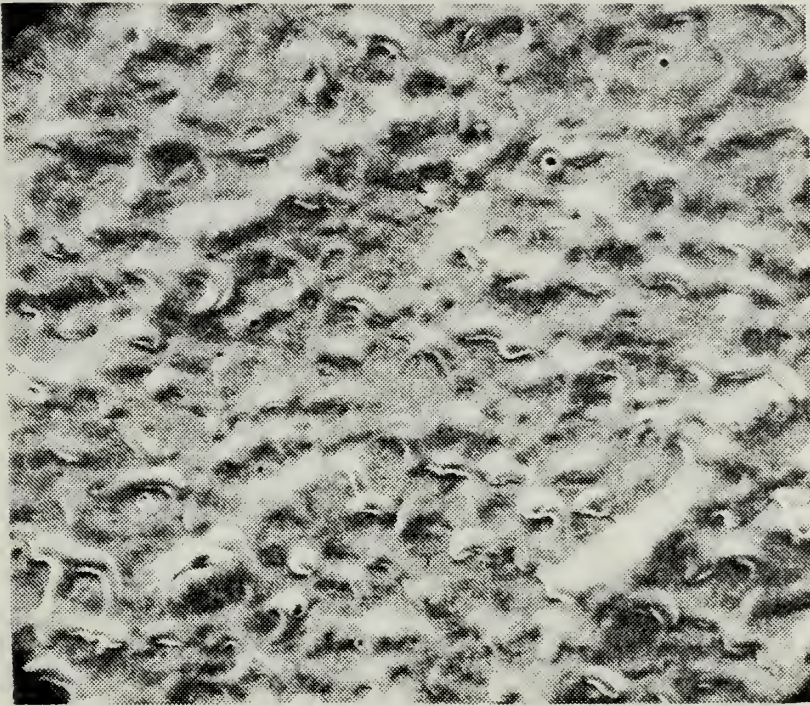


Figure 74. 304 Stainless. Same surface area as previous figure but at higher magnification (260X SEM)

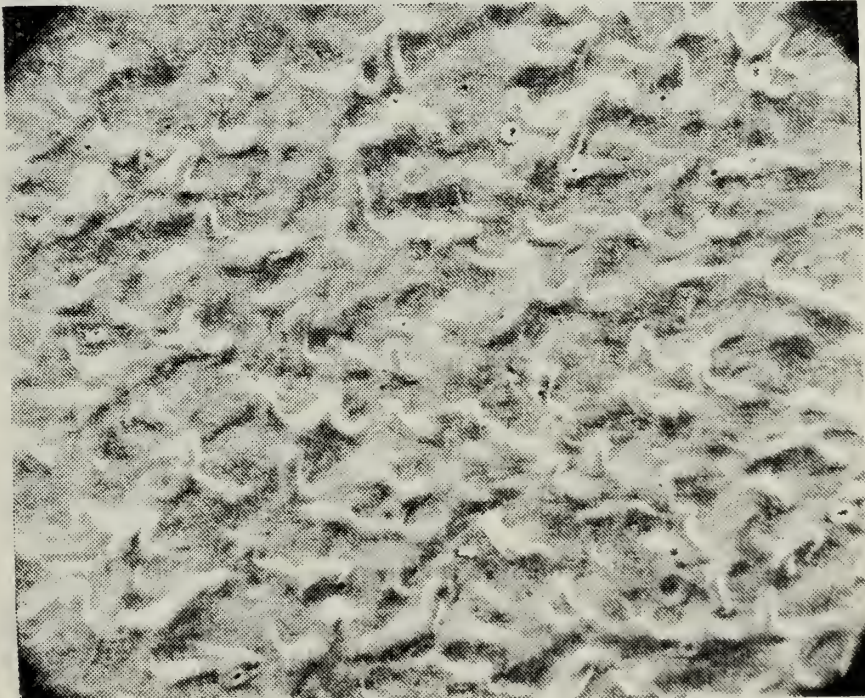


Figure 75. 304 Stainless. Surface produced by seven pulse sequence, 5mm from previous figure (260X SEM)

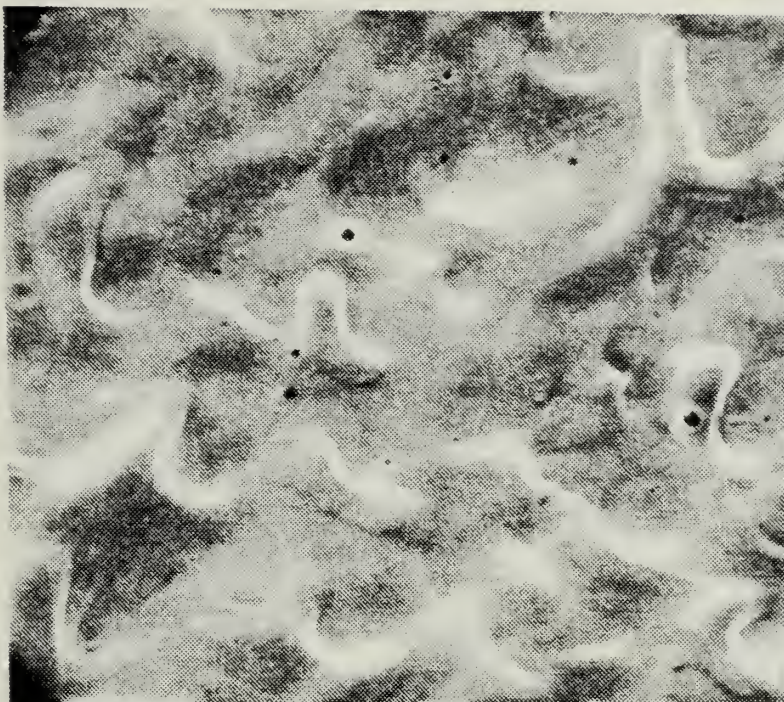


Figure 76. 304 Stainless. Same surface as previous figure but at higher magnification (650X SEM)

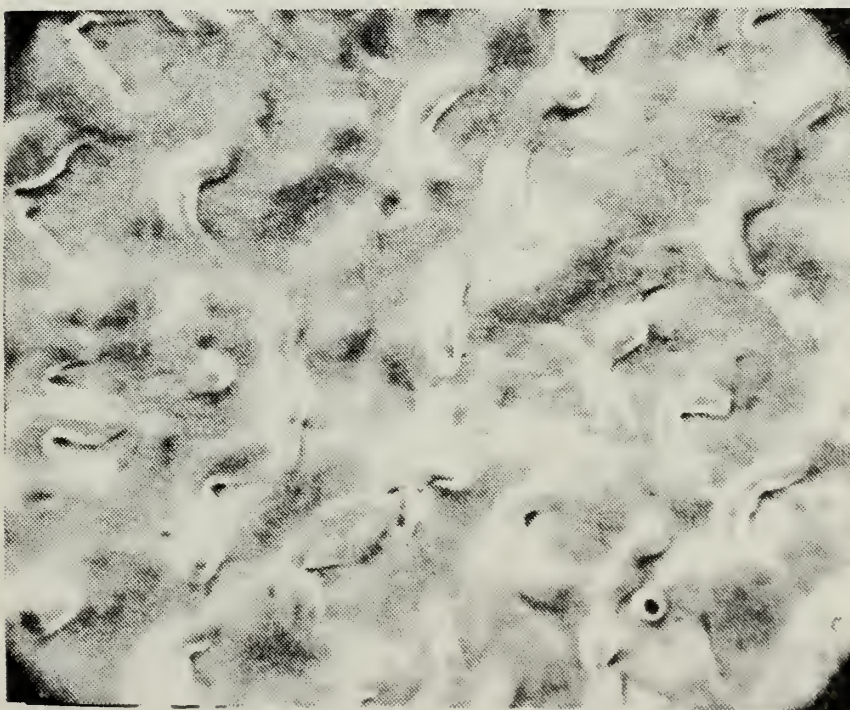


Figure 77. 304 Stainless. Another surface view from seven pulse sequence (650X SEM)

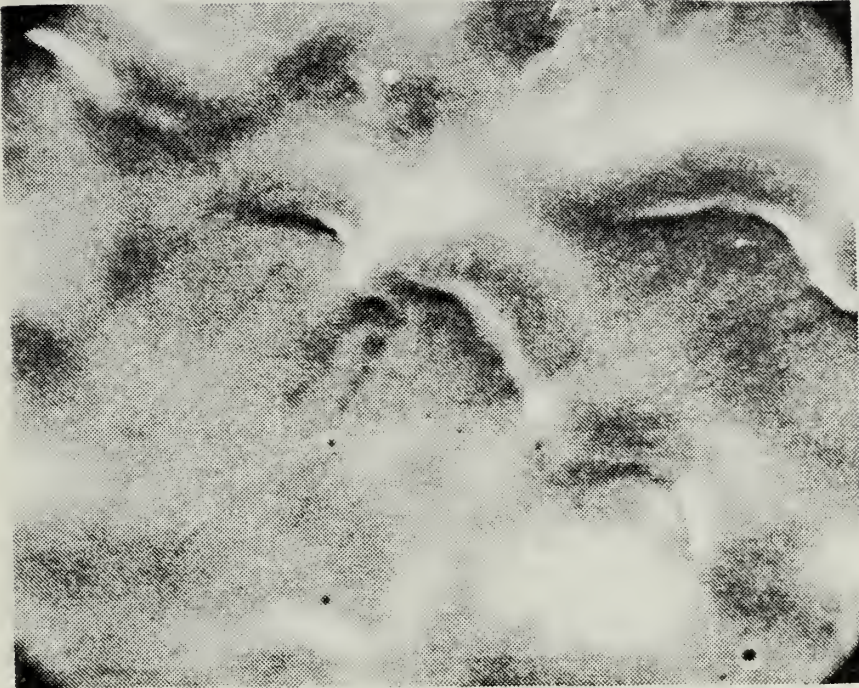


Figure 78. 304 Stainless. Close up of molten surface effects from seven pulse sequence, same area as in previous figures but at greater magnification (1300X SEM)



Figure 79. 304 Stainless. Unipolar arcing seen at cessation of molten surface effects for seven-pulse sequence (260X SEM)

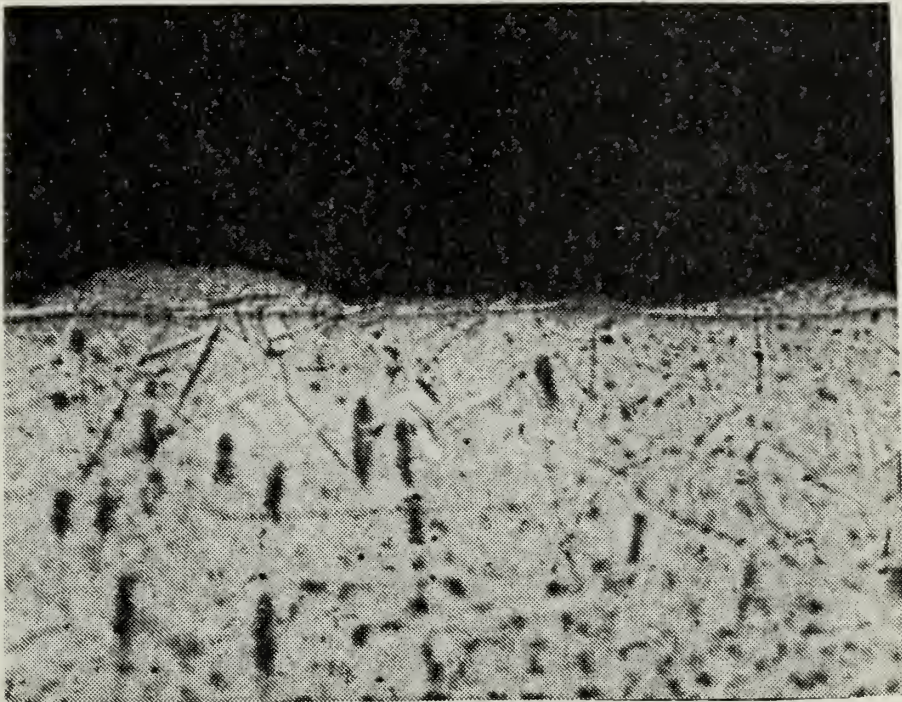


Figure 80. 304 Stainless. Etched cross section of seven-pulse sequence. Note crystal structure crosses crack line (500X optical)

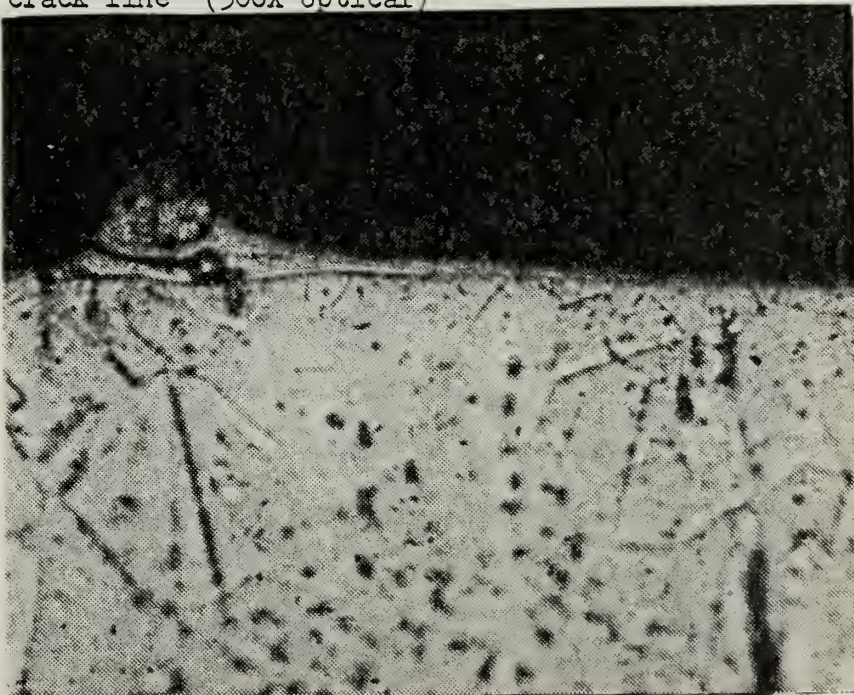


Figure 81. 304 Stainless. Etched cross section of seven pulse sequence. Note main laser crater rim in cross section (500X optical)

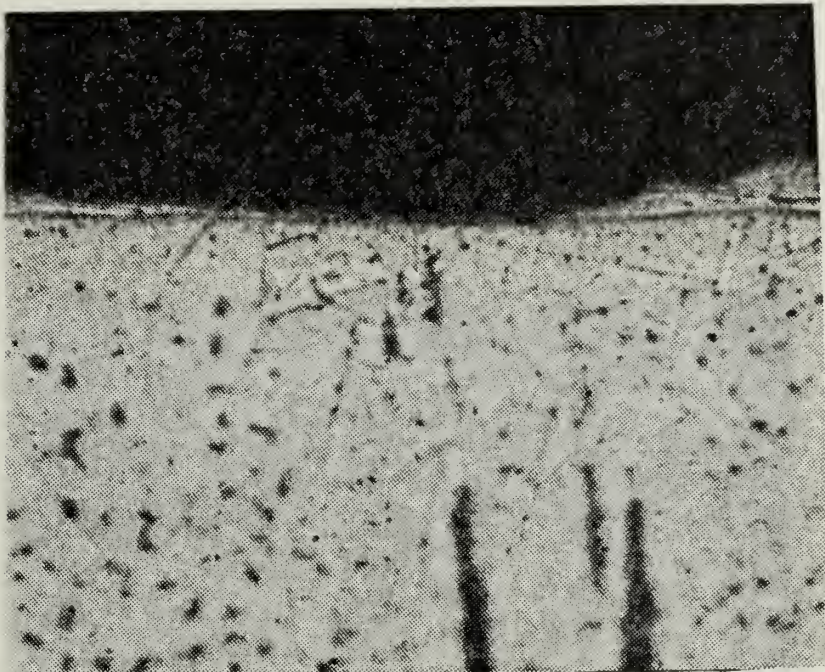


Figure 82. 304 Stainless. Etched cross section. Main laser crater shown in previous figure lies immediately to the left. (500X optical)

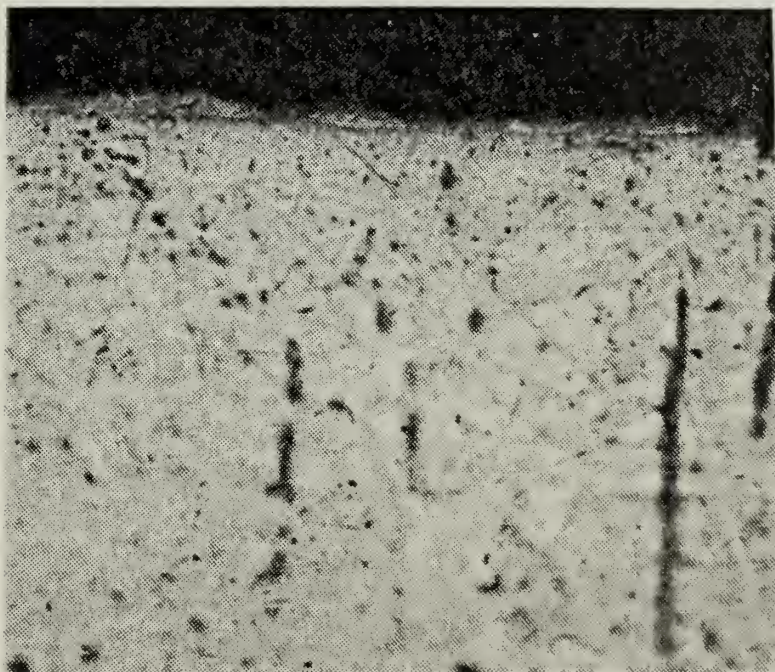


Figure 83. 304 Stainless. Etched cross section. Crystalline microstructure can apparently be seen extending up to the surface (500X optical)

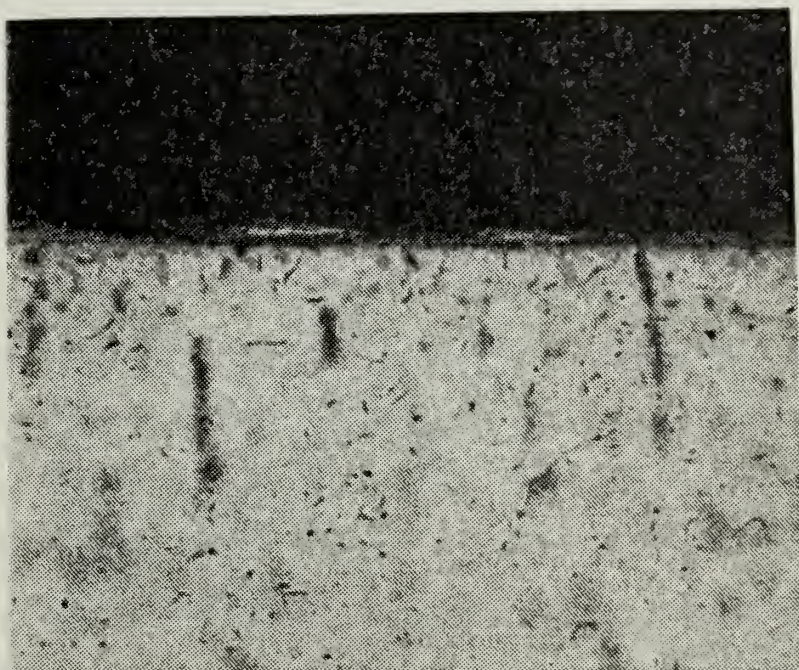


Figure 84. 304 Stainless. Etched cross section. Ridge-like structure corresponds to molten surface effects (500X optical)

line is probably a subsurface crack with its depth below the surface varying from 3 to 13 microns. Examination of the crack shows evidence of the starting annealed microstructure extending across the crack. However, no crystalline material as evidenced by grain boundaries could be discerned anywhere within 3 microns of the surface. This can be easily seen in the left side of figure 80.

Also seen in the figures is a layering effect which appears to start upon the cessation of verifiable stainless steel microstructure. This layering effect appears to begin at the surface and extend 3 to 10 microns in depth into the material, but never beyond the crack depth. It is thought that the crack was created by a combination of the steep temperature gradient near the surface during laser irradiation and the shock wave, created by recoiling material upon initial impact of the laser pulse, reflected from the back side of the target. With the shock wave returning approximately 1 microsecond after irradiation, its arrival would find the surface still molten, but areas at a 5 to 10 micron depth still crystalline; thus, it is believed the combination of at least a 1.6×10^8 °C/meter temperature gradient and shock wave created the crack. The layering effect seen probably is the result of stress wave impingement on the steel while it is in a semi-molten state though this is not a certainty.

3. Type 316 Stainless Steel

Attempts to examine the susceptibility of laser glazed surfaces on 316 stainless to unipolar arcing were made using the second technique used on 304 stainless. Two three shot sequences were made following the same routine and shot location for the 316 targets as for 304 targets (see Appendix B).

The results of one of the linear three shot sequences, where main laser crater centers lie approximately 2.5mm apart, are shown in figures 85, 86, 87, and 88. Figure 85 is a photograph of the center of the main laser crater from the third or last shot. It shows an etching effect probably due to sputtering, as did the 304 stainless, and was used for comparison with figure 86, which shows the center of the crater from the second shot. Seven new unipolar arcs can be seen in figure 86, which should then be compared with figure 87. Figure 87 shows an area of unipolar arcing that is 2.5mm from the center of crater three, opposite of crater two. Figure 88 is a photograph of an area, outside of main crater two, lying approximately 2mm from crater three's center, and shows no new unipolar arcs.

Results from the first three shot sequence were similar to those of the second sequence, with the density of new arcs being produced on the "laser glazed" surface being less than the arc density on the polished surface given equal plasma densities over both surfaces. No large differences were noted when comparing 304 glazed surfaces with 316; however, as noted previously, polished 316 seems to arc over a slightly smaller area, given the same laser pulse energy, than polished 304, so it would seem that a 316 glazed surface should be more unipolar arc resistant by a small amount.

4. HY 130

Only one three shot sequence was made on an HY 130 target sample. Two shots were made such that the resulting main laser rims were separated by 0.25mm, and a third shot, to create a test plasma, was made 2mm away from the second crater. Laser energy for the first

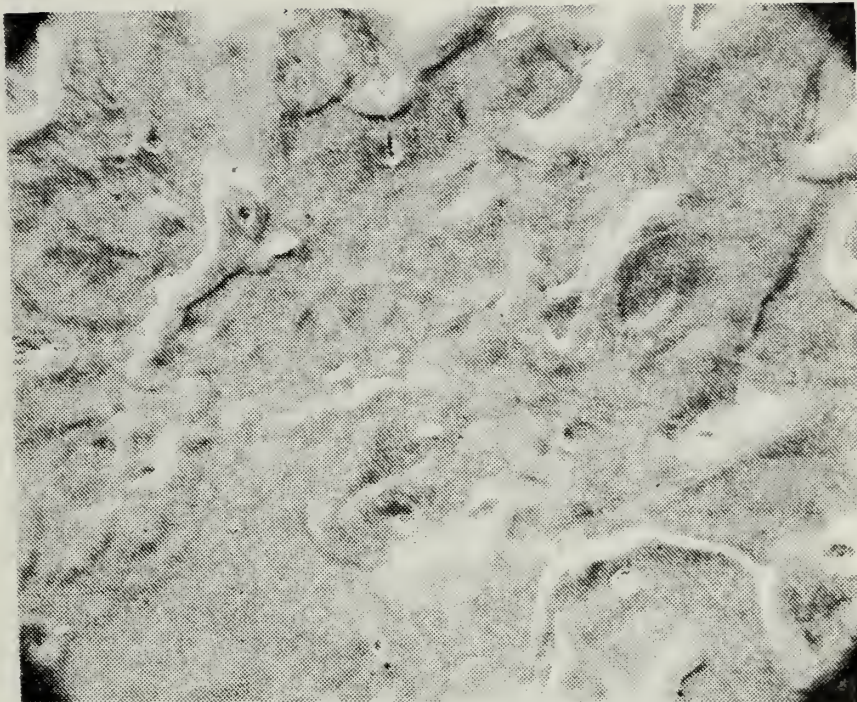


Figure 85. 316 Stainless. View (center) of main laser impact crater resulting from pulse three (650X SEM)

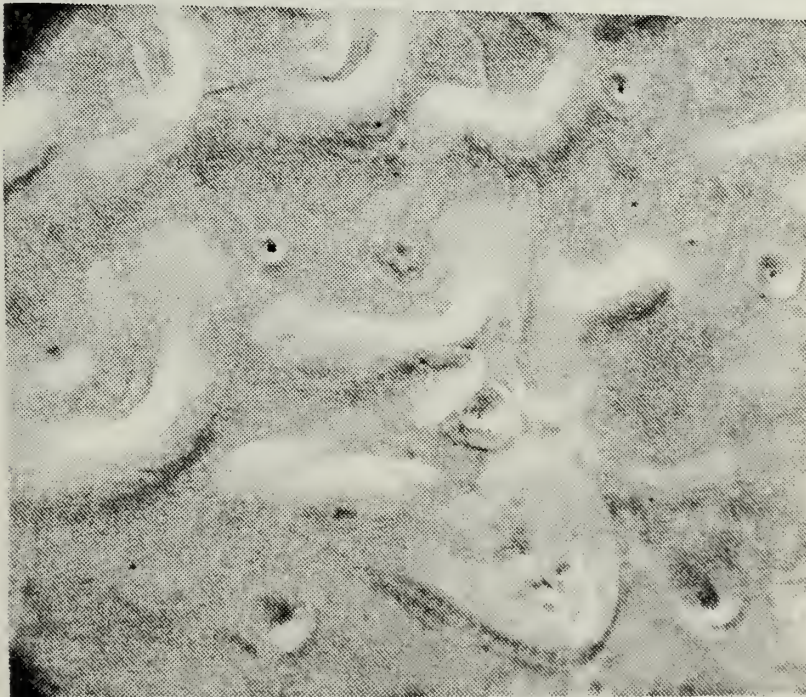


Figure 86. 316 Stainless. View (center) of main laser impact crater resulting from pulse two and after exposure to plasma produced by pulse three (650X SEM)

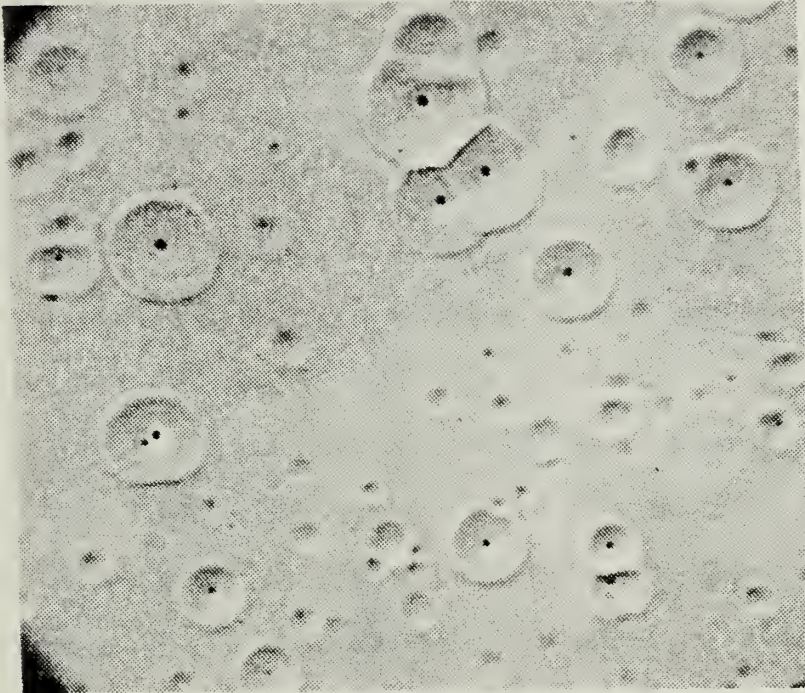


Figure 87. 316 Stainless. Unipolar arcing seen at distance 2.5mm from main laser impact crater number three (650X SEM)

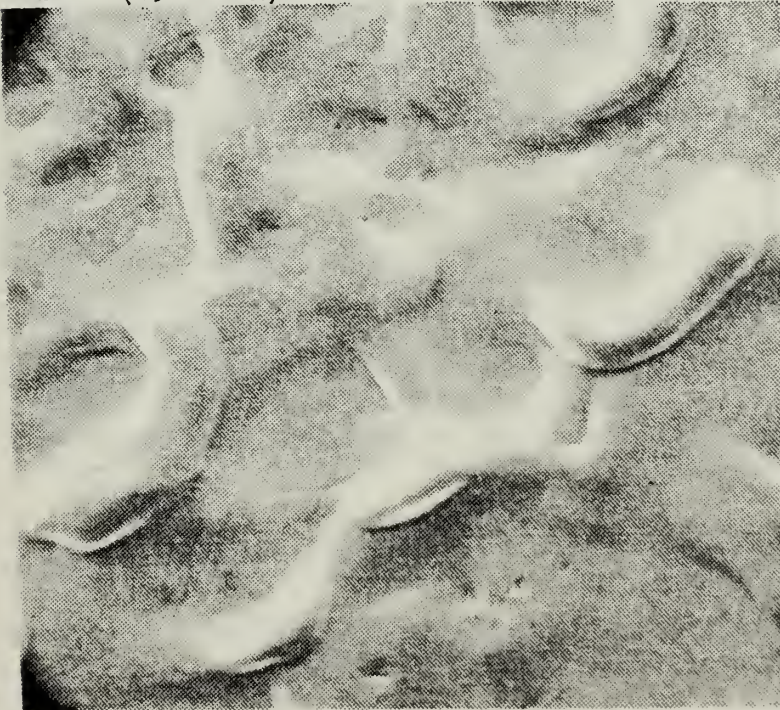


Figure 88. 316 Stainless. Molten surface effects resulting from pulse two, 2mm from main laser impact crater of pulse three, after exposure to plasma produced by pulse three (650X SEM)

two shots was 11 Joules while the third shot was one of 12 Joules. Focal spot diameters were all 0.4mm. Figure 89 shows the area between the main craters of the first two shots, while figure 90 shows an area outside of main crater two, with the left side of the figure approximately 1mm from crater three. Both figures show a plasma etched surface revealing a martensitic microstructure, an effect that was noted in the previous section on HY 130. No unipolar arc density reduction effect was noted on the glazed surfaces when compared to the one shot polished surface arc densities; however, since there is a paucity of unipolar arcs found in the few HY 130 plasma interactions studied, no real comparison can be made. It is believed by the author, however, that very fine or martensitic microstructures will be proved more arc resistant than the coarse grained structures; and that, by glazing the HY 130, one obtains a surface of refined martensite, which could be more unipolar arc resistant than HY 130's regular microstructure of tempered martensite.

5. 1030 Steel

As with the 316 samples, two three-shot linear sequences were fired at polished 1030 steel targets. Both samples had a hardness of 42 on the Rockwell B scale and had a coarse microstructure predominately of ferrite.

For one three-shot sequence, the first two laser pulses were both 11 Joules, had focal spot diameters of 0.5mm, with a distance of 1.25mm between resulting main laser crater centers. A third pulse of 11.3 Joules had a focal spot of 0.35mm diameter. The main crater produced by this third pulse was 1.5mm from the crater produced by the

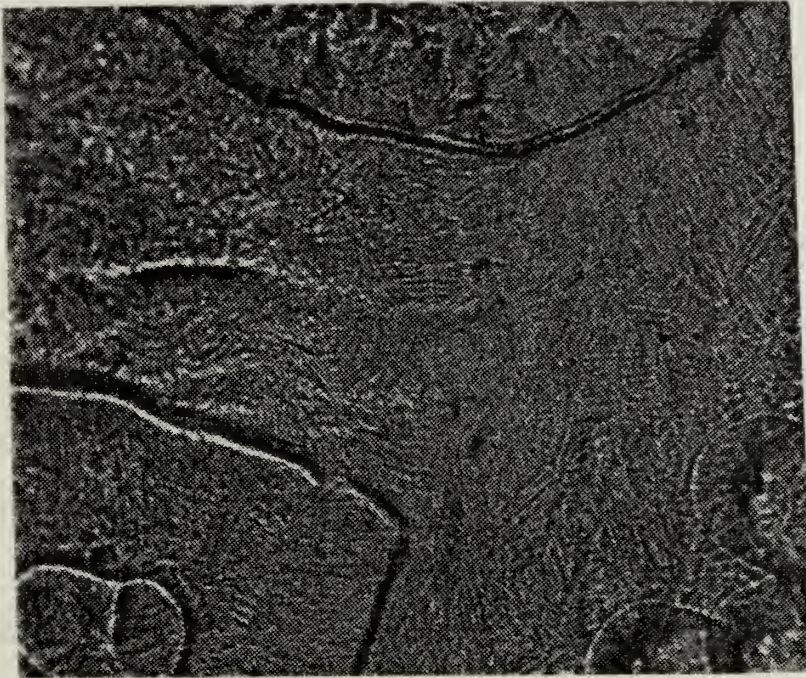


Figure 89. HY 130. Area between and around main impact craters from pulses one and two (160X optical)

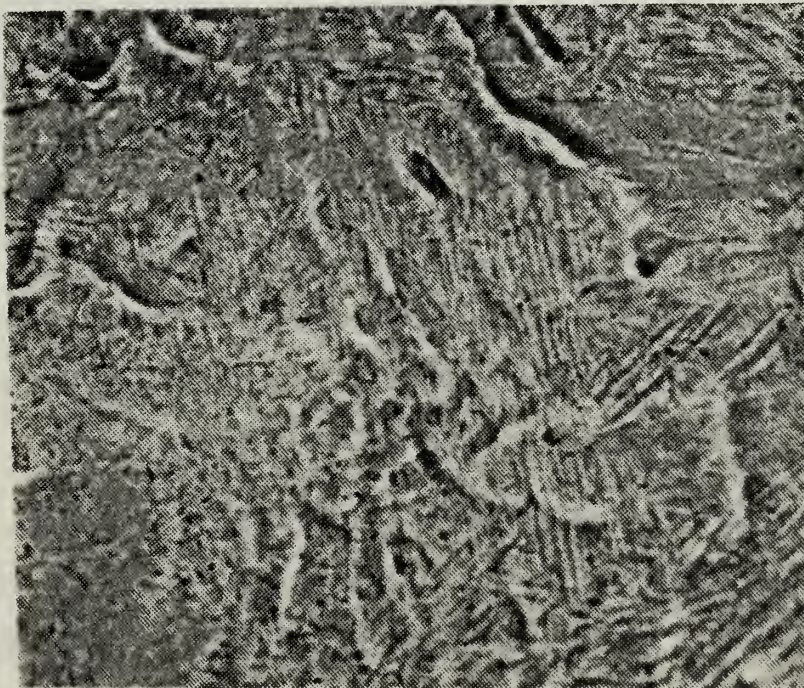


Figure 90. HY 130. Area near main laser impact crater number two (500X optical)

second pulse (center to center). Figure 91 shows the main crater of the second pulse after it had been exposed to the plasma produced by the third pulse. Surface area seen in this figure is approximately 0.75mm^2 with several hundred new unipolar arcs seen. Figures 92 and 93 show areas of crater number two at 600X. As in other samples, these two figures seem to show a surface that has undergone etching by the plasma. If this is the case, then the microstructure for surface material has been refined considerably with the photographs showing a martensitic microstructure. For comparison with the arc densities shown in figures 92 and 93, figure 94 has been provided. This figure shows an area lying 2.0mm from the third main crater and directly opposite from crater number two. Unipolar arc densities in figures 92 and 93 are less than seen in figure 94; however, the few arcs in the figures 92 and 93 are much larger than those in figure 94.

A second three shot sequence was done with the first two pulses having energies of 11 and 8 Joules, and the third having an energy of 10 Joules. The main laser craters for the first two pulses lie 1mm apart (center to center) while the third pulse producing the test plasma created a main crater that was 2.5mm distant (center to center) from crater two. Figure 95 shows the main crater produced by laser pulse number two; while figure 96 shows an area, in main crater two, which was approximately 2.6mm from crater three. No new unipolar arcs were seen, the few "washed out" arcs seen are the result of the first laser shot. Figure 97 shows an area on the opposite side of pulse three's main crater from crater two, with the bottom edge of the figure being approximately 2.4mm from main crater three's center. Apparently, the lower

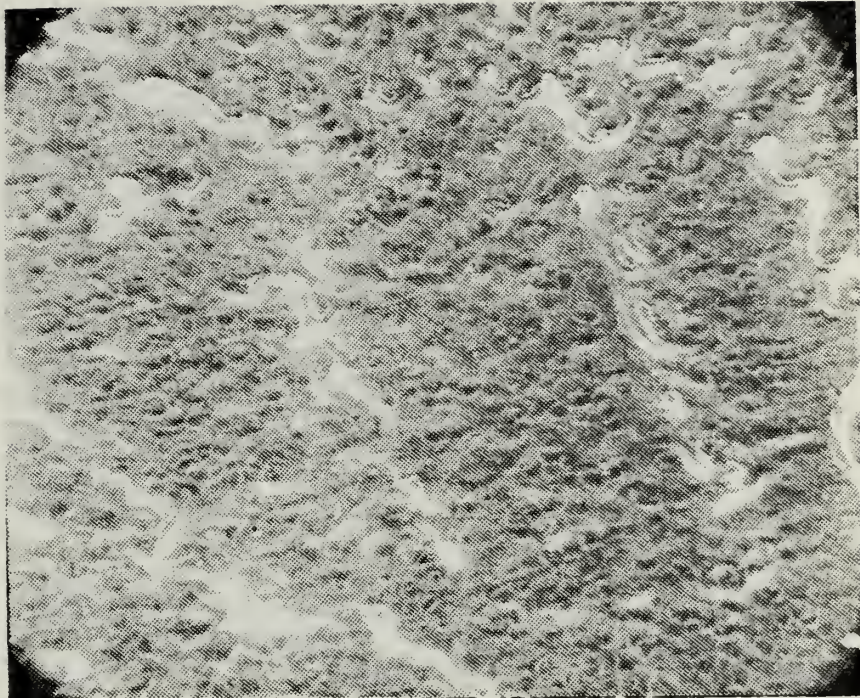


Figure 91. 1030 Steel. Main laser impact crater of pulse two after exposure to plasma produced by pulse three (125X SEM)

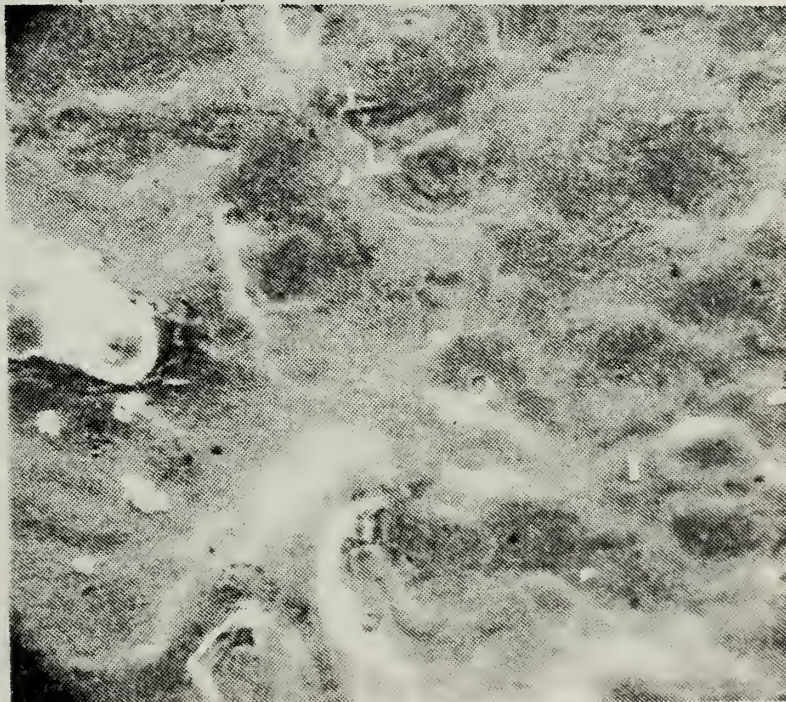


Figure 92. 1030 Steel. Close up of area in main crater two (600X SEM)

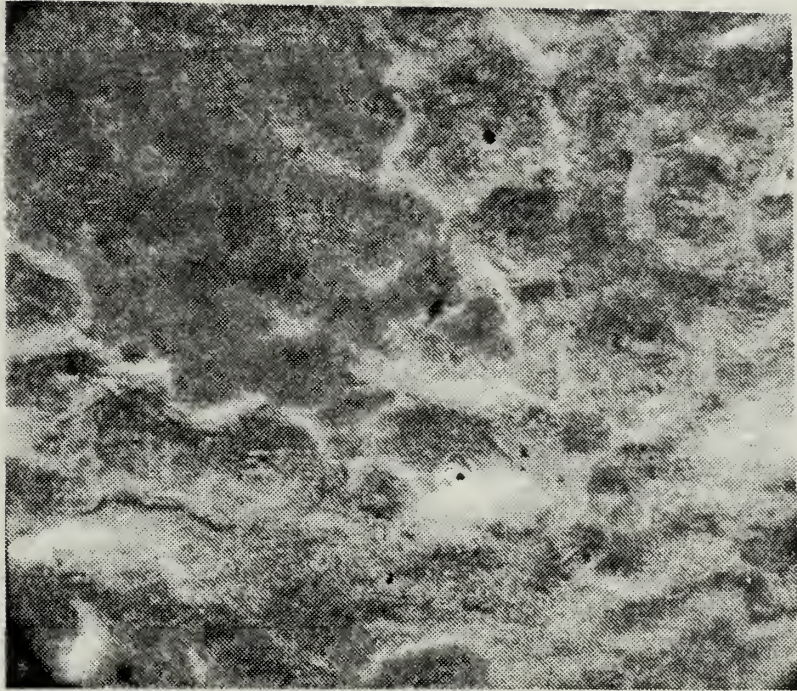


Figure 93. 1030 Steel. Close up of area in main crater two (600X SEM)

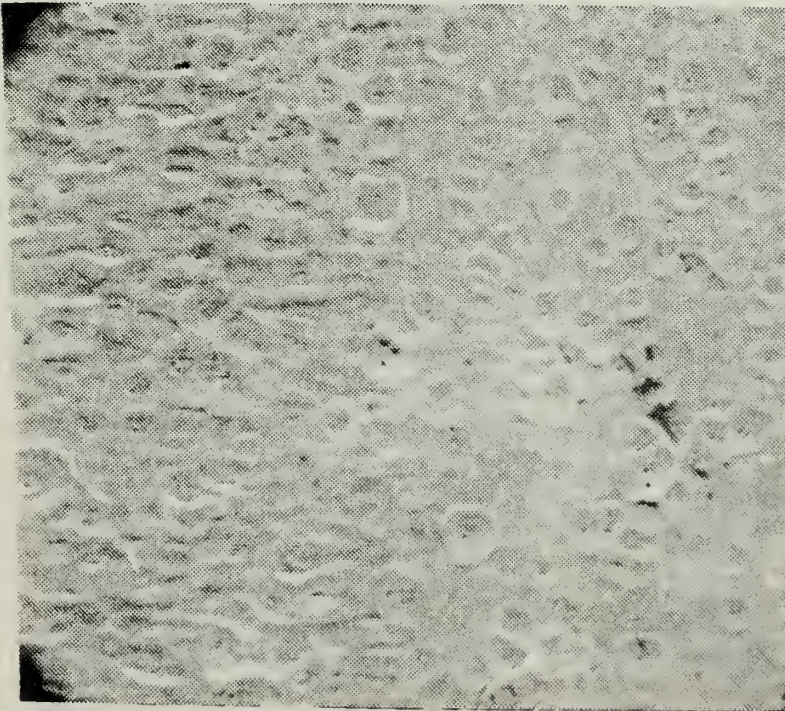


Figure 94. 1030 Steel. Unipolar arcing seen from distance of 2mm from main laser impact crater three (600X SEM)

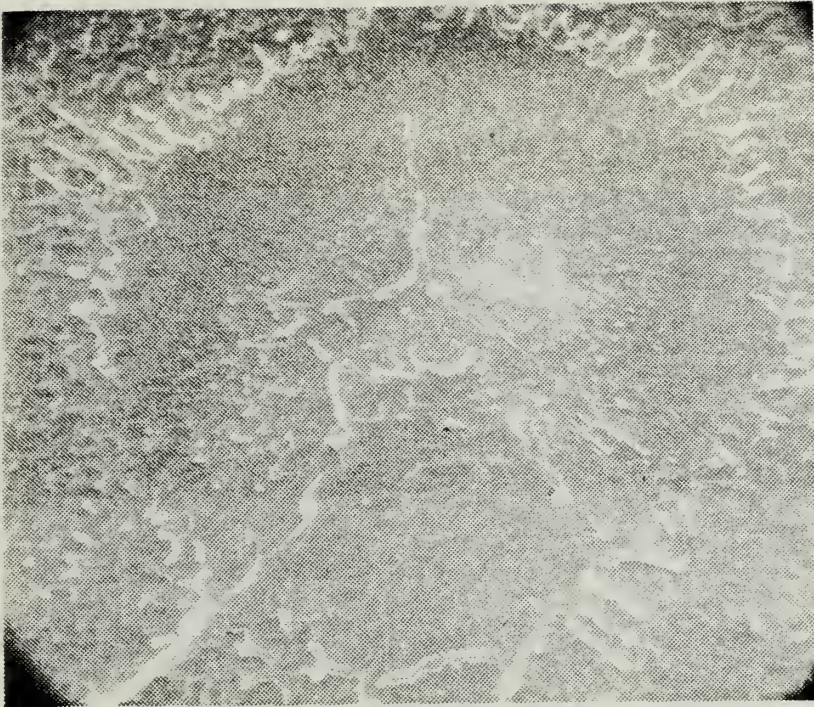


Figure 95. 1030 Steel. Main laser impact crater produced by pulse two, after exposure to plasma produced by pulse three; in second three-shot sequence (120X SEM)

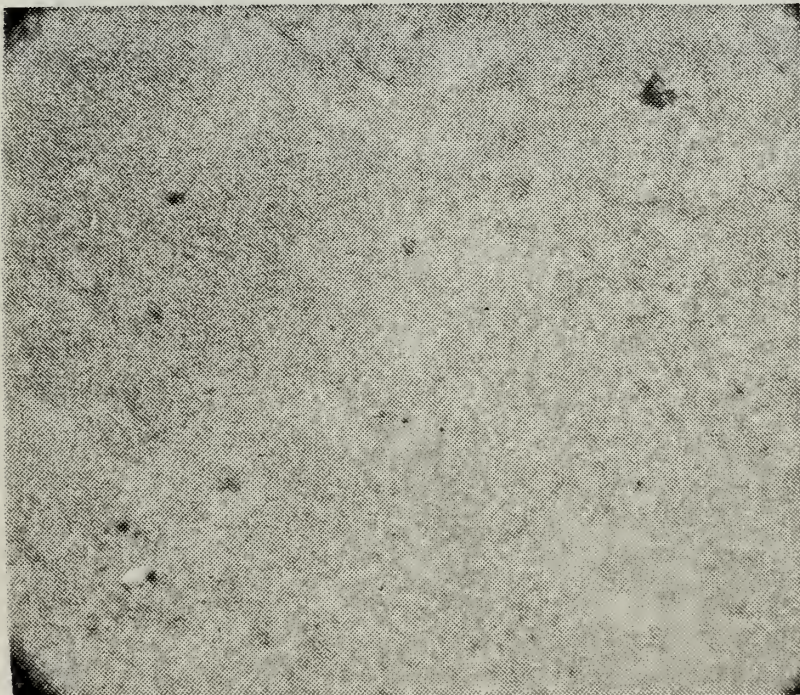


Figure 96. 1030 Steel. Close up of area seen in upper left corner of main crater seen in previous figure (1100X SEM)



Figure 97. 1030 Steel. Unipolar arcing at distance of 2.4mm from main laser impact crater three (1100X SEM)

plasma density produced by the test pulse of the second sequence in crater two was insufficient to initiate unipolar arcing in the glazed areas of crater two. The higher plasma density, due to the fact that the test pulse in this case was closer to the glazed area, of the first sequence, was of sufficient density to initiate unipolar arcing in the "glazed" surface; albeit at a lower arc density when compared to a polished surface exposed to the same plasma density.

V. CONCLUSIONS

The work on this thesis was directed towards discovering the degree of unipolar arc damage on various materials when they are exposed to a plasma environment, and to discover methods that can be employed to impede unipolar arc initiation in materials that arc heavily. To this end, the following conclusions have been made for the materials tested:

99.9% pure titanium, which is used on some components in the plasma environment of Tokamaks, exhibited the greatest propensity towards arcing of any of the metals tested. Molten surface effects covered approximately twice the surface area, per Joule applied, than the area of effects on the steels. Unipolar arcing was also seen to occur over the entire target surface. This implies that titanium should not be used in any plasma environment where contamination by high Z elements is of concern.

The carbon material tested showed no propensity towards arcing, at least no cathode spots could be discerned amid the porous surface; however, the erosion of the original surface was quite pronounced. For an 11.9 Joule focused pulse irradiation, excluding the main laser impact crater, the volume of material removed by the plasma was approximately 0.060mm^3 . This value assumes a circular interaction area with a $5\mu\text{m}$ erosion of the original surface at the edge of the main laser impact crater, no erosion at a 3.5mm radius, and the amount of erosion varying linearly as a function of the radius. The volume of material removed from the main impact crater was approximately 0.44mm^3 . This

indicates that sections of Poco graphite probably will erode "rapidly" if used as a limiter in fusion reactors, and may have only limited utility in a dense plasma environment.

Of the steels tested, both stainless types and 1030 exhibited approximately the same high degree of susceptibility to unipolar arc damage, though type 316 stainless does exhibit a slightly lower density of arcing at equivalent plasma densities. The one steel that showed a low susceptibility to arcing was HY 130, though once a unipolar arc did initiate, it apparently tended to burn long and vigorously. This tends to confirm the model of arc cessation put forth by Ryan and Shedd [Ref. 4], which essentially states that the material removed by arcing from the crater area and enters the plasma, serves to cool the plasma until it no longer has the sheath potential required to sustain the arc. With a five orders of magnitude lower arcing density in HY 130, when compared to the other steels, it is apparent that more plasma energy can go into each arc, enabling that arc to burn much longer than a corresponding arc in stainless before the sheath potential is reduced enough for arc cessation. The reason for the low arc density in HY 130 is unknown.

Sandblasting appears to be a viable method of reducing the density of arcing on a material, as long as polished surface smoothness is not a prerequisite for use of the material. Unipolar arc density was reduced in both copper and stainless steel samples tested after sandblasting, with few arcs seen beyond a radius of 1.5mm from laser impact.

It is felt that the SiO_2 surface coating produced by sandblasting acts as an inhibitor to unipolar arcing, in spite of the fact that the surface is rough and jagged which should act as an electric field, and therefore unipolar arc enhancer.

As noted by Ryan and Shedd [Ref. 4], commercial metallic glasses appear to be resistant to unipolar arcing. Results obtained with $\text{Fe}_{80}\text{B}_{20}$ tend to confirm that statement. No unipolar arcs were observed on $\text{Fe}_{80}\text{B}_{20}$ outside of a small molten area abutting a hole burned through the ribbon by the laser. Upon initiation of crystallization of the metallic glass, the number of unipolar arcs, and the area affected by unipolar arcing, increased. It seems that metallic glasses would be ideal for use when a metal surface is to be exposed to a plasma so long as temperatures and exposure times are not great enough to recrystallize the glass; however, since the only commercial metallic glasses available are in ribbon form, their utility seems very limited.

Attempts to produce a metallic glass surface layer over a large area by laser glazing the various steels produced uncertain results. Unipolar arcing is apparently greatly reduced on steels that have been previously irradiated by laser radiation, with a complete cessation of arcing seen on a 304 stainless steel target after irradiation by seven laser pulses. It is suspected that a very thin layer, perhaps only 200 angstroms thick, of metallic glass is formed in the area of molten surface effects, and that the process of unipolar arcing, itself, produces a surface metallic glass layer due to the short lifetime of the arc.

Ryan and Shedd stated that they believe a metallic glass layer is formed immediately upon arrival of the incident laser pulse and that, when unipolar arcing occurs on this layer, the molten core of the arc lifts up the metallic glass layer and forms the metallic glass crater rims they observed. The author feels that this is not the case. It is felt that the metallic glass crater rims they observed were produced by molten material pushed up out of the cathode spots and solidified at a cooling rate in excess of $1,000,000^{\circ}$ C/sec. Thus, it is felt, on certain alloys the process of unipolar arcing will self-extinguish eventually by the production of a surrounding arc resistant metallic glass surface layer around the arc crater. It is felt that this is the reason no unipolar arcing could be found on the seven pulse irradiated stainless steel surface. Simply put, the seven pulses produced so many unipolar arcs that, in conjunction with other surface effects, eventually a thin layer of metallic glass completely covered the surface, which was now also free of any surface impurities that aid in unipolar arc initiation.

The uncertainties of that idea arise from observations of the laser glazed stainless steel in cross section and of the glazed surfaces of 1030 and HY 130 steels. As closely as could be examined, the microstructure of the seven shot stainless steel target seemed to be intact up to the surface, though observation of a 200 angstrom thick surface layer was impossible by the optical means used to evaluate the depth of the surface effects. In the 1030 and HY 130 steels, especially the HY 130, the surface of the target material appeared to be etched by the laser produced plasma, revealing a martensitic microstructure.

It may be that, instead of a metallic glass layer being formed, a thin homogeneous layer of martensite is formed on some glazed steels, and being cleaned of surface impurities by the laser produced plasma, is very resistant to unipolar arc initiation. These results suggest that the microstructure of a material influences its resistance to unipolar arc initiation.

In either case, even if a very thin surface layer of metallic glass resistant to unipolar arcing was formed, the target material had to be shock hardened in the area beneath and abutting the main laser impact crater. Power densities in that area were of the order of 10^{10} W/cm² for approximately 25 nsec, which should produce a hard homogeneous layer of fine microstructure [Ref. 14]. It is felt that, even if the layer of metallic glass were not there, these hardened layers would be resistant to unipolar arcing because of their homogeneity and cleanliness and because of the high electrical resistivity of individual grain boundaries [Ref. 18]. With a very fine microstructure, it is felt that the grain boundaries may inhibit the return microcurrent flow of electrons required for unipolar arcing. Thus, whether a metallic glass layer or a hardened crystalline layer is at the surface, either layer should inhibit unipolar arc initiation. It may be noted that unipolar arcing has occurred when some targets were still in a molten state where electrical resistivity is high. It is felt that the increased vapor pressure of the molten metal compensates for the high electrical resistivity.

VI. RECOMMENDATIONS

The results of this thesis raise many questions and suggest many areas for further study. Results of this thesis suggest that coarse microstructures such as those that exist in annealed stainless and 1030 steels undergo unipolar arcing easier than a steel of martensitic microstructure such as HY 130. A study of the effect of steel microstructure on unipolar arcing is recommended. For example, the effect of microstructure on unipolar arcing could be studied by heat treating a hardenable alloy steel, such as AISI 4140, to produce various microstructures varying from fine untempered martensite to coarse pearlite.

Further studies on the effect of sandblasting impeding arc initiation appear warranted. The sandblasted surfaces evaluated proved to provide a high degree of resistance to unipolar arcing, and showed less laser surface interaction damage than their polished counterparts. In order to separate the effects of surface hardening and impregnation of SiO_2 on the surface, samples could be "sand" blasted with different particles ranging from metallic to ceramic. It is recommended that experiments be conducted to determine the susceptibility of insulating materials to unipolar arcing, and to determine methods of coating conductors with insulating materials that will not be damaged by thermal effects and that are resistant to unipolar arcing. Sandblasting appears to provide an insulating coat of SiO_2 , but it is not 100% effective as was a coating a conductor with titanium carbide was shown to be by Keville and Lautrup [Ref. 19].

Experiments showed that a metallic surface that has undergone multiple exposures to laser radiation and a laser produced plasma was more resistant to unipolar arcing than a cleaned, polished surface. It is recommended that experiments be carried out to determine the exact nature and thickness of surface layers produced on steels by multiple laser pulse exposure. It is also recommended that stainless steel targets be laser glazed commercially, using a focused CW CO₂ laser that is scanned across the target surface, and then determine the resulting surface's resistance to unipolar arcing. It is felt that this would be the best way to produce "smooth" layers of metallic glass, if indeed a metallic glass is produced, over a target surface area large enough for easy evaluation of plasma-surface interaction effects.

Finally, it is recommended that experiments be devised to determine the density and temperature of the laser produced plasma as it expands radially over the target surface. This would aid in evaluating a material's susceptibility to unipolar arcing and aid in determining the plasma density and temperature required for unipolar arc initiation in that material.

APPENDIX A

Composition of HY-130 Cast Steel

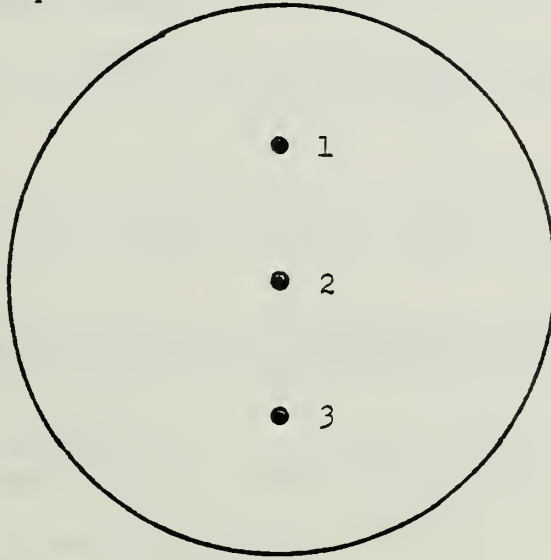
<u>Element</u>	<u>Weight Percentage of Target Samples</u>	<u>Specified Chemical Composition*</u>
Carbon	0.12	0.12 max.
Manganese	0.77	0.60 - 0.90
Phosphorus	0.010	0.010 max.
Sulfur	0.006	0.008 max.
Silicon	0.045	0.20 - 0.50
Copper	0.07	0.25 max.
Nickel	5.25	5.25 - 5.50
Chromium	0.57	0.40 - 0.70
Molybdenum	0.52	0.30 - 0.65
Vanadium	0.11	0.05 - 0.10
Titanium	0.02	0.02 max.
Aluminum	0.034	0.015 - 0.035
Nitrogen	44.0 ppm	<hr/>
Oxygen	43.0 ppm	35.0 ppm max.
Hydrogen	5.5 ppm	2.0 ppm max.

* Department of Navy Mil Spec MI-30-C/1, Dec. 1971.

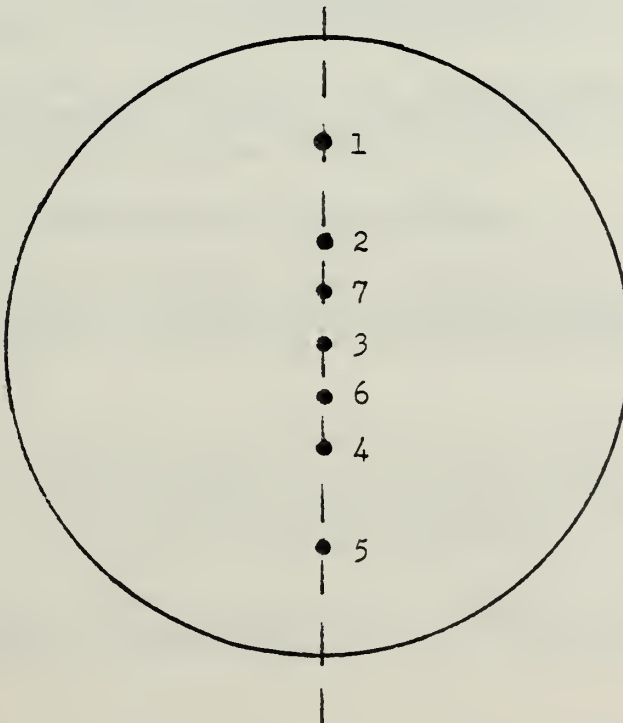
APPENDIX B

Laser Shot Sequences and Locations

1. Three-Shot Sequence



2. Seven-Shot Sequence



Location of Diamond Saw Cross Section Cut

LIST OF REFERENCES

1. Behrisch, R., "Surface Erosion from Plasma Materials Interaction", Journal of Nuclear Materials, vols. 85 & 86, pp. 1047-1061, 1979.
2. Goodall, D. H. J., Conlon, T. W., Sofield, C., and McCracken, G. M., "Investigation of Arcing in the DITE Tokamak", Journal of Nuclear Materials, vols. 76 & 77, pp. 492-498, 1978.
3. McCracken, G. M., and Goodall, D. H. J., "The Rule of Arcing in Producing Metal Impurities in Tokamaks", Nuclear Fusion, To Be Published, Culham Laboratory, Preprint, 1977.
4. Ryan, F. T., and Shedd, S. T., A Study of the Unipolar Arcing Damage Mechanism on Selected Conductors and Semiconductors, M.S. Thesis, The Naval Postgraduate School, Monterey, California, 1980.
5. Schwirzke, F., and Taylor, R. J., "Surface Damage by Sheath Effects and Unipolar Arcs", Journal of Nuclear Materials, vols. 94 & 95, 1980.
6. Chaudhari, P., Giessen, B. C., and Turnbull, D., "Metallic Glasses", Scientific American, April, 1980.
7. Matt, N. F., and Davis, E. A., Electronic Processes in Non-Crystalline Materials, p. 177, Clarendon Press, 1979.
8. Cooper, A. W., and Crittenden, E. C., Laser Physics and Applications to High Energy Lasers, Classroom Notes, The Naval Postgraduate School, Monterey, California, Summer, 1981.
9. Chen, F. F., Introduction to Plasma Physics, p. 54, Plenum Press, 1974.
10. Honeywell Corporate Research Center, Interim Report, Investigation of Material Damage. Pressure Pulses Produced by Carbon Dioxide Laser Radiation, by J. F. Ready, p. 66, 15 December 1974 to 14 December 1975.
11. Krehl, P., Schwirzke, F., and Cooper, A. W., "Correlation of Stress-Wave Profiles and the Dynamics of the Plasma Produced by Laser Irradiation on Plane Solid Targets", Journal of Applied Physics, vol. 46, no. 10, pp. 4400-4406, October, 1975.
12. Naval Research Laboratory Report 7728, Response of Materials to Laser Radiation: A Short Course, by J. T. Schriempf, p. 36, 10 July 1974.

13. Kim, Y. W., Strutt, P. R., and Nowotny, H., "Laser Melting and Heat Treatment of M2 Tool Steel: A Microstructural Characterization", Metallurgical Transactions, vol. 10A-no. 7, pp. 381-386, July, 1979.
14. Breinan, E. M., Kear, B. H., and Banas, C. M., "Processing Materials with Lasers", Physics Today, pp. 44-50, November, 1976.
15. Briant, C. L., and Ritter, A. M., "The Effects of Deformation Induced Martensite on The Sensitization of Austenitic Stainless Steels", Metallurgical Transactions, vol. 11S-no. 12, pp. 2009-2017, December 1980.
16. Davis, L. J., Self-Generated Magnetic Field Produced by Laser Bombardment of a Solid Target, M.S. Thesis, The Naval Postgraduate School, Monterey, California, 1971.
17. Barker, J. H., and Rush, R. J., An Investigation of Plasma-Surface Interactions on Selected Conductors and Insulators, M.S. Thesis, Naval Postgraduate School, Monterey, California, December, 1980.
18. Walter, J. L., Bartram, S. F., and Russell, R. R., "Crystallization of the Amorphous Alloys $\text{Fe}_{50}\text{Ni}_{30}\text{B}_{20}$ and $\text{Fe}_{80}\text{B}_{20}$ ", Metallurgical Transactions, vol. 9A, pp. 803-814, 1978.
19. Keville, M. T., and Lautrup, R. W., An Investigation of Unipolar Arcing Damage on Stainless Steel and Titanium Carbide Coated Surfaces, M.S. Thesis, The Naval Postgraduate School, Monterey, California, June 1980.

INITIAL DISTRIBUTION LIST

	Copies
1. Defense Technical Information Center Cameron Station Alexandria, Virginia 22314	2
2. Library, Code 0142 Naval Postgraduate School Monterey, California 93940	2
3. Department Chairman, Code 61 Department of Physics and Chemistry Naval Postgraduate School Monterey, California 93940	1
4. Assoc. Professor. F. R. Schwirzke, Code 61Sw Department of Physics and Chemistry Naval Postgraduate School Monterey, California 93940	3
5. Assoc. Professor K. D. Challenger, Code 69 Department of Mechanical Engineering Naval Postgraduate School Monterey, California 93940	1
6. LT Todd J. Hoover 5272 Morning Drive Hilliard, Ohio 43026	2

Thesis
H744
c.1

Hoover

195506

An investigation of
unipolar arcing in
various conductors and
metallic glasses.

16 MAY 86

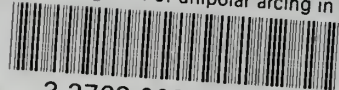
30978

Thesis
H744
c.1

Hoover

195506

An investigation of
unipolar arcing in
various conductors and
metallic glasses.



3 2768 002 06673 0
DUDLEY KNOX LIBRARY